The Astrophysical Journal Supplement Series, 180:330–376, 2009 February doi:10.1088/0067-0049/180/2/330

FIVE-YEAR *WILKINSON MICROWAVE ANISOTROPY PROBE** OBSERVATIONS: COSMOLOGICAL INTERPRETATION

E. Komatsu[1], J. Dunkley[2,3,4], M. R. Nolta[5], C. L. Bennett[6], B. Gold[6], G. Hinshaw[7], N. Jarosik[2], D. Larson[6], M. Limon[8], L. Page[2], D. N. Spergel[3,9], M. Halpern[10], R. S. Hill[11], A. Kogut[7], S. S. Meyer[12], G. S. Tucker[13], J. L. Weiland[11], E. Wollack[7], and E. L. Wright[14]

[1] Department of Astronomy, University of Texas, Austin, 2511 Speedway, RLM 15.306, Austin, TX 78712, USA; komatsu@astro.as.utexas.edu
[2] Department of Physics, Jadwin Hall, Princeton University, Princeton, NJ 08544-0708, USA
[3] Department of Astrophysical Sciences, Peyton Hall, Princeton University, Princeton, NJ 08544-1001, USA
[4] Astrophysics, University of Oxford, Keble Road, Oxford, OX1 3RH, UK
[5] Canadian Institute for Theoretical Astrophysics, 60 St. George St, University of Toronto, Toronto, ON M5S 3H8, Canada
[6] Department of Physics and Astronomy, The Johns Hopkins University, 3400 N. Charles St., Baltimore, MD 21218-2686, USA
[7] Code 665, NASA/Goddard Space Flight Center, Greenbelt, MD 20771, USA
[8] Columbia Astrophysics Laboratory, 550 W. 120th St., Mail Code 5247, New York, NY 10027-6902, USA
[9] Princeton Center for Theoretical Sciences, Princeton University, Princeton, NJ 08544, USA
[10] Department of Physics and Astronomy, University of British Columbia, Vancouver, BC V6T 1Z1, Canada
[11] Adnet Systems, Inc., 7515 Mission Dr., Suite A100, Lanham, MD 20706, USA
[12] Departments of Astrophysics and Physics, KICP and EFI, University of Chicago, Chicago, IL 60637, USA
[13] Department of Physics, Brown University, 182 Hope St., Providence, RI 02912-1843, USA
[14] UCLA Physics and Astronomy, P.O. Box 951547, Los Angeles, CA 90095-1547, USA
Received 2008 March 4; accepted 2008 June 25; published 2009 February 11

ABSTRACT

The *Wilkinson Microwave Anisotropy Probe* (*WMAP*) 5-year data provide stringent limits on deviations from the minimal, six-parameter Λ cold dark matter model. We report these limits and use them to constrain the physics of cosmic inflation via Gaussianity, adiabaticity, the power spectrum of primordial fluctuations, gravitational waves, and spatial curvature. We also constrain models of dark energy via its equation of state, parity-violating interaction, and neutrino properties, such as mass and the number of species. We detect no convincing deviations from the minimal model. The six parameters and the corresponding 68% uncertainties, derived from the *WMAP* data combined with the distance measurements from the Type Ia supernovae (SN) and the Baryon Acoustic Oscillations (BAO) in the distribution of galaxies, are: $\Omega_b h^2 = 0.02267^{+0.00058}_{-0.00059}$, $\Omega_c h^2 = 0.1131 \pm 0.0034$, $\Omega_\Lambda = 0.726 \pm 0.015$, $n_s = 0.960 \pm 0.013$, $\tau = 0.084 \pm 0.016$, and $\Delta^2_{\mathcal{R}} = (2.445 \pm 0.096) \times 10^{-9}$ at $k = 0.002\,\mathrm{Mpc}^{-1}$. From these, we derive $\sigma_8 = 0.812 \pm 0.026$, $H_0 = 70.5 \pm 1.3\,\mathrm{km\,s^{-1}\,Mpc^{-1}}$, $\Omega_b = 0.0456 \pm 0.0015$, $\Omega_c = 0.228 \pm 0.013$, $\Omega_m h^2 = 0.1358^{+0.0037}_{-0.0036}$, $z_{\mathrm{reion}} = 10.9 \pm 1.4$, and $t_0 = 13.72 \pm 0.12$ Gyr. With the *WMAP* data combined with BAO and SN, we find the limit on the tensor-to-scalar ratio of $r < 0.22$ (95% CL), and that $n_s > 1$ is disfavored even when gravitational waves are included, which constrains the models of inflation that can produce significant gravitational waves, such as chaotic or power-law inflation models, or a blue spectrum, such as hybrid inflation models. We obtain tight, simultaneous limits on the (constant) equation of state of dark energy and the spatial curvature of the universe: $-0.14 < 1 + w < 0.12$ (95% CL) and $-0.0179 < \Omega_k < 0.0081$ (95% CL). We provide a set of "*WMAP* distance priors," to test a variety of dark energy models with spatial curvature. We test a time-dependent w with a present value constrained as $-0.33 < 1 + w_0 < 0.21$ (95% CL). Temperature and dark matter fluctuations are found to obey the adiabatic relation to within 8.9% and 2.1% for the axion-type and curvaton-type dark matter, respectively. The power spectra of TB and EB correlations constrain a parity-violating interaction, which rotates the polarization angle and converts E to B. The polarization angle could not be rotated more than $-5.^\circ9 < \Delta\alpha < 2.^\circ4$ (95% CL) between the decoupling and the present epoch. We find the limit on the total mass of massive neutrinos of $\sum m_\nu < 0.67$ eV (95% CL), which is free from the uncertainty in the normalization of the large-scale structure data. The number of relativistic degrees of freedom (dof), expressed in units of the effective number of neutrino species, is constrained as $N_{\mathrm{eff}} = 4.4 \pm 1.5$ (68%), consistent with the standard value of 3.04. Finally, quantitative limits on physically-motivated primordial non-Gaussianity parameters are $-9 < f_{\mathrm{NL}}^{\mathrm{local}} < 111$ (95% CL) and $-151 < f_{\mathrm{NL}}^{\mathrm{equil}} < 253$ (95% CL) for the local and equilateral models, respectively.

Key words: cosmic microwave background – cosmology: observations – dark matter – early universe – instrumentation: detectors – space vehicles: instruments – telescopes

1. INTRODUCTION

Measurements of microwave background fluctuations by the *Cosmic Background Explorer* (*COBE*; Smoot et al. 1992; Bennett et al. 1994, 1996), the *Wilkinson Microwave Anisotropy Probe* (*WMAP*; Bennett et al. 2003a, 2003b), and ground and balloon-borne experiments (Miller et al. 1999, 2002; de Bernardis et al. 2000; Hanany et al. 2000; Netterfield et al. 2002; Ruhl et al. 2003; Mason et al. 2003; Sievers et al. 2003, 2007; Pearson et al. 2003; Readhead et al. 2004; Dickinson et al. 2004; Kuo et al. 2004, 2007; Reichardt et al. 2008; Jones et al. 2006; Montroy et al. 2006; Piacentini et al. 2006) have addressed many of the questions that were the focus of cosmology for the past 50

* *WMAP* is the result of a partnership between Princeton University and NASA's Goddard Space Flight Center. Scientific guidance is provided by the *WMAP* Science Team.

years: How old is the universe? How fast is it expanding? What is the size and shape of the universe? What is the composition of the universe? What seeded the formation of galaxies and large-scale structure?

By accurately measuring the statistical properties of the microwave background fluctuations, *WMAP* has helped establish a standard cosmology: a flat Λ cold dark matter (CDM) model composed of atoms, dark matter, and dark energy, with nearly scale-invariant adiabatic Gaussian fluctuations. With our most recent measurements, *WMAP* has measured the basic parameters of this cosmology to high precision: with the *WMAP* 5-year data alone, we find the density of dark matter (21.4%), the density of atoms (4.4%), the expansion rate of the universe, the amplitude of density fluctuations, and their scale dependence, as well as the optical depth due to reionization (Dunkley et al. 2009; also see Table 1 for summary).

Cosmologists are now focused on a new set of questions: What is the nature of the dark energy? What is the dark matter? Did inflation seed the primordial fluctuations? If so, what is the class of the inflationary model? How did the first stars form? Microwave background observations from *WMAP*, *Planck*, and from the upcoming generation of cosmic microwave background (CMB) ground and balloon-borne experiments will play an important role in addressing these questions.

This paper will discuss how the *WMAP* results, particularly when combined with other astronomical observations (mainly the distance measurements), are now providing new insights into these questions through constraints on gravitational waves and nonadiabatic (entropic) fluctuations, measurements of primordial non-Gaussianity, accurate determination of the primordial spectral index and the geometry of the universe, and limits on parity-violating interactions (see Table 2 for summary).

This paper is one of seven papers on the analysis of the *WMAP* 5-year data: Hinshaw et al. (2009) reported on the data processing, map-making, and systematic error limits; Hill et al. (2009) on the physical optics modeling of beams and the 5-year window functions (beam transfer functions); Gold et al. (2009) on the modeling, understanding, and subtraction of the temperature and polarized foreground emission; Wright et al. (2009) on the catalogue of point sources detected in the 5-year temperature data; Nolta et al. (2009) on the measurements of the temperature and polarization power spectra; and Dunkley et al. (2009) on the parameter estimation methodology, the cosmological parameters inferred from the *WMAP* data alone, and comparison between different cosmological data sets.

This paper is organized as follows. In Section 2, we briefly summarize new aspects of our analysis of the *WMAP* 5-year temperature and polarization data. In Section 3, we constrain the spatial curvature of the observable universe, Gaussianity/adiabaticity/scale-invariance of the primordial fluctuations, and the amplitude of primordial gravitational waves. We discuss their implications for the physics of the early, primordial universe. In Section 4, we demonstrate that the power spectra of TB and EB correlations,[15] which are usually ignored in the cosmological analysis, can be used to constrain a certain parity-violating interaction that couples to photons. In Section 5, we explore the nature of dark energy, and in Section 6, we study the properties of neutrinos in cosmology. We conclude in Section 7.

2. SUMMARY OF 5-YEAR ANALYSIS

2.1. WMAP 5-year Data: Temperature and Polarization

With 5 years of observations of Jupiter and an extensive physical optics modeling of beams (Hill et al. 2009), our understanding of the beam transfer function, b_l, has improved significantly: the fractional beam errors, $\Delta b_l/b_l$, have been nearly halved in most differencing assemblies (DAs). In some cases, for example W4, the errors have been reduced by as much as a factor of 4.

Many of the small-scale CMB experiments have been calibrated to the *WMAP* 3-year data at high multipoles. Since the new beam model raises the 5-year power spectrum almost uniformly by $\sim 2.5\%$ relative to the 3-year power spectrum over $l \gtrsim 200$ (Hill et al. 2009), these small-scale CMB experiments have been undercalibrated by the same amount, that is, $\sim 2.5\%$ in power and 1.2% in temperature. For example, the latest Arcminute Cosmology Bolometer Array Receiver (ACBAR) data (Reichardt et al. 2008) report on the calibration error of 2.23% in temperature (4.5% in power), which is twice as large as the magnitude of miscalibration; thus, we expect the effect of miscalibration to be subdominant in the error budget. Note that the change in the beam is fully consistent with the 1σ error of the previous *WMAP* beam reported in Page et al. (2003). Since the ACBAR calibration error includes the previous *WMAP* beam error, the change in the beam should have a minimal impact on the current ACBAR calibration.

While we use only V and W bands for the cosmological analysis of the temperature data, the treatment of b_l in Q band affects our determination of the point-source contamination to the angular power spectrum, $A_{\rm ps}$.[16] The 5-year estimate of the point-source correction, $A_{\rm ps} = 0.011 \pm 0.001\,\mu{\rm K}^2\,{\rm sr}$ (Nolta et al. 2009), is slightly lower than the 3-year estimate, $A_{\rm ps} = 0.014 \pm 0.003\,\mu{\rm K}^2\,{\rm sr}$ (Hinshaw et al. 2007), partly because more sources have been detected and masked by the 5-year source mask (390 sources have been detected in the 5-year temperature data, whereas 323 sources were detected in the 3-year data (Wright et al. 2009)).

Note that the uncertainty in $A_{\rm ps}$ has been reduced by a factor of 3. The uncertainty in the previous estimate was inflated to include the lower value found by Huffenberger et al. (2006) (0.011) and higher value from our original estimate (0.017). Much of the discrepancy between these estimates is due to the multipole range over which $A_{\rm ps}$ is fit. With the improved beam model from the 5-year analysis, the dependence on the multipole range has disappeared, and thus we no longer need to inflate our uncertainty. See Nolta et al. (2009) for more details.

The method for cleaning foreground emission in both temperature and polarization data is the same as we used for the 3-year data, that is, the template-based cleaning method described in Section 5.3 of Hinshaw et al. (2007) for temperature and Section 4.3 of Page et al. (2007) for polarization. Gold et al. (2009) described the results from the template cleaning of the 5-year data with the new coefficients. In addition, Gold et al. (2009) and Dunkley et al. (2009) explored alternative modelings of the foreground emission. All of these methods gave consistent results. Gold et al. (2009) also described definitions of the new masks, *KQ75* and *KQ85*, that replace the previous masks, *Kp0* and *Kp2*, that are recommended for the analysis of Gaussianity tests and the power spectrum, respectively.

[15] Here, "TB" refers to the power spectrum of a cross-correlation between the temperature and B-mode polarization, while "EB" refers to a correlation between the E-mode and B-mode polarization.

[16] This quantity, $A_{\rm ps}$, is the value of the power spectrum, C_l, from unresolved point sources in the Q band, in units of the antenna temperature. To convert this value to the thermodynamic units, use $C_{\rm ps} = 1.089 A_{\rm ps}$ (Nolta et al. 2009).

The method for measuring the TT and TE spectra at higher multipoles, that is, $l \geqslant 33$ for TT and $l \geqslant 24$ for TE, is also the same as we used for the 3-year data (Hinshaw et al. 2007). As for the estimation of the cosmological parameters from these spectra, we now include the weak gravitational lensing effect of CMB due to the intervening matter fluctuations (see Lewis & Challinor 2006, for a review), which was not included in the 3-year analysis. We continue to marginalize over a potential contribution from the Sunyaev–Zel'dovich effect (SZE), using exactly the same template SZE power spectrum that we used for the 3-year analysis: $C_l^{\rm SZE}$ from Komatsu & Seljak (2002) with $\Omega_m = 0.26$, $\Omega_b = 0.044$, $h = 0.72$, $n_s = 0.97$, and $\sigma_8 = 0.80$ (see also Section 2.1 of Spergel et al. 2007). We continue to use the *V*- and *W*-band data for estimating the high-l temperature power spectrum, and the Q- and V-band data for the high-l polarization power spectra.

We have improved our treatment of the temperature and polarization power spectra at lower multipoles, as described below.

Low-l temperature. We use the Gibbs sampling technique and the Blackwell–Rao (BR) estimator to evaluate the likelihood of the temperature power spectrum at $l \leqslant 32$ (Jewell et al. 2004; Wandelt 2003; Wandelt et al. 2004; O'Dwyer et al. 2004; Eriksen et al. 2004a, 2007c, 2007b; Chu et al. 2005; Larson et al. 2007). For the 3-year analysis, we used the resolution 4 Internal Linear Combination (ILC) temperature map ($N_{\rm side} = 16$) with a Gaussian smoothing of $9\overset{\circ}{.}183$ (FWHM). Since the ILC map has an intrinsic Gaussian smoothing of 1°, we have added an extra smoothing of $9\overset{\circ}{.}1285$. We then directly evaluated the likelihood in the pixel space for a given C_l. For the 5-year analysis, we use a higher-resolution map, the resolution 5 ILC map ($N_{\rm side} = 32$) with a smaller Gaussian smoothing of 5° (FWHM). The potential foreground leakage due to smoothing is, therefore, reduced. The BR estimator has an advantage of being much faster to compute, which is why we have adopted the Gibbs sampling and the BR estimator for the 5-year data release. We have confirmed that both the resolution 4 pixel-based likelihood and the resolution 5 Gibbs-based likelihood yield consistent results (see Dunkley et al. 2009 for details). Both options are made publicly available in the released likelihood code.

Low-l polarization. While we continue to use the direct evaluation of the likelihood of polarization power spectra in pixel space from coadded resolution 3 ($N_{\rm side} = 8$) polarization maps (Stokes Q and U maps), we now add the Ka band data to the coadded maps; we used only Q- and V-band data for the 3-year analysis. We believe that we understand the polarized foreground emission (dominated by synchrotron, traced well by the K-band data) in the Ka band data well enough to justify the inclusion of the Ka band (Gold et al. 2009). This, with 2 years of more integration, has led to a significant reduction of the noise power spectra (averaged over $l = 2 - 7$) in the polarization EE and BB power spectra by a factor of as much as 2.3 compared to the 3-year analysis. As a result, the EE power spectrum averaged over $l = 2 - 7$ exceeds the noise by a factor of 10, that is, our measurement of the EE power spectrum averaged over $l = 2-7$ is now limited by cosmic variance and the possibility of residual foreground emission and/or systematic errors,[17] rather than by noise. In addition, we have added a capability of computing the likelihood of TB and EB power spectra to the released likelihood code. This allows us to test models in which nonzero TB and EB correlations can be generated. We discuss this further in Section 4.

We continue to use the Markov Chain Monte Carlo (MCMC) technique to explore the posterior distribution of cosmological parameters given the measured temperature and polarization power spectra. For details on the implementation and convergence criteria, see Dunkley et al. (2009).

2.2. Comments on Systematic Errors in the Cosmological Parameters Derived from the WMAP 5-year Data

Hinshaw et al. (2009) gave extensive descriptions of our limits on the systematic errors in the *WMAP* 5-year temperature and polarization data. With the improved treatment of beams and gain calibrations, we are confident that the instrumental systematic errors in the cosmological results derived from the temperature data are negligible compared to the statistical errors. As for the polarization data, we find that the W-band polarization data still contain the systematic errors that we do not fully understand, and thus we do not use the W-band polarization for the cosmological analysis. We do not find any evidence for the unaccounted instrumental systematic errors in the other bands that we use for cosmology.

The most dominant systematic errors in the cosmological analysis are the foreground emission. Since CMB dominates over the foreground emission in the temperature data in V and W bands outside the galaxy mask, and we also reduce the subdominant foreground contamination at high Galactic latitudes further by using the K- and Ka-band data (for synchrotron emission), the external Hα map (for free–free emission), and the external dust map, the systematic errors from the foreground emission are unimportant for the temperature data, even at the lowest multipoles where the foreground is most important (Gold et al. 2009).

We, however, find that the uncertainty in our modeling of the *polarized* foreground is not negligible compared to the statistical errors. For the 5-year polarization analysis, we have used two independent foreground-cleaning algorithms: one based upon the template fitting (as developed for the 3-year analysis; see Page et al. 2007) and the other based upon the Gibbs sampling (Dunkley et al. 2008). The optical depth, τ, is the parameter that is most affected by the uncertainty in the polarized foreground model. The template fitting method gives $\tau = 0.087 \pm 0.017$. The Gibbs sampling method gives a range of values from $\tau = 0.085 \pm 0.025$ to $\tau = 0.103 \pm 0.018$, depending upon various assumptions made about the properties of the polarized synchrotron and dust emission. Therefore, the systematic error in τ is comparable to the statistical error.

This has an implication for the determination of the primordial tilt, n_s, as there is a weak correlation between n_s and τ (see Figure 1): for $\tau = 0.087$, we find $n_s = 0.963$, while for $\tau = 0.105$, we find $n_s = 0.98$. Since the statistical error of n_s is 0.015, the systematic error in n_s (from the polarized foreground) is comparable to the statistical one. The other parameters that are correlated with n_s, that is, the baryon density (Figure 1), the tensor-to-scalar ratio (Figure 2), and the amplitude of nonadiabatic fluctuations (Sections 3.6.3 and 3.6.4), would be similarly affected. For the parameters that are not correlated with n_s or τ, the systematic errors are insignificant.

2.3. External Data Sets: Hubble Constant, Luminosity, and Angular Diameter Distances

Aside from the CMB data (including the small-scale CMB measurements), the main external astrophysical results that we

[17] For our limits on the residual polarized foreground contamination, see Dunkley et al. (2008).

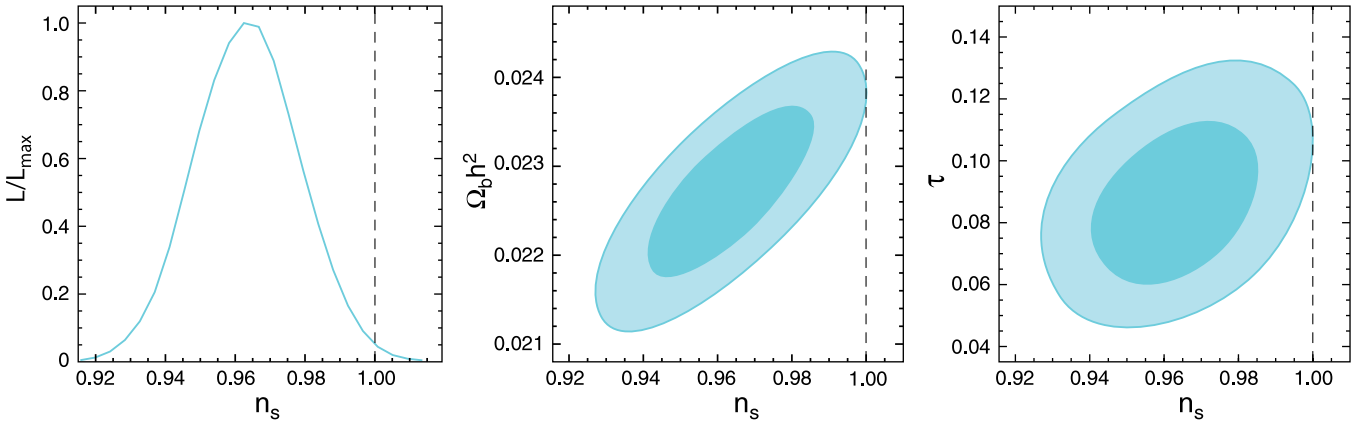

Figure 1. Constraint on the primordial tilt, n_s (Section 3.1.2). No running index or gravitational waves are included in the analysis. (Left) One-dimensional marginalized constraint on n_s from the *WMAP*-only analysis. (Middle) Two-dimensional joint marginalized constraint (68% and 95% CL), showing a strong correlation between n_s and $\Omega_b h^2$. (Right) A mild correlation with τ. None of these correlations are reduced significantly by including BAO or SN data, as these datasets are not sensitive to $\Omega_b h^2$ or τ; however, the situation changes when the gravitational wave contribution is included (see Figure 2).

shall use in this paper for the joint cosmological analysis are the following distance-scale indicators.

1. A Gaussian prior on the present-day Hubble's constant from the Hubble Key Project final results, $H_0 = 72 \pm 8$ km s^{-1} Mpc^{-1} (Freedman et al. 2001). While the uncertainty is larger than the *WMAP*'s determination of H_0 for the minimal ΛCDM model (see Table 1), this information improves upon limits on the other models, such as models with nonzero spatial curvature.
2. The luminosity distances out to Type Ia supernovae (SNe) with their absolute magnitudes marginalized over uniform priors. We use the "union" SN samples compiled by Kowalski et al. (2008). The union compilation contains 57 nearby ($0.015 < z \lesssim 0.15$) Type Ia SNe and 250 high-z Type Ia SNe, after selection cuts. The high-z samples contain the Type Ia SNe from the *Hubble Space Telescope* (*HST*; Knop et al. 2003; Riess et al. 2004, 2007), the SuperNova Legacy Survey (SNLS; Astier et al. 2006), the Equation of State: SupErNovae trace Cosmic Expansion (ESSENCE) survey (Wood-Vasey et al. 2007), as well as those used in the original papers of the discovery of the acceleration of the universe (Riess et al. 1998; Perlmutter et al. 1999), and the samples from Barris et al. (2004) and Tonry et al. (2003). The nearby Type Ia SNe are taken from Hamuy et al. (1996), Riess et al. (1999), Jha et al. (2006), Krisciunas et al. (2001, 2004a, 2004b). Kowalski et al. (2008) have processed all of these samples using the same light curve fitter called SALT (Guy et al. 2005), which allowed them to combine all the data in a self-consistent fashion. The union compilation is the largest to date. The previous compilation by Davis et al. (2007) used a smaller number of Type Ia SNe, and did not use the same light curve fitter for all the samples. We examine the difference in the derived ΛCDM cosmological parameters between the union compilation and Davis et al.'s compilation in Appendix D. While we ignore the systematic errors when we fit the Type Ia SN data, we examine the effects of systematic errors on the ΛCDM parameters and the dark energy parameters in Appendix D.
3. Gaussian priors on the distance ratios, $r_s/D_V(z)$, at $z = 0.2$ and 0.35 measured from the Baryon Acoustic Oscillations (BAO) in the distribution of galaxies (Percival et al. 2007). The CMB observations measure the acoustic oscillations in the photon-baryon plasma, which can be used to measure the angular diameter distance to the photon decoupling epoch. The same oscillations are imprinted on the distribution of matter, traced by the distribution of galaxies, which can be used to measure the angular distances to the galaxies that one observes from galaxy surveys. While both CMB and galaxies measure the same oscillations, in this paper, we shall use the term, BAO, to refer only to the oscillations in the distribution of matter, for definiteness.

Here, we describe how we use the BAO data in more detail. The BAO can be used to measure not only the angular diameter distance, $D_A(z)$, through the clustering perpendicular to the line of sight, but also the expansion rate of the universe, $H(z)$, through the clustering along the line of sight. This is a powerful probe of dark energy; however, the accuracy of the current data does not allow us to extract $D_A(z)$ and $H(z)$ separately, as one can barely measure BAO in the spherically-averaged correlation function (Okumura et al. 2008).

The spherical average gives us the following effective distance measure (Eisenstein et al. 2005):

$$D_V(z) \equiv \left[(1+z)^2 D_A^2(z) \frac{cz}{H(z)}\right]^{1/3}, \quad (1)$$

where $D_A(z)$ is the proper (not comoving) angular diameter distance:

$$D_A(z) = \frac{c}{H_0} \frac{f_k\left[H_0\sqrt{|\Omega_k|}\int_0^z \frac{dz'}{H(z')}\right]}{(1+z)\sqrt{|\Omega_k|}}, \quad (2)$$

where $f_k[x] = \sin x$, x, and $\sinh x$ for $\Omega_k < 0$ ($k = 1$), $\Omega_k = 0$ ($k = 0$), and $\Omega_k > 0$ ($k = -1$), respectively.

There is an additional subtlety. The peak positions of the (spherically averaged) BAO depend actually on the *ratio* of $D_V(z)$ to the sound horizon size at the so-called drag epoch, z_d, at which baryons were released from photons. Note that there is no reason why the decoupling epoch of photons, z_*, needs to be the same as the drag epoch, z_d. They would be equal only when the energy density of photons and that of baryons were equal at the decoupling epoch—more precisely, they would be equal only when $R(z) \equiv 3\rho_b/(4\rho_\gamma) = (3\Omega_b/4\Omega_\gamma)/(1+z) \simeq 0.67(\Omega_b h^2/0.023)[1090/(1+z)]$ was unity at $z = z_*$. Since we happen to live in the universe in which $\Omega_b h^2 \simeq 0.023$, this ratio

Table 1
Summary of the Cosmological Parameters of ΛCDM Model and the Corresponding 68% Intervals

Class	Parameter	*WMAP* 5 Year ML[a]	*WMAP*+BAO+SN ML	*WMAP* 5 Year Mean[b]	*WMAP*+BAO+SN Mean
Primary	$100\Omega_b h^2$	2.268	2.262	2.273 ± 0.062	$2.267^{+0.058}_{-0.059}$
	$\Omega_c h^2$	0.1081	0.1138	0.1099 ± 0.0062	0.1131 ± 0.0034
	Ω_Λ	0.751	0.723	0.742 ± 0.030	0.726 ± 0.015
	n_s	0.961	0.962	$0.963^{+0.014}_{-0.015}$	0.960 ± 0.013
	τ	0.089	0.088	0.087 ± 0.017	0.084 ± 0.016
	$\Delta^2_{\mathcal{R}}(k_0^c)$	2.41×10^{-9}	2.46×10^{-9}	$(2.41 \pm 0.11) \times 10^{-9}$	$(2.445 \pm 0.096) \times 10^{-9}$
Derived	σ_8	0.787	0.817	0.796 ± 0.036	0.812 ± 0.026
	H_0	$72.4\,\mathrm{km\,s^{-1}\,Mpc^{-1}}$	$70.2\,\mathrm{km\,s^{-1}\,Mpc^{-1}}$	$71.9^{+2.6}_{-2.7}$ km s^{-1} Mpc^{-1}	70.5 ± 1.3 km s$^-$ Mpc$^-$
	Ω_b	0.0432	0.0459	0.0441 ± 0.0030	0.0456 ± 0.0015
	Ω_c	0.206	0.231	0.214 ± 0.027	0.228 ± 0.013
	$\Omega_m h^2$	0.1308	0.1364	0.1326 ± 0.0063	$0.1358^{+0.0037}_{-0.0036}$
	$z^{\mathrm{d}}_{\mathrm{reion}}$	11.2	11.3	11.0 ± 1.4	10.9 ± 1.4
	t_0^{e}	13.69 Gyr	13.72 Gyr	13.69 ± 0.13 Gyr	13.72 ± 0.12 Gyr

Notes.
[a] Dunkley et al. (2009). "ML" refers to the Maximum Likelihood parameters.
[b] Dunkley et al. (2009). "Mean" refers to the mean of the posterior distribution of each parameter.
[c] $k_0 = 0.002\,\mathrm{Mpc}^{-1}$. $\Delta^2_{\mathcal{R}}(k) = k^3 P_{\mathcal{R}}(k)/(2\pi^2)$ (Equation (15)).
[d] "Redshift of reionization," if the universe was reionized instantaneously from the neutral state to the fully ionized state at z_{reion}.
[e] The present-day age of the universe.

Table 2
Summary of the 95% Confidence Limits on Deviations from the Simple (Flat, Gaussian, Adiabatic, Power-Law) ΛCDM Model

Section	Name	Type	*WMAP* 5 Year	*WMAP*+BAO+SN
Section 3.2	Gravitational wave[a]	No running index	$r < 0.43$[b]	$r < 0.22$
Section 3.1.3	Running index	No grav. wave	$-0.090 < dn_s/d\ln k < 0.019$[c]	$-0.068 < dn_s/d\ln k < 0.012$
Section 3.4	Curvature[d]		$-0.063 < \Omega_k < 0.017$[e]	$-0.0179 < \Omega_k < 0.0081$[f]
	Curvature radius[g]	Positive curv.	$R_{\mathrm{curv}} > 12\,h^{-1}$ Gpc	$R_{\mathrm{curv}} > 22\,h^{-1}$ Gpc
		Negative curv.	$R_{\mathrm{curv}} > 23\,h^{-1}$ Gpc	$R_{\mathrm{curv}} > 33\,h^{-1}$ Gpc
Section 3.5	Gaussianity	Local	$-9 < f_{\mathrm{NL}}^{\mathrm{local}} < 111$[h]	N/A
		Equilateral	$-151 < f_{\mathrm{NL}}^{\mathrm{equil}} < 253$[i]	N/A
Section 3.6	Adiabaticity	Axion	$\alpha_0 < 0.16$[j]	$\alpha_0 < 0.072$[k]
		Curvaton	$\alpha_{-1} < 0.011$[l]	$\alpha_{-1} < 0.0041$[m]
Section 4	Parity violation	Chern–Simons[n]	$-5.^\circ9 < \Delta\alpha < 2.^\circ4$	N/A
Section 5	Dark energy	Constant w[o]	$-1.37 < 1 + w < 0.32$[p]	$-0.14 < 1 + w < 0.12$
		Evolving $w(z)$[q]	N/A	$-0.33 < 1 + w_0 < 0.21$[r]
Section 6.1	Neutrino mass[s]		$\sum m_\nu < 1.3\,\mathrm{eV}$[t]	$\sum m_\nu < 0.67\,\mathrm{eV}$[u]
Section 6.2	Neutrino species		$N_{\mathrm{eff}} > 2.3$[v]	$N_{\mathrm{eff}} = 4.4 \pm 1.5$[w] (68%)

Notes.
[a] In the form of the tensor-to-scalar ratio, r, at $k = 0.002\,\mathrm{Mpc}^{-1}$.
[b] Dunkley et al. (2009).
[c] Dunkley et al. (2009).
[d] (Constant) dark energy equation of state allowed to vary ($w \neq -1$).
[e] With the *HST* prior, $H_0 = 72 \pm 8\,\mathrm{km\,s^{-1}\,Mpc^{-1}}$. For $w = -1$, $-0.052 < \Omega_k < 0.013$ (95% CL).
[f] For $w = -1$, $-0.0178 < \Omega_k < 0.0066$ (95% CL).
[g] $R_{\mathrm{curv}} = (c/H_0)/\sqrt{|\Omega_k|} = 3/\sqrt{|\Omega_k|}\,h^{-1}$ Gpc.
[h] Cleaned V + W map with $l_{\mathrm{max}} = 500$ and the *KQ75* mask, after the point-source correction.
[i] Cleaned V + W map with $l_{\mathrm{max}} = 700$ and the *KQ75* mask, after the point-source correction.
[j] Dunkley et al. (2009).
[k] In terms of the adiabaticity deviation parameter, $\delta_{adi}^{(c,\gamma)} = \sqrt{\alpha}/3$ (Equation (39)), the axion-like dark matter and photons are found to obey the adiabatic relation (Equation (36)) to 8.9%.
[l] Dunkley et al. (2009).
[m] In terms of the adiabaticity deviation parameter, $\delta_{adi}^{(c,\gamma)} = \sqrt{\alpha}/3$ (Equation (39)), the curvaton-like dark matter and photons are found to obey the adiabatic relation (Equation (36)) to 2.1%.
[n] For an interaction of the form given by $[\phi(t)/M]F_{\alpha\beta}\tilde{F}^{\alpha\beta}$, the polarization rotation angle is $\Delta\alpha = M^{-1}\int \frac{dt}{a}\dot{\phi}$.
[o] For spatially curved universes ($\Omega_k \neq 0$).
[p] With the *HST* prior, $H_0 = 72 \pm 8\,\mathrm{km\,s^{-1}\,Mpc^{-1}}$.
[q] For a flat universe ($\Omega_k = 0$).
[r] $w_0 \equiv w(z = 0)$.
[s] $\sum m_\nu = 94(\Omega_\nu h^2)\,\mathrm{eV}$.
[t] Dunkley et al. (2009).
[u] For $w = -1$. For $w \neq -1$, $\sum m_\nu < 0.80$ eV (95% CL).
[v] Dunkley et al. (2009).
[w] With the *HST* prior, $H_0 = 72 \pm 8\,\mathrm{km\,s^{-1}\,Mpc^{-1}}$. The 95% limit is $1.8 < N_{\mathrm{eff}} < 7.6$.

Table 3
Sound Horizon Scales Determined by the *WMAP* 5-year Data

	Quantity	Equation	5 Year *WMAP*
CMB	z_*	(66)	1090.51 ± 0.95
CMB	$r_s(z_*)$	(6)	146.8 ± 1.8 Mpc
Matter	z_d	(3)	1020.5 ± 1.6
Matter	$r_s(z_d)$	(6)	153.3 ± 2.0 Mpc

Notes. CMB: the sound horizon scale at the photon decoupling epoch, z_*, imprinted on the CMB power spectrum; matter: the sound horizon scale at the baryon drag epoch, z_d, imprinted on the matter (galaxy) power spectrum.

is less than unity, and thus the drag epoch is slightly later than the photon decoupling epoch, $z_d < z_*$. As a result, the sound horizon size at the drag epoch happens to be slightly larger than that at the photon decoupling epoch. In Table 3, we give the CMB decoupling epoch, BAO drag epoch, as well as the corresponding sound horizon radii that are determined from the *WMAP* 5-year data.

We use a fitting formula for z_d proposed by Eisenstein & Hu (1998):

$$z_d = \frac{1291(\Omega_m h^2)^{0.251}}{1+0.659(\Omega_m h^2)^{0.828}}\left[1+b_1(\Omega_b h^2)^{b2}\right], \quad (3)$$

where

$$b_1 = 0.313(\Omega_m h^2)^{-0.419}\left[1+0.607(\Omega_m h^2)^{0.674}\right], \quad (4)$$

$$b_2 = 0.238(\Omega_m h^2)^{0.223}. \quad (5)$$

In this paper, we frequently combine the *WMAP* data with $r_s(z_d)/D_V(z)$ extracted from the Sloan Digital Sky Survey (SDSS) and the Two Degree Field Galaxy Redshift Survey (2dFGRS; Percival et al. 2007), where $r_s(z)$ is the comoving sound horizon size given by

$$r_s(z) = \frac{c}{\sqrt{3}}\int_0^{1/(1+z)} \frac{da}{a^2 H(a)\sqrt{1+(3\Omega_b/4\Omega_\gamma)a}}, \quad (6)$$

where $\Omega_\gamma = 2.469 \times 10^{-5} h^{-2}$ for $T_{\rm cmb} = 2.725$ K, and

$$H(a) = H_0\left[\frac{\Omega_m}{a^3}+\frac{\Omega_r}{a^4}+\frac{\Omega_k}{a^2}+\frac{\Omega_\Lambda}{a^{3(1+w_{\rm eff}(a))}}\right]^{1/2}. \quad (7)$$

The radiation density parameter, Ω_r, is the sum of photons and relativistic neutrinos,

$$\Omega_r = \Omega_\gamma\,(1+0.2271 N_{\rm eff}), \quad (8)$$

where $N_{\rm eff}$ is the effective number of neutrino species (the standard value is 3.04). For more details on $N_{\rm eff}$, see Section 6.2. When neutrinos are nonrelativistic at a, one needs to reduce the value of $N_{\rm eff}$ accordingly. Also, the matter density must contain the neutrino contribution when they are nonrelativistic,

$$\Omega_m = \Omega_c + \Omega_b + \Omega_\nu, \quad (9)$$

where Ω_ν is related to the sum of neutrino masses as

$$\Omega_\nu = \frac{\sum m_\nu}{94 h^2\,{\rm eV}}. \quad (10)$$

For more details on the neutrino mass, see Section 6.1.

All the density parameters refer to the values at the present epoch, and add up to unity:

$$\Omega_m + \Omega_r + \Omega_k + \Omega_\Lambda = 1. \quad (11)$$

Throughout this paper, we shall use Ω_Λ to denote the dark energy density parameter at present:

$$\Omega_\Lambda \equiv \Omega_{de}(z=0). \quad (12)$$

Here, $w_{\rm eff}(a)$ is the effective equation of state of dark energy given by

$$w_{\rm eff}(a) \equiv \frac{1}{\ln a}\int_0^{\ln a} d\ln a' w(a'), \quad (13)$$

and $w(a)$ is the usual dark energy equation of state, that is, the dark energy pressure divided by the dark energy density:

$$w(a) \equiv \frac{P_{de}(a)}{\rho_{de}(a)}. \quad (14)$$

For vacuum energy (cosmological constant), w does not depend on time, and $w = -1$.

Percival et al. (2007) have determined $r_s(z_d)/D_V(z)$ out to two redshifts, $z = 0.2$ and 0.35, as $r_s(z_d)/D_V(z=0.2) = 0.1980 \pm 0.0058$ and $r_s(z_d)/D_V(z=0.35) = 0.1094 \pm 0.0033$, with a correlation coefficient of 0.39. We follow the description given in Appendix A of Percival et al. (2007) to implement these constraints in the likelihood code. We have checked that our calculation of $r_s(z_d)$ using the above formulae (including z_d) matches the value that they quote,[18] $111.426\,h^{-1}$ Mpc, to within $0.2\,h^{-1}$ Mpc, for their quoted cosmological parameters, $\Omega_m = 0.25$, $\Omega_b h^2 = 0.0223$, and $h = 0.72$.

We have decided to use these results, as they measure only the distances, and are not sensitive to the growth of structure. This property enables us to identify the information added by the external astrophysical results more clearly. In addition to these, we shall also use the BAO measurement by Eisenstein et al. (2005)[19] and the flux power spectrum of Lyα forest from Seljak et al. (2006) in the appropriate context.

For the 3-year data analysis in Spergel et al. (2007), we also used the shape of the galaxy power spectra measured from the SDSS main sample and the Luminous Red Galaxies (Tegmark et al. 2004b, 2006), and 2dFGRS (Cole et al. 2005). We have found some tension between these data sets, which could be indicative of the degree by which our understanding of nonlinearities, such as the nonlinear matter clustering, nonlinear bias, and nonlinear redshift space distortion, is still limited at low redshifts, that is, $z \lesssim 1$. See Dunkley et al. (2009) for more detailed study on this issue. Also see Sánchez & Cole (2008) on the related subject. The galaxy power spectra should provide us with important information on the growth of structure (which helps constrain the dark energy and neutrino masses) as our understanding of nonlinearities improves in the future. In this paper, we do not combine these datasets because of the limited understanding of the consequences of nonlinearities.

[18] In Percival et al. (2007), the authors used a different notation for the drag redshift, z_*, instead of z_d. We have confirmed that they have used equation (6) of Eisenstein & Hu (1998) for r_s, which makes an explicit use of the drag redshift (W. Percival 2008, private communication).

[19] We use a Gaussian prior on $A = D_V(z=0.35)\sqrt{\Omega_m H_0^2}/(0.35c) = 0.469(n_s/0.98)^{-0.35} \pm 0.017$.

3. FLAT, GAUSSIAN, ADIABATIC, POWER-LAW ΛCDM MODEL, AND ITS ALTERNATIVES

The theory of inflation, the idea that the universe underwent a brief period of rapid accelerated expansion (Starobinsky 1979, 1982; Kazanas 1980; Guth 1981; Sato 1981; Linde 1982; Albrecht & Steinhardt 1982), has become an indispensable building block of the standard model of our universe.

Models of the early universe must explain the following observations: the universe is nearly flat and the fluctuations observed by *WMAP* appear to be nearly Gaussian (Komatsu et al. 2003), scale-invariant, super-horizon, and adiabatic (Spergel & Zaldarriaga 1997; Spergel et al. 2003; Peiris et al. 2003). Inflation models have been able to explain these properties successfully (Mukhanov & Chibisov 1981; Hawking 1982; Starobinsky 1982; Guth & Pi 1982; Bardeen et al. 1983).

Although many models have been ruled out observationally (see Kinney et al. 2006; Alabidi & Lyth 2006a; Martin & Ringeval 2006, for recent surveys), there are more than 100 candidate inflation models available (see Liddle & Lyth 2000; Bassett et al. 2006; Linde 2008, for reviews). Therefore, we now focus on the question, "*which model is the correct inflation model?*" This must be answered by the observational data.

However, an inflationary expansion may not be the only way to solve cosmological puzzles and create primordial fluctuations. Contraction of the primordial universe followed by a bounce to expansion can, in principle, make a set of predictions that are qualitatively similar to those of inflation models (Khoury et al. 2001, 2002a, 2002b, 2003; Buchbinder et al. 2007, 2008; Koyama & Wands 2007; Koyama et al. 2007; Creminelli & Senatore 2007), although building concrete models and making robust predictions have been challenging (Kallosh et al. 2001a, 2001b, 2008; Linde 2002).

There is also a fascinating possibility that one can learn something about the fundamental physics from cosmological observations. For example, recent progress in implementing de Sitter vacua and inflation in the context of string theory (see McAllister & Silverstein 2008, for a review) makes it possible to connect the cosmological observations to the ingredients of the fundamental physics via their predicted properties of inflation such as the shape of the power spectrum, spatial curvature of the universe, and non-Gaussianity of primordial fluctuations.

3.1. Power Spectrum of Primordial Fluctuations

3.1.1. Motivation and Analysis

The shape of the power spectrum of primordial curvature perturbations, $P_{\mathcal{R}}(k)$, is one of the most powerful and practical tool for distinguishing among inflation models. Inflation models with featureless scalar-field potentials usually predict that $P_{\mathcal{R}}(k)$ is *nearly* a power law (Kosowsky & Turner 1995)

$$\Delta^2_{\mathcal{R}}(k) \equiv \frac{k^3 P_{\mathcal{R}}(k)}{2\pi^2} = \Delta^2_{\mathcal{R}}(k_0)\left(\frac{k}{k_0}\right)^{n_s(k_0)-1+\frac{1}{2}dn_s/d\ln k} . \quad (15)$$

Here, $\Delta^2_{\mathcal{R}}(k)$ is a useful quantity, which gives an approximate contribution of $\mathcal{R}$ at a given scale per logarithmic interval in k to the total variance of $\mathcal{R}$, as $\langle \mathcal{R}^2(\mathbf{x})\rangle = \int d\ln k \Delta^2_{\mathcal{R}}(k)$. It is clear that the special case with $n_s = 1$ and $dn_s/d\ln k = 0$ results in the "scale-invariant spectrum," in which the contributions of $\mathcal{R}$ at any scales per logarithmic interval in k to the total variance are equal (hence, the term "scale invariance"). Following the usual terminology, we shall call n_s and $dn_s/d\ln k$ the tilt of the spectrum and the running index, respectively. We shall take k_0 to be $0.002\,\mathrm{Mpc}^{-1}$.

The significance of n_s and $dn_s/d\ln k$ is that different inflation models motivated by different physics make specific, testable predictions for the values of n_s and $dn_s/d\ln k$. For a given shape of the scalar field potential, $V(\phi)$, of a single-field model, for instance, one finds that n_s is given by a combination of the first derivative and second derivative of the potential, $1-n_s = 3M^2_{pl}(V'/V)^2 - 2M^2_{pl}(V''/V)$ (where $M^2_{pl} = 1/(8\pi G)$ is the reduced Planck mass), and $dn_s/d\ln k$ is given by a combination of V'/V, V''/V, and V'''/V (see Liddle & Lyth 2000, for a review).

This means that one can reconstruct the shape of $V(\phi)$ up to the first three derivatives in this way. As the expansion rate squared is proportional to $V(\phi)$ via the Friedmann equation, $H^2 = V/(3M^2_{pl})$, one can reconstruct the expansion history during inflation by measuring the shape of the primordial power spectrum.

How generic are n_s and $dn_s/d\ln k$? They are physically motivated by the fact that most inflation models satisfy the slow-roll conditions, and thus deviations from a pure power-law, scale-invariant spectrum, $n_s = 1$ and $dn_s/d\ln k = 0$, are expected to be small, and the higher-order derivative terms such as V'''' and higher are negligible. However, there is always a danger of missing some important effects, such as sharp features, when one relies too much on a simple parametrization like this. Therefore, a number of people have investigated various, more general ways of reconstructing the shape of $P_{\mathcal{R}}(k)$ (Matsumiya et al. 2002, 2003; Mukherjee & Wang 2003b, 2003a, 2003c; Bridle et al. 2003; Kogo et al. 2004, 2005; Hu & Okamoto 2004; Hannestad 2004; Shafieloo & Souradeep 2004, 2008; Sealfon et al. 2005; Tocchini-Valentini et al. 2005, 2006; Spergel et al. 2007; Verde & Peiris 2008) and $V(\phi)$ (Lidsey et al. 1997; Grivell & Liddle 2000; Kadota et al. 2005; Covi et al. 2006; Lesgourgues & Valkenburg 2007; Powell & Kinney 2007).

These studies have indicated that the parametrized form (Equation (15)) is basically a good fit, and no significant features were detected. Therefore, we do not repeat this type of analysis in this paper, but focus on constraining the parametrized form given by Equation (15).

Finally, let us comment on the choice of priors. We impose uniform priors on n_s and $dn_s/d\ln k$, but there are other possibilities for the choice of priors. For example, one may impose uniform priors on the slow-roll parameters, $\epsilon = (M^2_{pl}/2)(V'/V)^2$, $\eta = M^2_{pl}(V''/V)$ and $\xi = M^4_{pl}(V'V'''/V^2)$, and on the number of e-foldings, N, rather than on n_s and $dn_s/d\ln k$ (Peiris & Easther 2006a, 2006b; Easther & Peiris 2006). It has been found that, as long as one imposes a reasonable lower bound on N, $N > 30$, both approaches yield similar results.

To constrain n_s and $dn_s/d\ln k$, we shall use the *WMAP* 5-year temperature and polarization data, the small-scale CMB data, and/or BAO and SN distance measurements. In Table 4, we summarize our results presented in Sections 3.1.2, 3.1.3, and 3.2.4.

3.1.2. Results: Tilt

First, we test the inflation models with $dn_s/d\ln k = 0$ and negligible gravitational waves. The *WMAP* 5-year temperature and polarization data yield $n_s = 0.963^{+0.014}_{-0.015}$, which is slightly above the 3-year value with a smaller uncertainty, $n_s(3\mathrm{yr}) = 0.958 \pm 0.016$ (Spergel et al. 2007). We shall provide the reason for this small upward shift in Section 3.1.3.

Table 4
Primordial Tilt n_s, Running Index $dn_s/d\ln k$, and Tensor-to-Scalar Ratio r

Section	Model	Parameter[a]	5 Year *WMAP*[b]	5 Year *WMAP* = +CMB[c]	5 Year *WMAP*+ACBAR08[d]	5 Year *WMAP*+BAO+SN
Section 3.1.2	Power law	n_s	$0.963^{+0.014}_{-0.015}$	0.960 ± 0.014	0.964 ± 0.014	0.960 ± 0.013
Section 3.1.3	Running	n_s	$1.031^{+0.054}_{-0.055}$ [e]	$1.059^{+0.051}_{-0.049}$	1.031 ± 0.049	$1.017^{+0.042}_{-0.043}$ [f]
		$dn_s/d\ln k$	-0.037 ± 0.028	-0.053 ± 0.025	$-0.035^{+0.024}_{-0.025}$	-0.028 ± 0.020[g]
Section 3.2.4	Tensor	n_s	0.986 ± 0.022	0.979 ± 0.020	$0.985^{+0.019}_{-0.020}$	0.970 ± 0.015
		r	<0.43 (95% CL)	<0.36 (95% CL)	<0.40 (95% CL)	<0.22 (95% CL)
Section 3.2.4	Running	n_s	$1.087^{+0.072}_{-0.073}$	$1.127^{+0.075}_{-0.071}$	$1.083^{+0.063}_{-0.062}$	$1.089^{+0.070}_{-0.068}$
	+Tensor	r	<0.58 (95% CL)	<0.64 (95% CL)	<0.54 (95% CL)	<0.55 (95% CL)[h]
		$dn_s/d\ln k$	-0.050 ± 0.034	$-0.072^{+0.031}_{-0.030}$	-0.048 ± 0.027	-0.053 ± 0.028[i]

Notes.
[a] Defined at $k_0 = 0.002\,\mathrm{Mpc}^{-1}$.
[b] Dunkley et al. (2009).
[c] "CMB" includes the small-scale CMB measurements from CBI (Mason et al. 2003; Sievers et al. 2003, 2007; Pearson et al. 2003; Readhead et al. 2004), VSA (Dickinson et al. 2004), ACBAR (Kuo et al. 2004, 2007), and BOOMERanG (Ruhl et al. 2003; Montroy et al. 2006; Piacentini et al. 2006).
[d] "ACBAR08" is the complete ACBAR data set presented in Reichardt et al. (2008). We used the ACBAR data in the multipole range of $900 < l < 2000$.
[e] At the pivot point for *WMAP* only, $k_{\mathrm{pivot}} = 0.080\,\mathrm{Mpc}^{-1}$, where n_s and $dn_s/d\ln k$ are uncorrelated, $n_s(k_{\mathrm{pivot}}) = 0.963 \pm 0.014$.
[f] At the pivot point for *WMAP*+BAO+SN, $k_{\mathrm{pivot}} = 0.106\,\mathrm{Mpc}^{-1}$, where n_s and $dn_s/d\ln k$ are uncorrelated, $n_s(k_{\mathrm{pivot}}) = 0.961 \pm 0.014$.
[g] With the Lyα forest data (Seljak et al. 2006), $dn_s/d\ln k = -0.012 \pm 0.012$.
[h] With the Lyα forest data (Seljak et al. 2006), $r < 0.28$ (95% CL).
[i] With the Lyα forest data (Seljak et al. 2006), $dn_s/d\ln k = -0.017^{+0.014}_{-0.013}$.

The scale-invariant, Harrison–Zel'dovich–Peebles spectrum, $n_s = 1$, is at 2.5 standard deviations away from the mean of the likelihood for the *WMAP*-only analysis. The significance increases to 3.1 standard deviations for *WMAP*+BAO+SN. Looking at the two-dimensional constraints that include n_s, we find that the most dominant correlation that is still left is the correlation between n_s and $\Omega_b h^2$ (see Figure 1). The larger the $\Omega_b h^2$ is, the smaller the second peak becomes, and the larger the n_s is required to compensate it. Also, the larger the $\Omega_b h^2$ is, the larger the Silk damping (diffusion damping) becomes, and the larger the n_s is required to compensate it.

This argument suggests that the constraint on n_s should improve as we add more information from the small-scale CMB measurements that probe the Silk damping scales; however, the current data do not improve the constraint very much yet: $n_s = 0.960 \pm 0.014$ from *WMAP*+CMB, where "CMB" includes the small-scale CMB measurements from CBI (Mason et al. 2003; Sievers et al. 2003, 2007; Pearson et al. 2003; Readhead et al. 2004), VSA (Dickinson et al. 2004), ACBAR (Kuo et al. 2004, 2007), and BOOMERanG (Ruhl et al. 2003; Montroy et al. 2006; Piacentini et al. 2006), all of which go well beyond the *WMAP* angular resolution, so that their small-scale data are statistically independent of the *WMAP* data.

We find that the small-scale CMB data do not improve the determination of n_s because of their relatively large statistical errors. We also find that the calibration and beam errors are important. Let us examine this using the latest ACBAR data (Reichardt et al. 2008). The *WMAP*+ACBAR yields 0.964 ± 0.014. When the beam error of ACBAR is ignored, we find $n_s = 0.964 \pm 0.013$. When the calibration error is ignored, we find $n_s = 0.962 \pm 0.013$. Therefore, both the beam and calibration error are important in the error budget of the ACBAR data.

The Big Bang nucleosynthesis (BBN), combined with measurements of the deuterium-to-hydrogen ratio, D/H, from quasar absorption systems, has been extensively used for determining $\Omega_b h^2$, independent of any other cosmological parameters (see Steigman 2007, for a recent summary). The precision of the latest determination of $\Omega_b h^2$ from BBN (Pettini et al. 2008) is comparable to that of the *WMAP* data-only analysis. More precise measurements of D/H will help reduce the correlation between n_s and $\Omega_b h^2$, yielding a better determination of n_s.

There is still a bit of correlation left between n_s and the electron-scattering optical depth, τ (see Figure 1). While a better measurement of τ from future *WMAP* observations as well as the *Planck* satellite should help reduce the uncertainty in n_s via a better measurement of τ, the effect of $\Omega_b h^2$ is much larger.

We find that the other datasets, such as BAO, SN, and the shape of galaxy power spectrum from SDSS or 2dFGRS, do not improve our constraints on n_s, as these datasets are not sensitive to $\Omega_b h^2$ or τ; however, this will change when we include the running index, $dn_s/d\ln k$ (Section 3.1.3) and/or the tensor-to-scalar ratio, r (Section 3.2.4).

3.1.3. Results: Running Index

Next, we explore more general models in which a sizable running index may be generated (we still do not include gravitational waves; see Section 3.2 for the analysis that includes gravitational waves). We find no evidence for $dn_s/d\ln k$ from *WMAP* only, $-0.090 < dn_s/d\ln k < 0.019$ (95% CL), or *WMAP*+BAO+SN $-0.068 < dn_s/d\ln k < 0.012$ (95% CL). The improvement from *WMAP*-only to *WMAP*+BAO+SN is only modest.

We find a slight upward shift from the 3-year result, $dn_s/d\ln k = -0.055^{+0.030}_{-0.031}$ (68% CL; Spergel et al. 2003), to the 5-year result, $dn_s/d\ln k = -0.037 \pm 0.028$ (68% CL; *WMAP* only). This is caused by a combination of three effects:

1. The 3-year number for $dn_s/d\ln k$ was derived from an older analysis pipeline for the temperature data, namely the resolution 3 (instead of 4) pixel-based low-l temperature likelihood and a higher point-source amplitude, $A_{\mathrm{ps}} = 0.017\,\mu\mathrm{K}^2\mathrm{sr}$.
2. With 2 years of more integration, we have a better signal-to-noise near the third acoustic peak, whose amplitude is slightly higher than the 3-year determination (Nolta et al. 2009).

3. With the improved beam model (Hill et al. 2009), the temperature power spectrum at $l \gtrsim 200$ has been raised nearly uniformly by $\sim 2.5\%$ (Hill et al. 2009; Nolta et al. 2009).

All of these effects go in the same direction, that is, to increase the power at high multipoles and reduce a negative running index. We find that these factors contribute to the upward shift in $dn_s/d\ln k$ at comparable levels.

Note that an upward shift in n_s for a power-law model, 0.958 to 0.963 (Section 3.1.2), is not subject to (1) because the 3-year number for n_s was derived from an updated analysis pipeline using the resolution 4 low-l code and $A_{\rm ps} = 0.014\,\mu{\rm K}^2$ sr. We find that (2) and (3) contribute to the shift in n_s at comparable levels. An upward shift in σ_8 from the 3-year value, 0.761, to the 5-year value, 0.796, can be similarly explained.

We do not find any significant evidence for the running index when the *WMAP* data and small-scale CMB data (CBI, VSA, ACBAR07, BOOMERanG) are combined, $-0.1002 < dn_s/d\ln k < -0.0037$ (95% CL), or the *WMAP* data and the latest results from the analysis of the complete ACBAR data (Reichardt et al. 2008) are combined, $-0.082 < dn_s/d\ln k < 0.015$ (95% CL).

Our best 68% CL constraint from *WMAP*+BAO+SN shows no evidence for the running index, $dn_s/d\ln k = -0.028 \pm 0.020$. In order to improve upon the limit on $dn_s/d\ln k$, one needs to determine n_s at small scales, as $dn_s/d\ln k$ is simply given by the difference between n_s's measured at two different scales, divided by the logarithmic separation between two scales. The Lyα forest provides such information (see Section 7; also Table 4).

3.2. Primordial Gravitational Waves

3.2.1. Motivation

The presence of primordial gravitational waves is a robust prediction of inflation models, as the same mechanism that generated primordial density fluctuations should also generate primordial gravitational waves (Grishchuk 1975; Starobinsky 1979). The amplitude of gravitational waves relative to that of density fluctuations is model-dependent.

The primordial gravitational waves leave their signatures imprinted on the CMB temperature anisotropy (Rubakov et al. 1982; Fabbri & Pollock 1983; Abbott & Wise 1984; Starobinsky 1985; Crittenden et al. 1993), as well as on polarization (Basko & Polnarev 1980; Bond & Efstathiou 1984; Polnarev 1985; Crittenden et al. 1993, 1995; Coulson et al. 1994).[20] The spin-2 nature of gravitational waves leads to two types of a polarization pattern on the sky (Zaldarriaga & Seljak 1997; Kamionkowski et al. 1997a): (1) the curl-free mode (E mode), in which the polarization directions are either purely radial or purely tangential to hot/cold spots in temperature, and (2) the divergence-free mode (B mode), in which the pattern formed by polarization directions around hot/cold spots possess nonzero vorticity.

In the usual gravitational instability picture, in the linear regime (before shell crossing of fluid elements), velocity perturbations can be written in terms of solely a gradient of a scalar velocity potential u, $\vec{v} = \vec{\nabla} u$. This means that no vorticity would arise, and, therefore, no B mode polarization can be generated from density or velocity perturbations in the linear regime. However, primordial gravitational waves can generate both E and B mode polarization; thus, the B mode polarization offers a smoking-gun signature for the presence of primordial gravitational waves (Seljak & Zaldarriaga 1997; Kamionkowski et al. 1997a). This gives us a strong motivation to look for signatures of the primordial gravitational waves in CMB.

In Table 4, we summarize our constraints on the amplitude of gravitational waves, expressed in terms of the tensor-to-scalar ratio, r, defined by Equation (20).

3.2.2. Analysis

We quantify the amplitude and spectrum of primordial gravitational waves in the following form:

$$\Delta_h^2(k) \equiv \frac{k^3 P_h(k)}{2\pi^2} = \Delta_h^2(k_0)\left(\frac{k}{k_0}\right)^{n_t}, \tag{16}$$

where we have ignored a possible scale dependence of $n_t(k)$, as the current data cannot constrain it. Here, by $P_h(k)$, we mean

$$\langle \tilde{h}_{ij}(\mathbf{k})\tilde{h}^{ij}(\mathbf{k}')\rangle = (2\pi)^3 P_h(k)\delta^3(\mathbf{k}-\mathbf{k}'), \tag{17}$$

where $\tilde{h}_{ij}(\mathbf{k})$ is the Fourier transform of the tensor metric perturbations, $g_{ij} = a^2(\delta_{ij} + h_{ij})$, which can be further decomposed into the two polarization states (+ and ×) with the appropriate polarization tensor, $e_{ij}^{(+,\times)}$, as

$$\tilde{h}_{ij}(\mathbf{k}) = \tilde{h}_+(\mathbf{k})e_{ij}^+(\mathbf{k}) + \tilde{h}_\times(\mathbf{k})e_{ij}^\times(\mathbf{k}), \tag{18}$$

with the normalization that $e_{ij}^+ e^{+,ij} = e_{ij}^\times e^{\times,ij} = 2$ and $e_{ij}^+ e^{\times,ij} = 0$. Unless there was a parity-violating interaction term such as $f(\phi)R_{\mu\nu\rho\sigma}\tilde{R}^{\mu\nu\rho\sigma}$, where $f(\phi)$ is an arbitrary function of a scalar field, $R_{\mu\nu\rho\sigma}$ is the Riemann tensor, and $\tilde{R}^{\mu\nu\rho\sigma}$ is a dual tensor (Lue et al. 1999), both polarization states are statistically independent with the same amplitude, meaning

$$\langle|\tilde{h}_+|^2\rangle = \langle|\tilde{h}_\times|^2\rangle \equiv \langle|\tilde{h}^2|\rangle, \qquad \langle\tilde{h}_\times\tilde{h}_+^*\rangle = 0. \tag{19}$$

This implies that parity-violating correlations, such as the TB and EB correlations, must vanish. We shall explore such parity-violating correlations in Section 4 in a slightly different context. For limits on the difference between $\langle|\tilde{h}_+|^2\rangle$ and $\langle|\tilde{h}_\times|^2\rangle$ from, respectively, the TB and EB spectra of the *WMAP* 3-year data, see Saito et al. (2007).

In any case, this definition suggests that $P_h(k)$ is given by $P_h(k) = 4\langle|\tilde{h}|^2\rangle$. Notice a factor of 4. This is the definition of $P_h(k)$ that we have been consistently using since the first year release (Peiris et al. 2003; Spergel et al. 2003, 2007; Page et al. 2007). We continue to use this definition.

With this definition of $\Delta_h^2(k)$ (Equation (16)), we define the tensor-to-scalar ratio, r, at $k = k_0$, as

$$r \equiv \frac{\Delta_h^2(k_0)}{\Delta_{\mathcal{R}}^2(k_0)}, \tag{20}$$

where $\Delta_{\mathcal{R}}(k)$ is the curvature perturbation spectrum given by Equation (15). We shall take k_0 to be $0.002\,{\rm Mpc}^{-1}$. In this paper, we sometimes loosely call this quantity the "amplitude of gravitational waves."

What about the tensor spectral tilt, n_t? In single-field inflation models, there exists the so-called consistency relation between r and n_t (see Liddle & Lyth 2000, for a review)

$$n_t = -\frac{r}{8}. \tag{21}$$

[20] See, for example, Watanabe & Komatsu (2006) for the spectrum of the primordial gravitational waves itself.

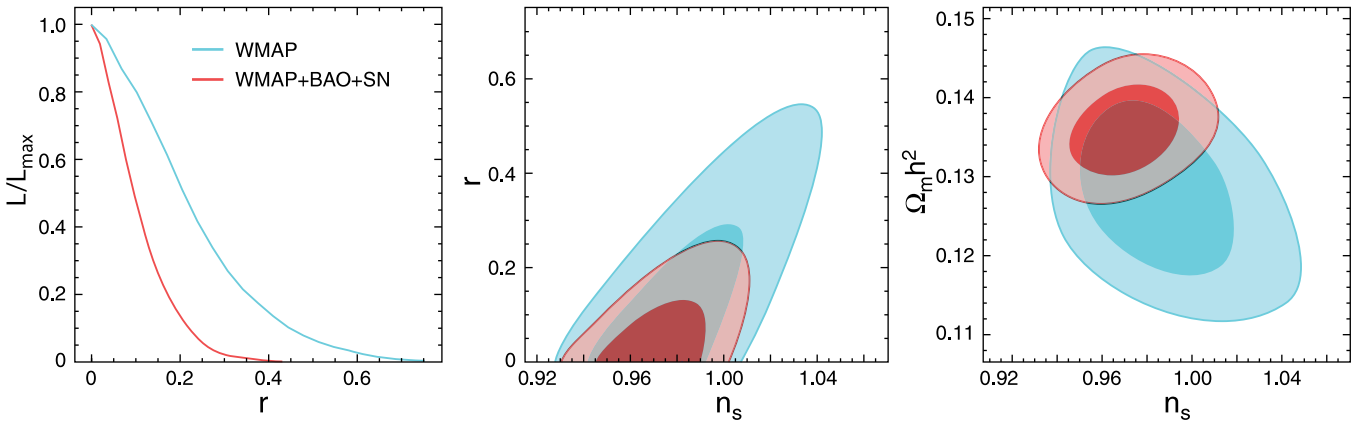

Figure 2. Constraint on the tensor-to-scalar ratio, r, at $k = 0.002\,\mathrm{Mpc}^{-1}$ (Section 3.2.4). No running index is assumed. See Figure 4 for r with the running index. In all panels, we show the *WMAP*-only results in blue and *WMAP*+BAO+SN in red. (Left) One-dimensional marginalized distribution of r, showing the *WMAP*-only limit, $r < 0.43$ (95% CL), and *WMAP*+BAO+SN, $r < 0.22$ (95% CL). (Middle) Joint two-dimensional marginalized distribution (68% and 95% CL), showing a strong correlation between n_s and r. (Right) Correlation between n_s and $\Omega_m h^2$. The BAO and SN data help to break this correlation which, in turn, reduces the correlation between r and n_s, resulting in a factor of 2.2 better limit on r.

In order to reduce the number of parameters, we continue to impose this relation at $k = k_0 = 0.002\,\mathrm{Mpc}^{-1}$. For a discussion on how to impose this constraint in a more self-consistent way, see Peiris & Easther (2006a).

To constrain r, we shall use the *WMAP* 5-year temperature and polarization data, the small-scale CMB data, and/or BAO and SN distance measurements.

3.2.3. How WMAP Constrains the Amplitude of Gravitational Waves

Let us show how the gravitational wave contribution is constrained by the *WMAP* data (see Figure 3). In this pedagogical analysis, we vary only r and τ, while adjusting the overall amplitude of fluctuations such that the height of the first peak of the temperature power spectrum is always held fixed. All the other cosmological parameters are fixed at $\Omega_k = 0$, $\Omega_b h^2 = 0.02265$, $\Omega_c h^2 = 0.1143$, $H_0 = 70.1\,\mathrm{km\,s^{-1}\,Mpc^{-1}}$, and $n_s = 0.960$. Note that the limit on r from this analysis should not be taken as our best limit, as this analysis ignores the correlation between r and the other cosmological parameters, especially n_s. The limit on r from the full analysis will be given in Section 3.2.4.

1. (The gray contours in the left panel and the upper right of the right panel of Figure 3.) The low-l polarization data (TE/EE/BB) at $l \lesssim 10$ are unable to place meaningful limits on r. A large r can be compensated by a small τ, producing nearly the same EE power spectrum at $l \lesssim 10$. (Recall that the gravitational waves also contribute to EE.) As a result, r that is as large as 10 is still allowed within 68% CL.[21]
2. (The red contours in the left panel and the lower left of the right panel of Figure 3.) Such a high value of r, however, produces too negative a TE correlation between $30 \lesssim l \lesssim 150$. Therefore, we can improve the limit on r significantly—by nearly an order of magnitude—by simply using the high-l TE data. The 95% upper bound at this point is still as large as $r \sim 2$.[22]
3. (The blue contours in the left panel and the upper left of the right panel of Figure 3.) Finally, the low-l temperature data at $l \lesssim 30$ severely limit the excess low-l power due to gravitational waves, bringing the upper bound down to $r \sim 0.2$. Note that this bound is about a half of what we actually obtain from the full MCMC of the *WMAP*-only analysis, $r < 0.43$ (95% CL). This is because we have fixed n_s, and thus ignored the correlation between r and n_s shown by Figure 2.

3.2.4. Results

Having understood which parts of the temperature and polarization spectra constrain r, we obtain the upper limit on r from the full exploration of the likelihood space using the MCMC. Figure 2 shows the one-dimensional constraint on r and the two-dimensional constraint on r and n_s, assuming a negligible running index. With the *WMAP* 5-year data alone, we find $r < 0.43$ (95% CL). Since the B-mode contributes little here, and most of the information essentially comes from TT and TE, our limit on r is highly degenerate with n_s, and thus we can obtain a better limit on r only when we have a better limit on n_s.

When we add BAO and SN data, the limit improves significantly to $r < 0.22$ (95% CL). This is because the distance information from BAO and SN reduces the uncertainty in the matter density, and thus it helps to determine n_s better because n_s is also degenerate with the matter density. This "chain of correlations" helped us improve our limit on r significantly from the previous results. This limit, $r < 0.22$ (95% CL), is the best limit on r to date.[23] With the new data, we are able to get more stringent limits than our earlier analyses (Spergel et al. 2007) that combined the *WMAP* data with measurements of the galaxy power spectrum and found $r < 0.30$ (95% CL).

A dramatic reduction in the uncertainty in r has an important implication for n_s as well. Previously, $n_s > 1$ was within the 95%

[21] We have performed a similar, but different, analysis in Section 6.2 of Page et al. (2007). In this paper, we include both the scalar and tensor contributions to EE, whereas in Page et al. (2007), we have ignored the tensor contribution to EE and found a somewhat tighter limit, $r < 4.5$ (95% CL), from the low-l polarization data. This is because, when the tensor contribution was ignored, the EE polarization could still be used to fix τ, whereas in our case, r and τ are fully degenerate when $r \gtrsim 1$ (see Figure 3), as the EE is also dominated by the tensor contribution for such a high value of r.

[22] See Polnarev et al. (2008); Miller et al. (2007) for a way to constrain r from the TE power spectrum alone.

[23] This is the one-dimensional marginalized 95% limit. From the joint two-dimensional marginalized distribution of n_s and r, we find $r < 0.27$ (95% CL) at $n_s = 0.99$. See Figure 2.

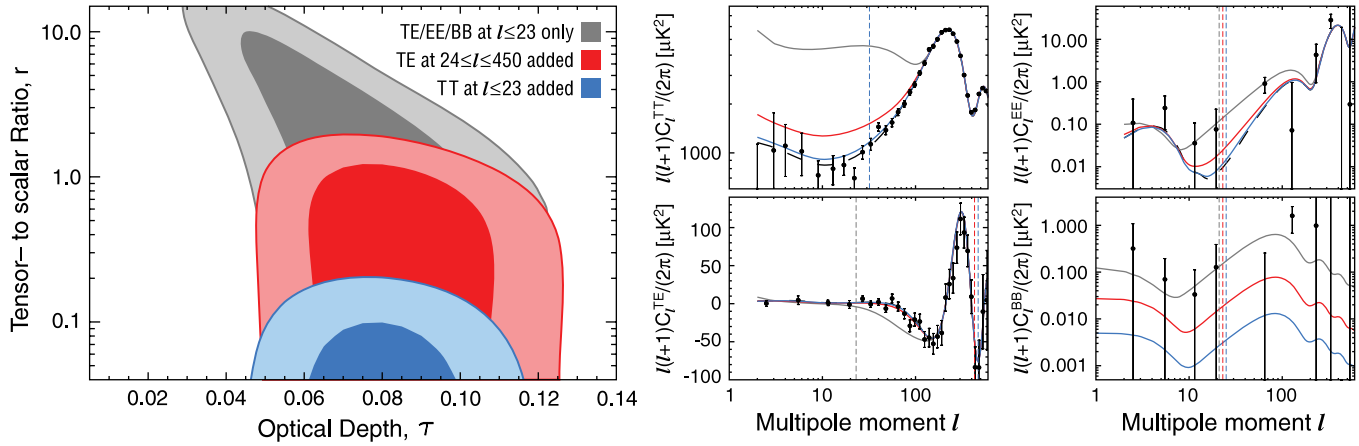

Figure 3. How the *WMAP* temperature and polarization data constrain the tensor-to-scalar ratio, r. (Left) The contours show 68% and 95% CL. The gray region is derived from the low-l polarization data (TE/EE/BB at $l \leqslant 23$) only, the red region from the low-l polarization plus the high-l TE data at $l \leqslant 450$, and the blue region from the low-l polarization, the high-l TE, and the low-l temperature data at $l \leqslant 32$. (Right) The gray curves show $(r, \tau) = (10, 0.050)$, the red curves $(r, \tau) = (1.2, 0.075)$, and the blue curves $(r, \tau) = (0.20, 0.080)$, which are combinations of r and τ that give the upper edge of the 68% CL contours shown on the left panel. The vertical lines indicate the maximum multipoles below which the data are used for each color. The data points with 68% CL errors are the *WMAP* 5-year measurements (Nolta et al. 2009). Note that the BB power spectrum at $l \sim 130$ is consistent with zero within 95% CL.

CL when the gravitational wave contribution was allowed, owing to the correlation between n_s and r. Now, we are beginning to disfavor $n_s > 1$ even when r is nonzero: with *WMAP*+BAO+SN, we find $-0.0022 < 1 - n_s < 0.0589$ (95% CL).[24]

However, these stringent limits on r and n_s weaken to $-0.246 < 1 - n_s < 0.034$ (95% CL) and $r < 0.55$ (95% CL) when a sizable running index is allowed. The BAO and SN data helped reduce the uncertainty in $dn_s/d\ln k$ (Figure 4), but not enough to improve on the other parameters compared to the *WMAP*-only constraints. The Lyα forest data can improve the limit on $dn_s/d\ln k$ even when r is present (see Section 7; also Table 4).

3.3. Implications for Inflation Models

How do the *WMAP* 5-year limits on n_s and r constrain inflationary models?[25] In the context of single-field models, one can write down n_s and r in terms of the derivatives of potential, $V(\phi)$, as (Liddle & Lyth 2000)

$$1 - n_s = 3M_{pl}^2 \left(\frac{V'}{V}\right)^2 - 2M_{pl}^2 \frac{V''}{V}, \tag{22}$$

$$r = 8M_{pl}^2 \left(\frac{V'}{V}\right)^2, \tag{23}$$

where $M_{pl} = 1/\sqrt{8\pi G}$ is the reduced Planck mass, and the derivatives are evaluated at the mean value of the scalar field at the time that a given scale leaves the horizon. These equations may be combined to give a relation between n_s and r:

$$r = \frac{8}{3}(1 - n_s) + \frac{16M_{pl}^2}{3}\frac{V''}{V}. \tag{24}$$

This equation indicates that it is the *curvature* of the potential that divides models on the n_s-r plane; thus, it makes sense to classify inflation models on the basis of the sign and magnitude of the curvature of the potential (Peiris et al. 2003).[26]

What is the implication of our bound on r for inflation models? Equation (24) suggests that a large r can be generated when the curvature of the potential is positive, that is, $V'' > 0$, at the field value that corresponds to the scales probed by the *WMAP* data. Therefore, it is a set of *positive curvature models* that we can constrain from the limit on r. However, negative curvature models are more difficult to constrain from r, as they tend to predict small r (Peiris et al. 2003). We shall not discuss negative curvature models in this paper: many of these models, including those based upon the Coleman–Weinberg potential, fit the *WMAP* data (see, e.g., Dvali et al. 1994; Shafi & Senoguz 2006).

Here we shall pick three simple, but representative, forms of $V(\phi)$ that can produce $V'' > 0$:[27]

1. Monomial (chaotic-type) potential, $V(\phi) \propto \phi^\alpha$. This form of the potential was proposed by, and is best known for, Linde's chaotic inflation models (Linde 1983). This model also approximates a pseudo Nambu–Goldstone boson potential (natural inflation; Freese et al. 1990; Adams et al. 1993) with the negative sign, $V(\phi) \propto 1 - \cos(\phi/f)$, when $\phi/f \ll 1$, or with the positive sign, $V(\phi) \propto 1 + \cos(\phi/f)$, when $\phi/f \sim 1$.[28] This model can also approximate the Landau–Ginzburg type of spontaneous symmetry breaking potential, $V(\phi) \propto (\phi^2 - v^2)^2$, in the appropriate limits.

[24] This is the one-dimensional marginalized 95% limit. From the joint two-dimensional marginalized distribution of n_s and r, we find $n_s < 1.007$ (95% CL) at $r = 0.2$. See Figure 2.

[25] For recent surveys of inflation models in light of the *WMAP* 3-year data, see Alabidi & Lyth (2006a), Kinney et al. (2006) and Martin & Ringeval (2006).

[26] This classification scheme is similar to, but different from, the most widely used one, which is based upon the field value (small-field, large-field, hybrid) (Dodelson et al. 1997; Kinney 1998).

[27] These choices are used to sample the space of positive curvature models. Realistic potentials may be much more complicated: see, for example, Destri et al. (2008) for the *WMAP* 3-year limits on trinomial potentials. Also, the classification scheme based upon derivatives of potentials sheds little light on the models with noncanonical kinetic terms such as k-inflation (Armendariz-Picon et al. 1999; Garriga & Mukhanov 1999), ghost inflation (Arkani-Hamed et al. 2004), Dirac–Born–Infeld (DBI) inflation (Silverstein & Tong 2004; Alishahiha et al. 2004), or infrared-DBI (IR-DBI) inflation (Chen 2005b, 2005a), as the tilt, n_s, also depends on the derivative of the effective speed of sound of a scalar field (for recent constraints on this class of models from the *WMAP* 3-year data, see Bean et al. 2007a, 2008; Lorenz et al. 2008).

[28] The positive sign case, $V(\phi) \propto 1 + \cos(\phi/f)$, belongs to a negative curvature model when $\phi/f \ll 1$. See Savage et al. (2006) for constraints on this class of models from the *WMAP* 3-year data.

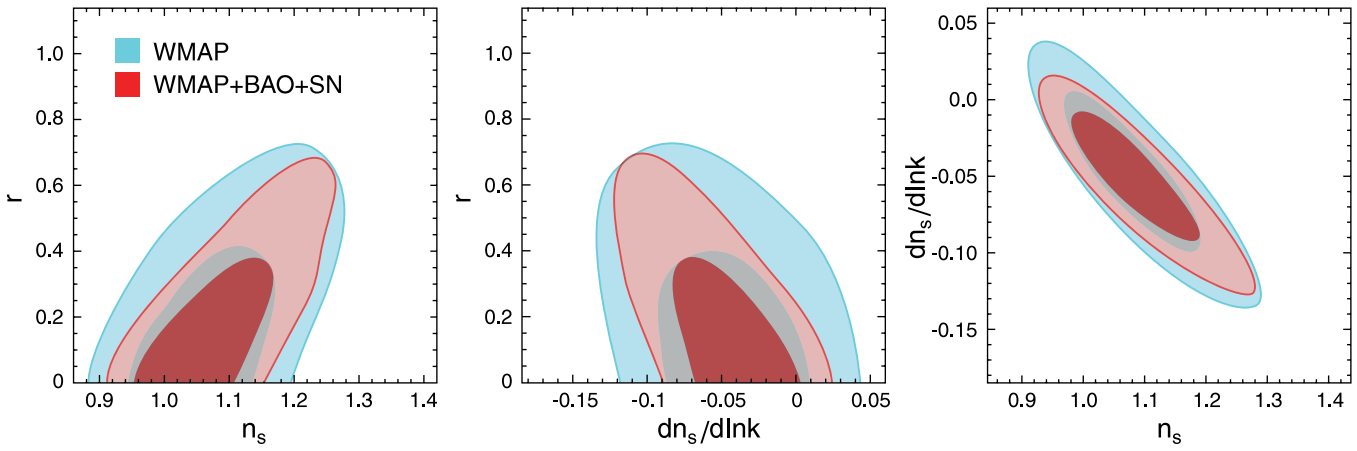

Figure 4. Constraint on the tensor-to-scalar ratio, r, the tilt, n_s, and the running index, $dn_s/d\ln k$, when all of them are allowed to vary (Section 3.2.4). In all panels, we show the *WMAP*-only results in blue and *WMAP*+BAO+SN in red. (Left) Joint two-dimensional marginalized distribution of n_s and r at $k = 0.002\,\mathrm{Mpc}^{-1}$ (68% and 95% CL). (Middle) n_s and $dn_s/d\ln k$. (Right) $dn_s/d\ln k$ and r. We find no evidence for the running index. While the inclusion of the running index weakens our constraint on n_s and r, the data do not support any need for treating the running index as a free parameter: changes in χ^2 between the power-law model and the running model are $\chi^2(\mathrm{running}) - \chi^2(\mathrm{power-law}) \simeq -1.8$ with and without the tensor modes for *WMAP*5+BAO+SN, and 1.2 for *WMAP*5.

2. Exponential potential, $V(\phi) \propto \exp[-(\phi/M_{pl})\sqrt{2/p}]$. A unique feature of this potential is that the dynamics of inflation is exactly solvable, and the solution is a power-law expansion, $a(t) \propto t^p$, rather than an exponential one. For this reason, this type of model is called power-law inflation (Abbott & Wise 1984; Lucchin & Matarrese 1985). They often appear in models of scalar-tensor theories of gravity (Accetta et al. 1985; La & Steinhardt 1989; Futamase & Maeda 1989; Steinhardt & Accetta 1990; Kalara et al. 1990).
3. ϕ^2 plus vacuum energy, $V(\phi) = V_0 + m^2\phi^2/2$. These models are known as Linde's hybrid inflation (Linde 1994). This model is a "hybrid" because the potential combines the chaotic-type (with $\alpha = 2$) with a Higgs-like potential for the second field (which is not shown here). This model behaves as if it were a single-field model until the second field terminates inflation when ϕ reaches some critical value. When $\phi \gg (2V_0)^{1/2}/m$, this model is the same as model 1 with $\alpha = 2$, although one of Linde's motivation was to avoid having such a large field value that exceeds M_{pl}.

These potentials[29] make the following predictions for r and n_s as a function of their parameters:

1. $r = 8(1-n_s)\frac{\alpha}{\alpha+2}$
2. $r = 8(1-n_s)$
3. $r = 8(1-n_s)\frac{\tilde{\phi}^2}{2\tilde{\phi}^2-1}$.

Here, for 3, we have defined a dimensionless variable, $\tilde{\phi} \equiv m\phi/(2V_0)^{1/2}$. This model approaches model 1 with $\alpha = 2$ for $\tilde{\phi} \gg 1$ and yields the scale-invariant spectrum, $n_s = 1$, when $\tilde{\phi} = 1/\sqrt{2}$.

We summarize our findings below, and in Figure 5.

1. Assuming that the monomial potentials are valid to the end of inflation including the reheating of the universe, one can relate n_s and r to the number of e-folds of inflation, $N \equiv \ln(a_{\mathrm{end}}/a_{WMAP})$, between the expansion factors at the end of inflation, a_{end}, and the epoch when the wavelength of fluctuations that we probe with *WMAP* leave the horizon during inflation, a_{WMAP}. The relations are (Liddle & Lyth 2000)

$$r = \frac{4\alpha}{N}, \qquad 1 - n_s = \frac{\alpha+2}{2N}. \tag{25}$$

We take $N = 50$ and 60 as a reasonable range (Liddle & Leach 2003). For $\alpha = 4$, that is, inflation by a massless self-interacting scalar field $V(\phi) = (\lambda/4)\phi^4$, we find that both $N = 50$ and 60 are far away from the 95% region and they are excluded convincingly at more than 99% CL. For $\alpha = 2$, that is, inflation by a massive free scalar field $V(\phi) = (1/2)m^2\phi^2$, the model with $N = 50$ lies outside of the 68% region, whereas the model with $N = 60$ is at the boundary of the 68% region. Therefore, both of these models are consistent with the data within the 95% CL. While this limit applies to a single massive free field, Easther & McAllister (2006) showed that a model with many massive axion fields (N-flation model; Dimopoulos et al. 2005) can shift the predicted n_s further away from unity,

$$1 - n_s^{\mathrm{N.f.}} = \left(1 - n_s^{\mathrm{s.f.}}\right)\left(1 + \frac{\beta}{2}\right), \tag{26}$$

where "N.f" refers to "N fields" and "s.f." to "single field," and β is a free parameter of the model. Easther & McAllister (2006) argued that $\beta \sim 1/2$ is favored, for which $1 - n_s$ is larger than the single-field prediction by as much as 25%. The prediction for the tensor-to-scalar ratio, r, is the same as the single-field case (Alabidi & Lyth 2006b). Therefore, this model lies outside of the 95% region for $N = 50$. As usual, however, these monomial potentials can be made a better fit to the data by invoking a nonminimal coupling between the inflaton and gravity, as the nonminimal coupling can reduce r to negligible levels (Komatsu & Futamase 1999; Hwang & Noh 1998; Tsujikawa & Gumjudpai 2004). Piao (2006) has shown that N-flation models with monomial potentials, $V(\phi) \propto \phi^\alpha$, generically predict n_s that is smaller than the corresponding single-field predictions.
2. For an exponential potential, r and n_s are uniquely determined by a single parameter, p, that determines a power-law index of the expansion factor, $a(t) \propto t^p$, as

$$r = \frac{16}{p}, \qquad 1 - n_s = \frac{2}{p}. \tag{27}$$

[29] In the language of Section 3.4 of Peiris et al. (2003), the models 1 and 2 belong to "small positive curvature models," and model 3 to "large positive curvature models" for $\tilde{\phi} \ll 1$, "small positive curvature models" for $\tilde{\phi} \gg 1$, and "intermediate positive curvature models" for $\tilde{\phi} \sim 1$.

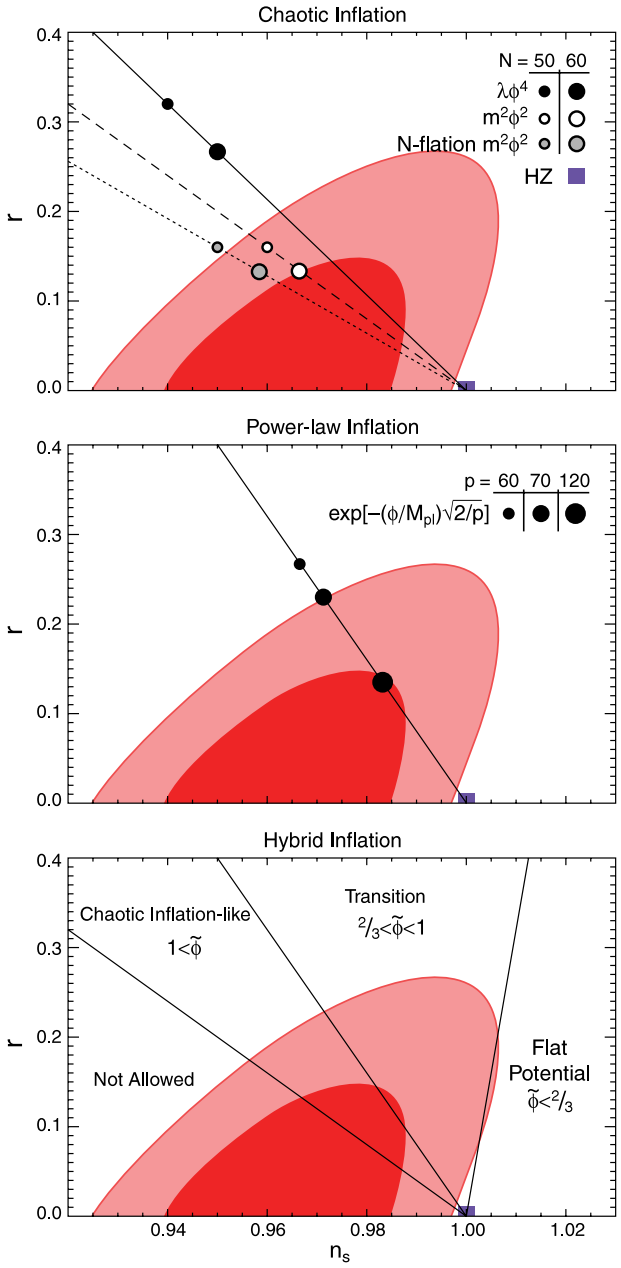

Figure 5. Constraint on three representative inflation models whose potential is positively curved, $V'' > 0$ (Section 3.3). The contours show the 68% and 95% CL derived from *WMAP*+BAO+SN. (Top) The monomial, chaotic-type potential, $V(\phi) \propto \phi^{\alpha}$ (Linde 1983), with $\alpha = 4$ (solid) and $\alpha = 2$ (dashed) for single-field models, and $\alpha = 2$ for multiaxion field models with $\beta = 1/2$ (Easther & McAllister 2006; dotted). The symbols show the predictions from each of these models with the number of e-folds of inflation equal to 50 and 60. The $\lambda\phi^4$ potential is excluded convincingly, the $m^2\phi^2$ single-field model lies outside of (at the boundary of) the 68% region for $N = 50$ (60), and the $m^2\phi^2$ multiaxion model with $N = 50$ lies outside of the 95% region. (Middle) The exponential potential, $V(\phi) \propto \exp[-(\phi/M_{pl})\sqrt{2/p}]$, which leads to a power-law inflation, $a(t) \propto t^p$ (Abbott & Wise 1984; Lucchin & Matarrese 1985). All models but $p \sim 120$ are outside of the 68% region. The models with $p < 60$ are excluded at more than 99% CL, and those with $p < 70$ are outside of the 95% region. For multifield models these limits can be translated into the number of fields as $p \rightarrow np_i$, where p_i is the p-parameter of each field (Liddle et al. 1998). The data favor $n \sim 120/p_i$ fields. (Bottom) The hybrid-type potential, $V(\phi) = V_0 + (1/2)m^2\phi^2 = V_0(1 + \tilde{\phi}^2)$, where $\tilde{\phi} \equiv m\phi/(2V_0)^{1/2}$ (Linde 1994). The models with $\tilde{\phi} < 2/3$ drive inflation by the vacuum energy term, V_0, and are disfavored at more than 95% CL, while those with $\tilde{\phi} > 1$ drive inflation by the quadratic term, and are similar to the chaotic type (the left panel with $\alpha = 2$). The transition regime, $2/3 < \tilde{\phi} < 1$ are outside of the 68% region, but still within the 95% region.

We find that $p < 60$ is excluded at more than 99% CL, $60 < p < 70$ is within the 99% region but outside of the 95% region, and $p > 70$ is within the 95% region. The models with $p \sim 120$ lie on the boundary of the 68% region, but other parameters are not within the 68% CL. This model can be thought of as a single-field inflation with $p \gg 1$, or multifield inflation with n fields, each having $p_i \sim 1$ or even $p_i < 1$ (assisted inflation; Liddle et al. 1998). In this context, therefore, one can translate the above limits on p into the limits on the number of fields. The data favor $n \sim 120/p_i$ fields.

3. For this model, we can divide the parameter space into three regions, depending upon the value of $\tilde{\phi}$ that corresponds to the field value when the wavelength of fluctuations that we probe with *WMAP* leaves the horizon. When $\tilde{\phi} \ll 1$, the potential is dominated by a constant term, which we call "Flat Potential Regime." When $\tilde{\phi} \gg 1$, the potential is indistinguishable from the chaotic-type (model 1) with $\alpha = 2$. We call this region "Chaotic Inflation-like Regime." When $\tilde{\phi} \sim 1$, the model shows a transitional behavior, and thus we call it "Transition Regime." We find that the flat potential regime with $\tilde{\phi} \lesssim 2/3$ lies outside of the 95% region. The transition regime with $2/3 \lesssim \tilde{\phi} \lesssim 1$ is within the 95% region, but outside of the 68% region. Finally, the chaotic-like regime contains the 68% region. Since inflation in this model ends by the second field whose dynamics depends on other parameters, there is no constraint from the number of e-folds.

These examples show that the *WMAP* 5-year data, combined with the distance information from BAO and SN, begin to disfavor a number of popular inflation models.

3.4. Curvature of the Observable Universe

3.4.1. Motivation

The flatness of the observable universe is one of the predictions of conventional inflation models. How much curvature can we expect from inflation? The common view is that inflation naturally produces the spatial curvature parameter, Ω_k, on the order of the magnitude of quantum fluctuations, that is, $\Omega_k \sim 10^{-5}$. However, the current limit on Ω_k is of order 10^{-2}; thus, the current data are not capable of reaching the level of Ω_k that is predicted by the common view.

Would a detection of Ω_k rule out inflation? It is possible that the value of Ω_k is just below our current detection limit, even within the context of inflation: inflation may not have lasted for so long, and the curvature radius of our universe may just be large enough for us not to see the evidence for curvature within our measurement accuracy, yet. While this sounds like fine-tuning, it is a possibility.

This is something we can test by constraining Ω_k better. There is also a revived (and growing) interest in measurements of Ω_k, as Ω_k is degenerate with the equation of state of dark energy, w. Therefore, a better determination of Ω_k has an important implication for our ability to constrain the nature of dark energy.

3.4.2. Analysis

Measurements of the CMB power spectrum alone do not strongly constrain Ω_k. More precisely, any experiments that measure the angular diameter or luminosity distance to a *single* redshift are not able to constrain Ω_k uniquely, as the distance depends not only on Ω_k, but also on the expansion history

of the universe. For a universe containing matter and vacuum energy, it is essential to combine *at least two* absolute distance indicators, or the expansion rates, out to different redshifts, in order to constrain the spatial curvature well. Note that CMB is also sensitive to Ω_Λ, via the late-time integrated Sachs–Wolfe (ISW) effect, and to Ω_m, via the signatures of gravitational lensing in the CMB power spectrum. These properties can be used to reduce the correlation between Ω_k and Ω_m (Stompor & Efstathiou 1999) or Ω_Λ (Ho et al. 2008; Giannantonio et al. 2008).

It has been pointed out by a number of people (e.g., Eisenstein et al. 2005) that a combination of distance measurements from BAO and CMB is a powerful way to constrain Ω_k. One needs more distances, if dark energy is not a constant but dynamical.

In this section, we shall make one important assumption that the dark energy component is vacuum energy, that is, a cosmological constant. In Section 5, we shall study the case in which the equation of state, w, and Ω_k are varied simultaneously.

3.4.3. Results

Figure 6 shows the limits on Ω_Λ and Ω_k. While the *WMAP* data alone cannot constrain Ω_k (see the left panel), the *WMAP* data combined with the *HST*'s constraint on H_0 tighten the constraint significantly, to $-0.052 < \Omega_k < 0.013$ (95% CL). The *WMAP* data combined with SN yield $\sim$ 50% better limits, $-0.0316 < \Omega_k < 0.0078$ (95% CL), compared to *WMAP+HST*. Finally, the *WMAP*+BAO yields the smallest statistical uncertainty, $-0.0170 < \Omega_k < 0.0068$ (95% CL), which is a factor of 2.6 and 1.7 better than *WMAP+HST* and *WMAP*+SN, respectively. This shows how powerful the BAO is in terms of constraining the spatial curvature of the universe; however, this statement needs to be re-evaluated when dynamical dark energy is considered, for example, $w \neq -1$. We shall come back to this point in Section 5.

Finally, when *WMAP*, BAO, and SN are combined, we find $-0.0178 < \Omega_k < 0.0066$ (95% CL). As one can see from the right panel of Figure 6, the constraint on Ω_k is totally dominated by that from *WMAP*+BAO; thus, the size of the uncertainty does not change very much from *WMAP*+BAO to *WMAP*+BAO+SN. Note that the above result indicates that we have reached 1.3% accuracy (95% CL) in determining Ω_k, which is rather good. The future BAO surveys at $z \sim 3$ are expected to yield an order of magnitude better determination, that is, 0.1% level, of Ω_k (Knox 2006).

It is instructive to convert our limit on Ω_k to the limits on the curvature radius of the universe. As Ω_k is defined as $\Omega_k = -kc^2/\left(H_0^2 R_{\rm curv}^2\right)$, where $R_{\rm curv}$ is the present-day curvature radius, one can convert the upper bounds on Ω_k into the lower bounds on $R_{\rm curv}$, as $R_{\rm curv} = (c/H_0)/\sqrt{|\Omega_k|} = 3/\sqrt{|\Omega_k|}\, h^{-1}$ Gpc. For negatively curved universes, we find $R_{\rm curv} > 37\, h^{-1}$ Gpc, whereas for positively curved universes, $R_{\rm curv} > 22\, h^{-1}$ Gpc. Incidentally these values are greater than the particle horizon at present, $9.7\, h^{-1}$ Gpc (computed for the same model).

The 68% limits from the 3-year data (Spergel et al. 2007) were $\Omega_k = -0.012 \pm 0.010$ from *WMAP*-3 yr+BAO (where BAO is from the SDSS LRG of Eisenstein et al. (2005)), and $\Omega_k = -0.011 \pm 0.011$ from *WMAP*-3 yr+SN (where SN is from the SNLS data of Astier et al. 2006). The 68% limit from *WMAP*-5 yr+BAO+SN (where both BAO and SN have more data than for the 3-year analysis) is $\Omega_k = -0.0050^{+0.0061}_{-0.0060}$. A significant improvement in the constraint is due to a combination of the better *WMAP*, BAO, and SN data.

We conclude that, *if* dark energy is vacuum energy (cosmological constant) with $w = -1$, we do not find any deviation from a spatially flat universe.

3.4.4. Implications for the Duration of Inflation

What does this imply for inflation? Since we do not detect any finite curvature radius, inflation had to last for a long enough period in order to make the observable universe sufficiently flat within the observational limits. This argument allows us to find a lower bound on the *total* number of e-foldings of the expansion factor during inflation, from the beginning to the end, $N_{\rm tot} \equiv \ln(a_{\rm end}/a_{\rm begin})$ (see also Section 4.1 of Weinberg 2008).

When the curvature parameter, Ω_k, is much smaller than unity, it evolves with the expansion factor, a, as $\Omega_k \propto a^{-2}$, a^2, and a during inflation, radiation, and matter era, respectively. Therefore, the observed Ω_k is related to Ω_k at the beginning of inflation as[30]

$$\frac{\Omega_k^{\rm obs}}{\Omega_k^{\rm begin}} = \left(\frac{a_{\rm today}}{a_{\rm eq}}\right)\left(\frac{a_{\rm eq}}{a_{\rm end}}\right)^2\left(\frac{a_{\rm begin}}{a_{\rm end}}\right)^2 \tag{28}$$

$$= (1+z_{\rm eq})\left(\frac{T_{\rm end} g_{*,\rm end}^{1/3}}{T_{\rm eq} g_{*,\rm eq}^{1/3}}\right)^2 e^{-2N_{\rm tot}}, \tag{29}$$

where g_* is the effective number of relativistic dof contributing to entropy, $z_{\rm eq}$ is the matter–radiation equality redshift, and $T_{\rm end}$ and $T_{\rm eq}$ are the reheating temperature of the universe at the end of inflation[31] and the temperature at the equality epoch, respectively. To within 10% accuracy, we take $1 + z_{\rm eq} = 3200$, $T_{\rm eq} = 0.75$ eV, and $g_{*,eq} = 3.9$. We find

$$N_{\rm tot} = 47 - \frac{1}{2}\ln\frac{\Omega_k^{\rm obs}/0.01}{\Omega_k^{\rm begin}} + \ln\frac{T_{\rm end}}{10^8 {\rm GeV}} + \frac{1}{3}\ln\frac{g_{*,\rm end}}{200}. \tag{30}$$

Here, it is plausible that $g_{*,\rm end} \sim 100$ in the standard model of elementary particles, and ~ 200 when the supersymmetric partners are included. The difference between these two cases gives the error of only $\Delta N_{\rm tot} = -0.2$, and thus can be ignored.

The curvature parameter at the beginning of inflation must be below of order unity, as inflation would not begin otherwise. However, it is plausible that $\Omega_k^{\rm begin}$ was not too much smaller than 1; otherwise, we have to explain why it was so small before inflation, and probably we would have to explain it by inflation before inflation. In that case, $N_{\rm tot}$ would refer to the sum of the number of e-foldings from two periods of inflation. From this argument, we shall take $\Omega_k^{\rm begin} \sim 1$.

The reheating temperature can be anywhere between 1 MeV and 10^{16} GeV. It is more likely that it is between 1 TeV and 10^8 GeV for various reasons, but the allowed region is still large. If we scale the result to a reasonably conservative lower limit on the reheating temperature, $T_{\rm end} \sim 1$ TeV, then we find, from our limit on the curvature of the universe,

$$N_{\rm tot} > 36 + \ln\frac{T_{\rm end}}{1{\rm TeV}}. \tag{31}$$

A factor of 10 improvement in the upper limit on $|\Omega_k^{\rm begin}|$ will raise this limit by $\Delta N_{\rm tot} = 1.2$.

[30] To simplify our discussion, we ignore the dark energy contribution, and assume that the universe is dominated matter at the present epoch. This leads to a small error in the estimated lower bound on $N_{\rm tot}$.

[31] For simplicity, we assume that reheating occurred as soon as inflation ended.

Again, $N_{\rm tot}$ here refers to the total number of e-foldings of inflation. In Section 3.3, we use $N \equiv \ln(a_{\rm end}/a_{WMAP})$, which is the number of e-foldings between the end of inflation and the epoch when the wavelength of fluctuations that we probe with *WMAP* leaves the horizon during inflation. Therefore, by definition, N is less than $N_{\rm tot}$.

3.5. Primordial Non-Gaussianity

3.5.1. Motivation and Background

In the simplest model of inflation, the distribution of primordial fluctuations is close to a Gaussian with random phases. The level of deviation from a Gaussian distribution and random phases, called *non-Gaussianity*, predicted by the simplest model of inflation is well below the current limit of measurement. Thus, any detection of non-Gaussianity would be a significant challenge to the currently favored models of the early universe.

The assumption of Gaussianity is motivated by the following view: the probability distribution of quantum fluctuations, $P(\varphi)$, of free scalar fields in the ground state of the Bunch–Davies vacuum, φ, is a Gaussian distribution; thus, the probability distribution of primordial curvature perturbations (in the comoving gauge), $\mathcal{R}$, generated from φ (in the flat gauge) as $\mathcal{R} = -[H(\phi)/\dot{\phi}_0]\varphi$ (Mukhanov & Chibisov 1981; Hawking 1982; Starobinsky 1982; Guth & Pi 1982; Bardeen et al. 1983), would also be a Gaussian distribution. Here, $H(\phi)$ is the expansion rate during inflation and ϕ_0 is the mean field, that is, $\phi = \phi_0 + \varphi$.

This argument suggests that non-Gaussianity can be generated when (a) scalar fields are not free, but have some interactions, (b) there are nonlinear corrections to the relation between $\mathcal{R}$ and φ, and (c) the initial state is not in the Bunch–Davies vacuum.

For (a), one can think of expanding a general scalar field potential $V(\phi)$ to the cubic order or higher, $V(\phi) = \bar{V} + V'\varphi + (1/2)V''\varphi^2 + (1/6)V'''\varphi^3 + \cdots$. The cubic (or higher-order) interaction terms can yield non-Gaussianity in φ (Falk et al. 1993). When perturbations in gravitational fields are included, there are many more interaction terms that arise from expanding the Ricci scalar to the cubic order, with coefficients containing derivatives of V and ϕ_0, such as $\dot{\phi}_0 V''$, $\dot{\phi}_0{}^3/H$, etc. (Maldacena 2003).

For (b), one can think of this relation, $\mathcal{R} = -[H(\phi)/\dot{\phi}_0]\varphi$, as the leading-order term of a Taylor series expansion of the underlying nonlinear (gauge) transformation law between $\mathcal{R}$ and φ. Salopek & Bond (1990) showed that, in the single-field models, $\mathcal{R} = 4\pi G \int_{\phi_0}^{\phi_0+\varphi} d\phi\, (\partial \ln H/\partial\phi)^{-1}$. Therefore, even if φ is precisely Gaussian, $\mathcal{R}$ can be non-Gaussian due to nonlinear terms such as φ^2 in a Taylor series expansion of this relation. One can write this relation in the following form, up to second order in $\mathcal{R}$,

$$\mathcal{R} = \mathcal{R}_{\rm L} - \frac{1}{8\pi G}\left(\frac{\partial^2 \ln H}{\partial\phi^2}\right)\mathcal{R}_{\rm L}^2, \tag{32}$$

where $\mathcal{R}_{\rm L}$ is a linear part of the curvature perturbation. We thus find that the second term makes $\mathcal{R}$ non-Gaussian, even when $\mathcal{R}_{\rm L}$ is precisely Gaussian. This formula has also been found independently by other researchers, extended to multifield cases, and often referred to as the "δN formalism" (Sasaki & Stewart 1996; Lyth et al. 2005; Lyth & Rodriguez 2005).

The observers like us, however, do not measure the primordial curvature perturbations, $\mathcal{R}$, directly. A more observationally-relevant quantity is the curvature perturbation during the matter era, Φ. At the linear order, these quantities are related by $\Phi = (3/5)\mathcal{R}_{\rm L}$ (e.g., Kodama & Sasaki 1984), but the actual relation is more complicated at the nonlinear order (see Bartolo et al. 2004, for a review). In any case, this argument has motivated our defining the "*local* nonlinear coupling parameter," $f_{\rm NL}^{\rm local}$, as (Komatsu & Spergel 2001)[32]

$$\Phi = \Phi_{\rm L} + f_{\rm NL}^{\rm local}\Phi_{\rm L}^2. \tag{33}$$

If we take equation (32), for example, we find $f_{\rm NL}^{\rm local} = -(5/24\pi G)(\partial^2 \ln H/\partial\phi^2)$ (Komatsu 2001). Here, we have followed the terminology proposed by Babich et al. (2004) and called $f_{\rm NL}^{\rm local}$ the "local" parameter, as both sides of Equation (33) are evaluated at the same location in space. (Hence, the term "local.")

Let us comment on the magnitude of the second term in Equation (33). Since $\Phi \sim 10^{-5}$, the second term is smaller than the first term by $10^{-5} f_{\rm NL}^{\rm local}$; thus, the second term is only 0.1% of the first term for $f_{\rm NL}^{\rm local} \sim 10^2$. As we shall see below, the existing limits on $f_{\rm NL}^{\rm local}$ have already reached this level of Gaussianity, and thus it is clear that we are already talking about a tiny deviation from Gaussian fluctuations. This limit is actually better than the current limit on the spatial curvature, which is only on the order of 1%. Therefore, Gaussianity tests offer a stringent test of early universe models.

In the context of single-field inflation in which the scalar field slowly rolls down the potential, the quantities, H, V, and ϕ, change slowly. Therefore, one generically expects that $f_{\rm NL}^{\rm local}$ is small, on the order of the so-called slow-roll parameters ϵ and η, which are typically of order 10^{-2} or smaller. In this sense, the single-field, slow-roll inflation models are expected to result in a tiny amount of non-Gaussianity (Salopek & Bond 1990; Falk et al. 1993; Gangui et al. 1994; Maldacena 2003; Acquaviva et al. 2003). These contributions from the epoch of inflation are much smaller than those from the ubiquitous, second-order cosmological perturbations, that is, the nonlinear corrections to the relation between Φ and $\mathcal{R}$, which result in $f_{\rm NL}^{\rm local}$ of order unity (Liguori et al. 2006; Smith & Zaldarriaga 2006). Also see Bartolo et al. (2004) for a review on this subject.

One can use the cosmological observations, such as the CMB data, to constrain $f_{\rm NL}^{\rm local}$ (Verde et al. 2000; Komatsu & Spergel 2001). While the temperature anisotropy, $\Delta T/T$, is related to Φ via the Sachs–Wolfe formula as $\Delta T/T = -\Phi/3$ at the linear order on very large angular scales (Sachs & Wolfe 1967), there are nonlinear corrections (nonlinear Sachs–Wolfe effect, nonlinear Integrated Sachs–Wolfe effect, gravitational lensing, etc.) to this relation, which add terms of order unity to $f_{\rm NL}^{\rm local}$ by the time we observe it in CMB (Pyne & Carroll 1996; Mollerach & Matarrese 1997). On smaller angular scales, one must include the effects of acoustic oscillations of photon-baryon plasma by solving the Boltzmann equations. The second-order corrections to the Boltzmann equations can also yield $f_{\rm NL}^{\rm local}$ of order unity (Bartolo et al. 2006, 2007).

Any detection of $f_{\rm NL}^{\rm local}$ at the level that is currently accessible would have a profound implication for the physics of inflation. How can a large $f_{\rm NL}^{\rm local}$ be generated? We essentially need to break either (a) single field or (b) slow-roll. For example, a multifield model, known as the curvaton scenario, can result in much larger values of $f_{\rm NL}^{\rm local}$ (Linde & Mukhanov 1997; Lyth

[32] Note that $f_{\rm NL}^{\rm local}$ can be related to the quantities discussed in earlier, pioneering work: $-\Phi_3/2$ (Gangui et al. 1994), $-A_{\rm infl}/2$ (Wang & Kamionkowski 2000), and $-\alpha$ (Verde et al. 2000).

et al. 2003), and so can the models with field-dependent (variable) decay widths for reheating of the universe after inflation (Dvali et al. 2004b, 2004a). A more violent, nonlinear reheating process called "preheating" can give rise to a large $f_{\rm NL}^{\rm local}$ (Enqvist et al. 2005; Jokinen & Mazumdar 2006; Chambers & Rajantie 2008).

Although breaking of slow-roll usually results in a premature termination of inflation, it is possible to break it temporarily for a brief period, without terminating inflation, by some features (steps, dips, etc.) in the shape of the potential. In such a scenario, a large non-Gaussianity may be generated at a certain limited scale at which the feature exists (Kofman et al. 1991; Wang & Kamionkowski 2000; Komatsu et al. 2003). The structure of non-Gaussianity from features is much more complex and model-dependent than $f_{\rm NL}^{\rm local}$ (Chen et al. 2007a, 2008).

There is also a possibility that non-Gaussianity can be used to test alternatives to inflation. In a collapsing universe followed by a bounce (e.g., new Ekpyrotic scenario), $f_{\rm NL}^{\rm local}$ is given by the *inverse* (as well as inverse-squared) of slow-roll parameters; thus, $f_{\rm NL}^{\rm local}$ as large as of order 10–10^2 is a fairly generic prediction of this class of models (Creminelli & Senatore 2007; Koyama et al. 2007; Buchbinder et al. 2008; Lehners & Steinhardt 2008a, 2008b).

Using the angular bispectrum,[33] the harmonic transform of the angular three-point correlation function, Komatsu et al. (2002) have obtained the first observational limit on $f_{\rm NL}^{\rm local}$ from the *COBE* 4-year data (Bennett et al. 1996), finding $-3500 < f_{\rm NL}^{\rm local} < 2000$ (95% CL). The uncertainty was large due to a relatively large beam size of *COBE*, which allowed us to go only to the maximum multipole of $l_{\rm max} = 20$. Since the signal-to-noise ratio of $f_{\rm NL}^{\rm local}$ is proportional to $l_{\rm max}$, it was expected that the *WMAP* data would yield a factor of ~ 50 improvement over the *COBE* data (Komatsu & Spergel 2001).

The full bispectrum analysis was not feasible with the *WMAP* data, as the computational cost scales as $N_{\rm pix}^{5/2}$, where $N_{\rm pix}$ is the number of pixels, which is on the order of millions for the *WMAP* data. The "KSW" estimator (Komatsu et al. 2005) has solved this problem by inventing a cubic statistic that combines the triangle configurations of the bispectrum optimally so that it is maximally sensitive to $f_{\rm NL}^{\rm local}$.[34] The computational cost of the KSW estimator scales as $N_{\rm pix}^{3/2}$. We give a detailed description of the method that we use in this paper in Appendix A.

We have applied this technique to the *WMAP* 1-year and 3-year data, and found $-58 < f_{\rm NL}^{\rm local} < 134$ ($l = 265$; Komatsu et al. 2003) and $-54 < f_{\rm NL}^{\rm local} < 114$ ($l_{\rm max} = 350$; Spergel et al. 2007), respectively, at 95% CL. Creminelli et al. performed an independent analysis of the *WMAP* data and found similar limits: $-27 < f_{\rm NL}^{\rm local} < 121$ ($l_{\rm max} = 335$; Creminelli et al. 2006) and $-36 < f_{\rm NL}^{\rm local} < 100$ ($l = 370$; Creminelli et al. 2007) for the 1-year and 3-year data, respectively. These constraints are slightly better than the *WMAP* team's, as their estimator for $f_{\rm NL}^{\rm local}$ was improved from the original KSW estimator.

While these constraints are obtained from the KSW-like fast bispectrum statistics, many groups have used the *WMAP* data to measure $f_{\rm NL}^{\rm local}$ using various other statistics, such as the Minkowski functionals (Komatsu et al. 2003; Spergel et al. 2007; Gott et al. 2007; Hikage et al. 2008), real-space three-point function (Gaztañaga & Wagg 2003; Chen & Szapudi 2005), integrated bispectrum (Cabella et al. 2006), 2-1 cumulant correlator power spectrum (Chen & Szapudi 2006), local curvature (Cabella et al. 2004), and spherical Mexican hat wavelet (Mukherjee & Wang 2004). The suborbital CMB experiments have also yielded constraints on $f_{\rm NL}^{\rm local}$: MAXIMA (Santos et al. 2003), VSA (Smith et al. 2004), Archeops (Curto et al. 2007), and BOOMERanG (De Troia et al. 2007).

We stress that it is important to use different statistical tools to measure $f_{\rm NL}^{\rm local}$ if any signal is found, as different tools are sensitive to different systematics. The analytical predictions for the Minkowski functionals (Hikage et al. 2006) and the angular trispectrum (the harmonic transform of the angular 4-point correlation function; Okamoto & Hu 2002; Kogo & Komatsu 2006) as a function of $f_{\rm NL}^{\rm local}$ are now available. Studies on the forms of the trispectrum from inflation models have just begun, and some important insights have been obtained (Boubekeur & Lyth 2006; Huang & Shiu 2006; Byrnes et al. 2006; Seery & Lidsey 2007; Seery et al. 2007; Arroja & Koyama 2008). It is now understood that the trispectrum is at least as important as the bispectrum in discriminating inflation models: some models do not produce any bispectra but produce significant trispectra, and other models produce similar amplitudes of the bispectra but produce very different trispectra (Huang & Shiu 2006; Buchbinder et al. 2008).

In this paper, we shall use the estimator that further improves upon Creminelli et al. (2006) by correcting an inadvertent numerical error of a factor of 2 in their derivation (Yadav et al. 2008). Yadav & Wandelt (2008) used this estimator to measure $f_{\rm NL}^{\rm local}$ from the *WMAP* 3-year data. We shall also use the Minkowski functionals to find a limit on $f_{\rm NL}^{\rm local}$.

In addition to $f_{\rm NL}^{\rm local}$, we shall also estimate the "*equilateral* nonlinear coupling parameter," $f_{\rm NL}^{\rm equil}$, which characterizes the amplitude of the three-point function (i.e., the bispectrum) of the equilateral configurations, in which the lengths of all the three wave vectors forming a triangle in Fourier space are equal. This parameter is useful and highly complementary to the local one: while $f_{\rm NL}^{\rm local}$ mainly characterizes the amplitude of the bispectrum of the squeezed configurations, in which two wave vectors are large and nearly equal and the other wave vector is small, and thus it is fairly insensitive to the equilateral configurations, $f_{\rm NL}^{\rm equil}$ is mainly sensitive to the equilateral configurations with little sensitivity to the squeezed configurations. In other words, it is possible that one may detect $f_{\rm NL}^{\rm local}$ without any detection of $f_{\rm NL}^{\rm equil}$ and vice versa.

These two parameters cover a fairly large class of models. For example, $f_{\rm NL}^{\rm equil}$ can be generated from inflation models in which the scalar field takes on the nonstandard (noncanonical) kinetic form, such as $\mathcal{L} = P(X, \phi)$, where $X = (\partial\phi)^2$. In this class of models, the effective sound speed of ϕ can be smaller than the speed of light, $c_s^2 = [1 + 2X(\partial^2 P/\partial X^2)/(\partial P/\partial X)]^{-1} < 1$. While the sign of $f_{\rm NL}^{\rm equil}$ is negative for the DBI inflation, $f_{\rm NL}^{\rm equil} \sim -1/c_s^2 < 0$ in the limit of $c_s \ll 1$, it can be positive or negative for more general models (Seery & Lidsey 2005; Chen et al. 2007b; Cheung et al. 2008; Li et al. 2008). Such models can be realized in the context of String Theory via the noncanonical kinetic action called the DBI form (Alishahiha et al. 2004), and in the context of an IR modification of gravity called the ghost condensation (Arkani-Hamed et al. 2004).

[33] For a pedagogical introduction to the bispectrum (three-point function) and trispectrum (four-point function) and various topics on non-Gaussianity, see Komatsu (2001) and Bartolo et al. (2004).

[34] Since the angular bispectrum is the harmonic transform of the angular three-point function, it forms a triangle in the harmonic space. While there are many possible triangles, the "squeezed triangles," in which the two wave vectors are long and one is short, are most sensitive to $f_{\rm NL}^{\rm local}$ (Babich et al. 2004).

The observational limits on $f_{\rm NL}^{\rm equil}$ have been obtained from the *WMAP* 1-year and 3-year data as $-366 < f_{\rm NL}^{\rm equil} < 238$ ($l = 405$; Creminelli et al. 2006) and $-256 < f_{\rm NL}^{\rm equil} < 332$ ($l_{\rm max} = 475$; Creminelli et al. 2007), respectively.

There are other forms, too. Warm inflation might produce a different form of $f_{\rm NL}$(Moss & Xiong 2007; Moss & Graham 2007). Also, the presence of particles at the beginning of inflation, that is, a departure of the initial state of quantum fluctuations from the Bunch–Davies vacuum, can result in an enhanced non-Gaussianity in the "flattened" triangle configurations (Chen et al. 2007b; Holman & Tolley 2008). We do not consider these forms of non-Gaussianity in this paper.

In this paper, we do not discuss the non-Gaussian signatures that cannot be characterized by $f_{\rm NL}^{\rm local}$, $f_{\rm NL}^{\rm equil}$, or $b_{\rm src}$ (the point-source bispectrum amplitude). There have been many studies on non-Gaussian signatures in the *WMAP* data in various forms (Chiang et al. 2003, 2007; Naselsky et al. 2007; Park 2004; de Oliveira-Costa et al. 2004; Tegmark et al. 2003; Larson & Wandelt 2004; Eriksen et al. 2004a, 2004b, 2004c, 2007a; Copi et al. 2004, 2006, 2007; Schwarz et al. 2004; Gordon et al. 2005; Bielewicz et al. 2005; Jaffe et al. 2005, 2006; Vielva et al. 2004; Cruz et al. 2005, 2006, 2007b, 2007a; Cayón et al. 2005; Bridges et al. 2008; Wiaux et al. 2008; Räth et al. 2007; Land & Magueijo 2005b, 2005a, 2007; Rakić & Schwarz 2007; Park et al. 2007; Bernui et al. 2007; Hajian & Souradeep 2003, 2006; Hajian et al. 2005; Prunet et al. 2005; Hansen et al. 2004a, 2004b), many of which are related to the large-scale features at $l \lesssim 20$. We expect these features to be present in the *WMAP* 5-year temperature map, as the structure of CMB anisotropy in the *WMAP* data on such large angular scales has not changed very much since the 3-year data.

3.5.2. Analysis

The largest concern in measuring primordial non-Gaussianity from the CMB data is the potential contamination from the Galactic diffuse foreground emission. To test how much the results would be affected by this, we measure $f_{\rm NL}$ parameters from the raw temperature maps and from the foreground-reduced maps.

We shall mainly use the *KQ75* mask, the new mask that is recommended for tests of Gaussianity (Gold et al. 2009). The important difference between the new mask and the previous *Kp0* mask (Bennett et al. 2003c) is that the new mask is defined by the *difference* between the *K*-band map and the ILC map, and that between the *Q* band and ILC. Therefore, the CMB signal was absent when the mask was defined, which removes any concerns regarding a potential bias in the distribution of CMB on the masked sky.[35]

To carry out tests of Gaussianity, one should use the *KQ75* mask, which is slightly more conservative than *Kp0*, as the *KQ75* mask cuts slightly more sky: we retain 71.8% of the sky with *KQ75*, while 76.5% with *Kp0*. To see how sensitive we are to the details of the mask, we also tried *Kp0* as well as the new mask that is recommended for the power spectrum analysis, *KQ85*, which retains 81.7% of the sky. The previous mask that corresponds to *KQ85* is the *Kp2* mask, which retains 84.6% of the sky.

In addition, we use the *KQ75p*1 mask, which replaces the point-source mask of *KQ75* with the one that does not mask the sources identified in the *WMAP* K-band data. Our point-source selection at *K* band removes more sources and sky in regions with higher CMB flux. We estimate the amplitude of this bias by using the *KQ75p*1 mask, which does not use any *WMAP* data for the point-source identification. The small change in $f_{\rm NL}^{\rm local}$ shows that this is a small bias.

The unresolved extra-galactic point sources also contribute to the bispectrum (Refregier et al. 2000; Komatsu & Spergel 2001; Argüeso et al. 2003; Serra & Cooray 2008), and they can bias our estimates of primordial non-Gaussianity parameters such as $f_{\rm NL}^{\rm local}$ and $f_{\rm NL}^{\rm equil}$. We estimate the bias by measuring $f_{\rm NL}^{\rm local}$ and $f_{\rm NL}^{\rm equil}$ from Monte Carlo simulations of point sources, and list them as $\Delta f_{\rm NL}^{\rm local}$ and $\Delta f_{\rm NL}^{\rm equil}$ in Tables 5 and 7, respectively. As the errors in these estimates of the bias are limited by the number of Monte Carlo realizations (which is 300), one may obtain a better estimate of the bias using more realizations.

We give a detailed description of our estimators for $f_{\rm NL}^{\rm local}$, $f_{\rm NL}^{\rm equil}$, and $b_{\rm src}$, the amplitude of the point-source bispectrum, as well as of Monte Carlo simulations in Appendix A.

Table 5
Clean-Map Estimates and the Corresponding 68% Intervals of the Local form of Primordial Non-Gaussianity, $f_{\rm NL}^{\rm local}$, the Point-Source Bispectrum Amplitude, $b_{\rm src}$ (in units of $10^{-5}\ \mu{\rm K}^3\ {\rm sr}^2$), and Monte-Carlo Estimates of Bias Due to Point Sources, $\Delta f_{\rm NL}^{\rm local}$

Band	Mask	$l_{\rm max}$	$f_{\rm NL}^{\rm local}$	$\Delta f_{\rm NL}^{\rm local}$	$b_{\rm src}$
V+W	*KQ85*	400	50 ± 29	1 ± 2	0.26 ± 1.5
V+W	*KQ85*	500	61 ± 26	2.5 ± 1.5	0.05 ± 0.50
V+W	*KQ85*	600	68 ± 31	3 ± 2	0.53 ± 0.28
V+W	*KQ85*	700	67 ± 31	3.5 ± 2	0.34 ± 0.20
V+W	*Kp0*	500	61 ± 26	2.5 ± 1.5	
V+W	*KQ75p*1[a]	500	53 ± 28	4 ± 2	
V+W	*KQ75*	400	47 ± 32	3 ± 2	−0.50 ± 1.7
V+W	*KQ75*	500	55 ± 30	4 ± 2	0.15 ± 0.51
V+W	*KQ75*	600	61 ± 36	4 ± 2	0.53 ± 0.30
V+W	*KQ75*	700	58 ± 36	5 ± 2	0.38 ± 0.21

Note. [a] This mask replaces the point-source mask in *KQ75* with the one that does not mask the sources identified in the *WMAP* K-band data.

3.5.3. Results: Bispectrum

In Table 5, we show our measurement of $f_{\rm NL}^{\rm local}$ from the template-cleaned V+W map (Gold et al. 2009) with four different masks, *KQ85*, *Kp0*, *KQ75p*1, and *KQ75*, in the increasing order of the size of the mask. For *KQ85* and *KQ75*, we show the results from different maximum multipoles used in the analysis, $l_{\rm max} = 400$, 500, 600, and 700. The *WMAP* 5-year temperature data are limited by cosmic variance to $l \sim 500$.

We find that both *KQ85* and *Kp0* for $l_{\rm max} = 500$ show evidence for $f_{\rm NL}^{\rm local} > 0$ at more than 95% CL, $9 < f_{\rm NL}^{\rm local} < 113$ (95% CL), before the point-source bias correction, and $6.5 < f_{\rm NL}^{\rm local} < 110.5$ (95% CL) after the correction. For a higher $l_{\rm max}$, $l_{\rm max} = 700$, we still find evidence for $f_{\rm NL}^{\rm local} > 0$, $1.5 < f_{\rm NL}^{\rm local} < 125.5$ (95% CL), after the correction.[36]

[35] Previously, the *Kp0* mask was defined by the K-band map, which contains CMB as well as the foreground emission. By cutting bright pixels in the K-band map, it could be possible to cut also the bright CMB pixels, introducing the negative skewness in the distribution of CMB. Since we did not include isolated "islands" on the high Galactic latitudes, some of which could be bright CMB spots, in the final mask when we defined the *Kp0* mask, the skewness bias mentioned above should not be as large as one would expect, if any. Nevertheless, with the new definition of mask, the masked maps are free from this type of bias. For more details on the definition of the mask, see Gold et al. (2009).

[36] The uncertainty for $l_{\rm max} > 500$ is slightly larger than that for $l_{\rm max} = 500$ due to a small suboptimality of the estimator of $f_{\rm NL}^{\rm local}$ (Yadav et al. 2008).

Table 6
Null Tests, Frequency Dependence, and Raw-Map Estimates of the Local form of Primordial Non-Gaussianity, $f_{\rm NL}^{\rm local}$, for $l_{\rm max} = 500$

Band	Foreground	Mask	$f_{\rm NL}^{\rm local}$
Q−W	Raw	*KQ75*	−0.53 ± 0.22
V−W	Raw	*KQ75*	−0.31 ± 0.23
Q−W	Clean	*KQ75*	0.10 ± 0.22
V−W	Clean	*KQ75*	0.06 ± 0.23
Q	Raw	*KQ75p1*[a]	−42 ± 45
V	Raw	*KQ75p1*	38 ± 34
W	Raw	*KQ75p1*	43 ± 33
Q	Raw	*KQ75*	−42 ± 48
V	Raw	*KQ75*	41 ± 35
W	Raw	*KQ75*	46 ± 35
Q	Clean	*KQ75p1*	9 ± 45
V	Clean	*KQ75p1*	47 ± 34
W	Clean	*KQ75p1*	60 ± 33
Q	Clean	*KQ75*	10 ± 48
V	Clean	*KQ75*	50 ± 35
W	Clean	*KQ75*	62 ± 35
V+W	Raw	*KQ85*	9 ± 26
V+W	Raw	*Kp0*	48 ± 26
V+W	Raw	*KQ75p1*	41 ± 28
V+W	Raw	*KQ75*	43 ± 30

Note. [a] This mask replaces the point-source mask in *KQ75* with the one that does not mask the sources identified in the *WMAP* K-band data.

Table 7
Clean-Map Estimates and the Corresponding 68% Intervals of the Equilateral Form of Primordial Non-Gaussianity, $f_{\rm NL}^{\rm equil}$, and Monte-Carlo Estimates of Bias Due to Point Sources, $\Delta f_{\rm NL}^{\rm equil}$

Band	Mask	$l_{\rm max}$	$f_{\rm NL}^{\rm equil}$	$\Delta f_{\rm NL}^{\rm equil}$
V+W	*KQ75*	400	77 ± 146	9 ± 7
V+W	*KQ75*	500	78 ± 125	14 ± 6
V+W	*KQ75*	600	71 ± 108	27 ± 5
V+W	*KQ75*	700	73 ± 101	22 ± 4

This evidence is, however, reduced when we use larger masks, *KQ75p1* and *KQ75*. For the latter, we find $-5 < f_{\rm NL}^{\rm local} < 115$ (95% CL) before the source bias correction, and $-9 < f_{\rm NL}^{\rm local} < 111$ (95% CL) after the correction, which we take as our best estimate. This estimate improves upon our previous estimate from the 3-year data, $-54 < f_{\rm NL}^{\rm local} < 114$ (95% CL; Spergel et al. 2007, for $l = 350$), by cutting much of the allowed region for $f_{\rm NL}^{\rm local} < 0$. To test whether the evidence for $f_{\rm NL}^{\rm local} > 0$ can also be seen with the *KQ75* mask, we need more years of *WMAP* observations.

Let us study the effect of mask further. We find that the central value of $f_{\rm NL}^{\rm local}$ (without the source correction) changes from 61 for *KQ85* to 55 for *KQ75* at $l_{\rm max} = 500$. Is this change expected? To study this, we have computed $f_{\rm NL}^{\rm local}$ from each of the Monte Carlo realizations using *KQ85* and *KQ75*. We find the root mean square (rms) scatter of $\langle (f_{\rm NL}^{{\rm local}\,KQ85} - f_{\rm NL}^{{\rm local}\,KQ75})^2 \rangle_{\rm MC}^{1/2} = 13$, 12, 15, and 15, for $l_{\rm max} = 400$, 500, 600, and 700, respectively. Therefore, the change in $f_{\rm NL}^{\rm local}$ measured from the *WMAP* data is consistent with a statistical fluctuation. For the other masks at $l_{max} = 500$, we find $\langle (f_{\rm NL}^{{\rm local}\,Kp0} - f_{\rm NL}^{{\rm local}\,KQ75})^2 \rangle_{\rm MC}^{1/2} = 9.7$ and $\langle (f_{\rm NL}^{{\rm local}\,KQ75p1} - f_{\rm NL}^{{\rm local}\,KQ75})^2 \rangle_{\rm MC}^{1/2} = 4.0$.

In Table 6, we summarize the results from various tests. As a null test, we have measured $f_{\rm NL}^{\rm local}$ from the difference maps such as Q−W and V−W, which are sensitive to non-Gaussianity in noise and the residual foreground emission, respectively. Since the difference maps do not contain the CMB signal, which is a source of a large cosmic variance in the estimation of $f_{\rm NL}^{\rm local}$, the errors in the estimated $f_{\rm NL}^{\rm local}$ are much smaller. Before the foreground cleaning ("Raw" in the second column), we see negative values of $f_{\rm NL}^{\rm local}$, which is consistent with the foreground emission having positively skewed temperature distribution and $f_{\rm NL}^{\rm local} > 0$ mainly generating negative skewness. We do not find any significant signal of $f_{\rm NL}^{\rm local}$ at more than 99% CL for raw maps, or at more than 68% CL for cleaned maps, which indicates that the temperature maps are quite clean outside of the *KQ75* mask.

From the results presented in Table 6, we find that the raw-map results yield more scatter in $f_{\rm NL}^{\rm local}$ estimated from various data combinations than the clean-map results. From these studies, we conclude that the clean-map results are robust against the data combinations, as long as we use only the V- and W-band data.

In Table 7, we show the equilateral bispectrum, $f_{\rm NL}^{\rm equil}$, from the template-cleaned V+W map with the *KQ75* mask. We find that the point-source bias is much more significant for $f_{\rm NL}^{\rm equil}$: we detect the bias in $f_{\rm NL}^{\rm equil}$ at more than the 5σ level for $l_{\rm max} = 600$ and 700. After correcting for the bias, we find $-151 < f_{\rm NL}^{\rm equil} < 253$ (95% CL; $l_{\rm max} = 700$) as our best estimate. Our estimate improves upon the previous one, $-256 < f_{\rm NL}^{\rm equil} < 332$ (95% CL; Creminelli et al. 2006, for $l = 475$), by reducing the allowed region from both above and below by a similar amount.

Finally, the bispectrum from very high multipoles, for example, $l_{\rm max} = 900$, can be used to estimate the amplitude of residual point-source contamination. One can use this information to check for a consistency between the estimate of the residual point sources from the power spectrum and that from the bispectrum. In Table 8, we list our estimates of $b_{\rm src}$. The raw maps and cleaned maps yield somewhat different values, indicating a possible leakage from the diffuse foreground to an estimate of

Table 8
Point-Source Bispectrum Amplitude, $b_{\rm src}$, for $l_{\rm max} = 900$

Band	Foreground	Mask	$b_{\rm src}$ ($10^{-5}\,\mu{\rm K}^3\,{\rm sr}^2$)
Q	Raw	*KQ75p1*[a]	11.1 ± 1.3
V	Raw	*KQ75p1*	0.83 ± 0.31
W	Raw	*KQ75p1*	0.16 ± 0.24
V+W	Raw	*KQ75p1*	0.28 ± 0.16
Q	Raw	*KQ75*	6.0 ± 1.3
V	Raw	*KQ75*	0.43 ± 0.31
W	Raw	*KQ75*	0.12 ± 0.24
V+W	Raw	*KQ75*	0.14 ± 0.16
V+W	Raw	*KQ85*	0.20 ± 0.15
Q	Clean	*KQ75p1*	8.7 ± 1.3
V	Clean	*KQ75p1*	0.75 ± 0.31
W	Clean	*KQ75p1*	0.16 ± 0.24
V+W	Clean	*KQ75p1*	0.28 ± 0.16
Q	Clean	*KQ75*	4.3 ± 1.3
V	Clean	*KQ75*	0.36 ± 0.31
W	Clean	*KQ75*	0.13 ± 0.24
V+W	Clean	*KQ75*	0.14 ± 0.16
V+W	Clean	*KQ85*	0.13 ± 0.15

Note.
[a] This mask replaces the point-source mask in *KQ75* with the one that does not mask the sources identified in the *WMAP* K-band data.

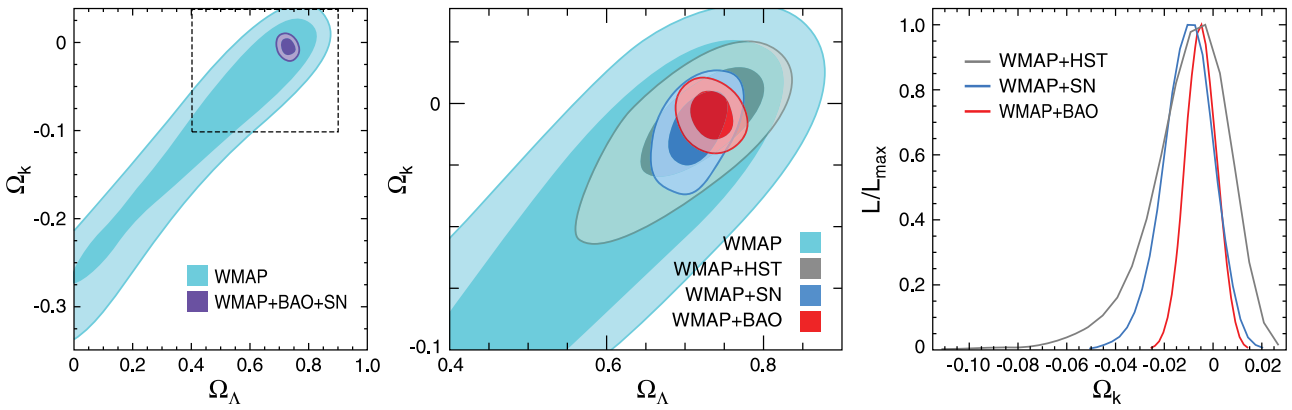

Figure 6. Joint two-dimensional marginalized constraint on the vacuum energy density, Ω_Λ, and the spatial curvature parameter, Ω_k (Section 3.4.3). The contours show the 68% and 95% CL. (Left) The *WMAP*-only constraint (light blue) compared with *WMAP*+BAO+SN (purple). Note that we have a prior on Ω_Λ, $\Omega_\Lambda > 0$. This figure shows how powerful the extra distance information is for constraining Ω_k. (Middle) A blow-up of the region within the dashed lines in the left panel, showing *WMAP*-only (light blue), *WMAP+HST* (gray), *WMAP*+SN (dark blue), and *WMAP*+BAO (red). The BAO provides the most stringent constraint on Ω_k. (Right) One-dimensional marginalized constraint on Ω_k from *WMAP+HST*, *WMAP*+SN, and *WMAP*+BAO. We find the best limit, $-0.0178 < \Omega_k < 0.0066$ (95% CL), from *WMAP*+BAO+SN, which is essentially the same as *WMAP*+BAO. See Figure 12 for the constraints on Ω_k when dark energy is dynamical, that is, $w \neq -1$, with time-independent w. Note that neither BAO nor SN alone is able to constrain Ω_k: they need the *WMAP* data for lifting the degeneracy. Also note that BAO+SN is unable to lift the degeneracy either, as BAO needs the sound horizon size measured by the *WMAP* data.

Table 9
χ^2 Analysis of the Minkowski Functionals for the Template-Cleaned V+W map

$N_{\rm side}$	χ^2_{WMAP}/dof	$F(> \chi^2_{WMAP})$
256	51.5/45	0.241
128	40.0/45	0.660
64	54.2/45	0.167
32	46.8/45	0.361
16	44.7/45	0.396
8	61.3/45	0.104

Note. The results from the area, contour length, and Euler characteristics are combined.

$b_{\rm src}$. Our best estimate in the Q band is $b_{\rm src} = 4.3 \pm 1.3\,\mu{\rm K}^3\,{\rm sr}^2$ (68% CL). See Nolta et al. (2009) for the comparison between $b_{\rm src}$, $C_{\rm ps}$, and the point-source counts.

Incidentally, we also list $b_{\rm src}$ from the *KQ75p*1 mask, whose source mask is exactly the same as we used for the first-year analysis. We find $b_{\rm src} = 8.7 \pm 1.3\,\mu{\rm K}^3\,{\rm sr}^2$ in the Q band, which is in an excellent agreement with the first-year result, $b_{\rm src} = 9.5 \pm 4.4\,\mu{\rm K}^3\,{\rm sr}^2$ (Komatsu et al. 2003).

3.5.4. Results: Minkowski Functionals

For the analysis of the Minkowski functionals, we follow the method described in Komatsu et al. (2003) and Spergel et al. (2007). In Figure 7, we show all of the three Minkowski functionals (Gott et al. 1990; Mecke et al. 1994; Schmalzing & Buchert 1997; Schmalzing & Gorski 1998; Winitzki & Kosowsky 1998) that one can define on a two-dimensional sphere: the cumulative surface area (bottom), the contour length (middle), and the Euler characteristics (which is also known as the genus; top), as a function the "threshold," ν, which is the number of σ of hot and cold spots, defined by

$$\nu \equiv \frac{\Delta T}{\sigma_0}, \tag{34}$$

where σ_0 is the standard deviation of the temperature data (which includes both signal and noise) at a given resolution of the map that one works with. We compare the Minkowski functionals measured from the *WMAP* data with the mean and dispersion of Gaussian realizations that include CMB signal and noise. We use the *KQ75* mask and the V+W-band map.

While Figure 7 shows the results at resolution 7 ($N_{\rm side} = 128$), we have carried out Gaussianity tests using the Minkowski functionals at six different resolutions from resolution 3 ($N_{\rm side} = 8$) to resolution 8 ($N_{\rm side} = 256$). We find no evidence for departures from Gaussianity at any resolutions, as summarized in Table 9; in this table, we list the values of χ^2 of the Minkowski functionals relative to the Gaussian predictions:

$$\chi^2_{WMAP} = \sum_{ij}\sum_{\nu_1\nu_2}\left[F^i_{WMAP} - \langle F^i_{\rm sim}\rangle\right]_{\nu_1} \times (\Sigma^{-1})^{ij}_{\nu_1\nu_2}\left[F^j_{WMAP} - \langle F^j_{\rm sim}\rangle\right]_{\nu_2}, \tag{35}$$

where F^i_{WMAP} and $F^i_{\rm sim}$ are the ith Minkowski functionals measured from the *WMAP* data and Gaussian simulations, respectively, the angular bracket denotes the average over realizations, and $\Sigma^{ij}_{\nu_1\nu_2}$ is the covariance matrix estimated from the simulations. We use 15 different thresholds from $\nu = -3.5$ to $\nu = +3.5$, as indicated by the symbols in Figure 7, and thus the number of dof in the fit is $15 \times 3 = 45$. We show the values of χ^2_{WMAP} and the dof in the second column, and the probability of having χ^2 that is larger than the measured value, $F(> \chi^2_{WMAP})$, in the third column. The smallest probability is 0.1 (at $N_{\rm side} = 8$), and thus we conclude that the Minkowski functionals measured from the *WMAP* 5-year data are fully consistent with Gaussianity.

What do these results imply for $f^{\rm local}_{\rm NL}$? We find that the absence of non-Gaussianity at $N_{\rm side} = 128$ and 64 gives the 68% limits on $f^{\rm local}_{\rm NL}$ as $f^{\rm local}_{\rm NL} = -57 \pm 60$ and -68 ± 69, respectively. The 95% limit from $N_{\rm side} = 128$ is $-178 < f^{\rm local}_{\rm NL} < 64$. The errors are larger than those from the bispectrum analysis given in Section 3.5.3 by a factor of 2, which is partly because we have not used the Minkowski functional at all six resolutions to constrain $f^{\rm local}_{\rm NL}$. For a combined analysis of the *WMAP* 3-year data, see Hikage et al. (2008).

It is intriguing that the Minkowski functionals prefer a *negative* value of $f^{\rm local}_{\rm NL}$, $f^{\rm local}_{\rm NL} \sim -60$, whereas the bispectrum prefers a *positive* value, $f^{\rm local}_{\rm NL} \sim 60$. In the limit that non-

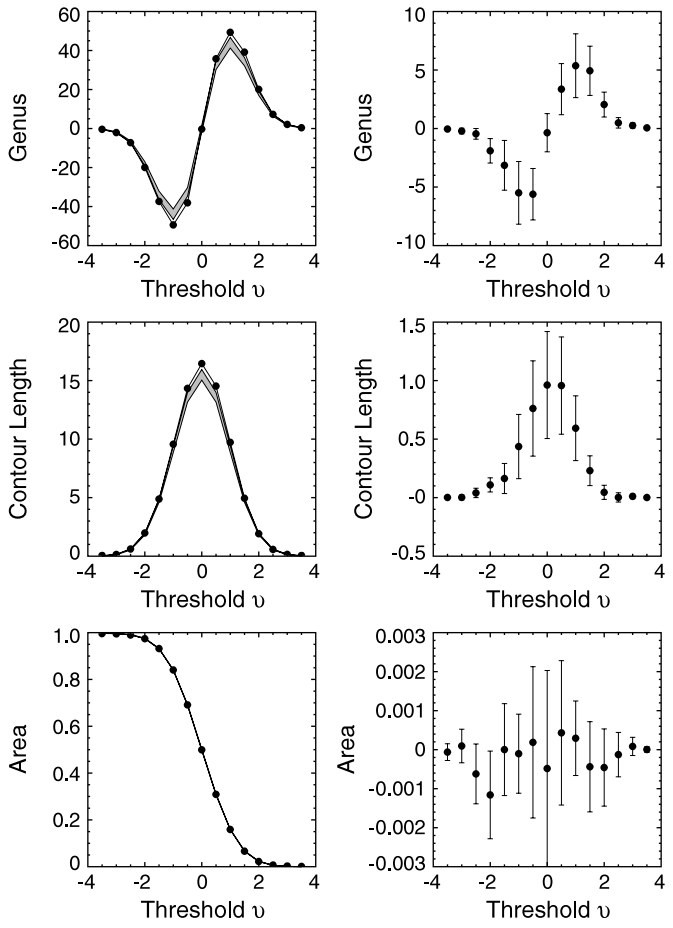

Figure 7. Minkowski functionals from the *WMAP* 5-year data, measured from the template-cleaned V+W map at $N_{\rm side} = 128$ (28′ pixels) outside of the *KQ75* mask. From the top to bottom panels, we show the Euler characteristics (also known as the genus), the contour length, and the cumulative surface area, as a function of the threshold (the number of σ's of hot and cold spots), $\nu \equiv \Delta T/\sigma_0$. (Left) The data (symbols) are fully consistent with the mean and dispersion of Gaussian realizations that include CMB and noise. The gray bands show the 68% intervals of Gaussian realizations. (Right) The residuals between the *WMAP* data and the mean of the Gaussian realizations. Note that the residuals are highly correlated from bin to bin. From this result, we find $f_{\rm NL}^{\rm local} = -57 \pm 60$ (68% CL). From $N_{\rm side} = 64$, we find $f_{\rm NL}^{\rm local} = -68 \pm 69$ (68% CL).

Gaussianity is weak, the Minkowski functionals are sensitive to three "skewness parameters": (1) $\langle(\Delta T)^3\rangle$, (2) $\langle(\Delta T)^2[\partial^2(\Delta T)]\rangle$, and (3) $\langle[\partial(\Delta T)]^2[\partial^2(\Delta T)]\rangle$, all of which can be written in terms of the weighted sum of the bispectrum; thus, the Minkowski functionals are sensitive to some selected configurations of the bispectrum (Hikage et al. 2006). It would be important to study where an apparent "tension" between the Minkowski functionals and the KSW estimator comes from. This example shows how important it is to use different statistical tools to identify the origin of non-Gaussian signals on the sky.

3.6. Adiabaticity of Primordial Fluctuations

3.6.1. Motivation

"Adiabaticity" of primordial fluctuations offers important tests of inflation as well as clues to the origin of matter in the universe. The negative correlation between the temperature and E-mode polarization (TE) at $l \sim 100$ is a generic signature of adiabatic superhorizon fluctuations (Spergel & Zaldarriaga 1997; Peiris et al. 2003). The improved measurement of the TE power spectrum and the temperature power spectrum from the *WMAP* 5-year data, combined with the distance information from BAO and SN, now provide tight limits on deviations of primordial fluctuations from adiabaticity.

Adiabaticity may be loosely defined as the following relation between fluctuations in radiation density and those in matter density:

$$\frac{3\delta\rho_r}{4\rho_r} = \frac{\delta\rho_m}{\rho_m}. \quad (36)$$

This version[37] of the condition guarantees that the entropy density (dominated by radiation, $s_r \propto \rho_r^{3/4}$) per matter particle is unperturbed, that is, $\delta(s_r/n_m) = 0$.

There are two situations in which the adiabatic condition may be satisfied: (1) there is only one degree of freedom in the system, foe example, both radiation and matter were created from decay products of a single scalar field that was solely responsible for generating fluctuations, and (2) matter and radiation were in thermal equilibrium before any nonzero conserving quantum number (such as baryon number minus lepton number, $B-L$) was created (e.g., Weinberg 2004).

Therefore, detection of any nonadiabatic fluctuations, that is, any deviation from the adiabatic condition (Equation (36)), would imply that there were multiple scalar fields during inflation, *and* either matter (baryon or dark matter) was never in thermal equilibrium with radiation, or a nonzero conserving quantum number associated with matter was created well before the era of thermal equilibrium. In any case, the detection of nonadiabatic fluctuations between matter and radiation has a profound implication for the physics of inflation and, perhaps more importantly, the origin of matter.

For example, axions, a good candidate for dark matter, generate nonadiabatic fluctuations between dark matter and photons, as axion density fluctuations could be produced during inflation independent of curvature perturbations (which were generated from inflaton fields, and responsible for CMB anisotropies that we observe today), *and* were not in thermal equilibrium with radiation in the early universe (see Kolb & Turner 1990; Sikivie 2008, for reviews). We can, therefore, place stringent limits on the properties of axions by looking at a signature of deviation from the adiabatic relation in the CMB temperature and polarization anisotropies.

In this paper, we focus on the nonadiabatic perturbations between CDM and CMB photons. Nonadiabatic perturbations between baryons and photons are exactly the same as those between CDM and photons, up to an overall constant; thus, we shall not consider them separately in this paper. For neutrinos and photons, we consider only adiabatic perturbations. In other words, we consider only three standard neutrino species (i.e., no sterile neutrinos) and assume that the neutrinos were in thermal equilibrium before the lepton number was generated.

The basic idea behind this study is not new, and adiabaticity has been extensively constrained using the *WMAP* data since the first-year release, including general (phenomenological) studies without references to specific models (Peiris et al. 2003; Crotty et al. 2003a; Bucher et al. 2004; Moodley et al. 2004; Lazarides et al. 2004; Kurki-Suonio et al. 2005; Beltrán et al. 2005a; Dunkley et al. 2005; Bean et al. 2006; Trotta 2007; Keskitalo et al. 2007), as well as constraints on specific models such as

[37] A more general relation is $\delta\rho_x/\dot\rho_x = \delta\rho_y/\dot\rho_y$, where x and y refer to some energy components. Using the energy conservation equation, $\dot\rho_x = -3H(1+w_x)\rho_x$ (where w_x is the equation of state for the component x), one can recover Equation (36), as $w_r = 1/3$ and $w_m = 0$. For a recent discussion on this topic, see, for example, Weinberg (2003).

double inflation (Silk & Turner 1987; Polarski & Starobinsky 1992, 1994), axion (Weinberg 1978; Wilczek 1978; Seckel & Turner 1985; Linde 1985, 1991; Turner & Wilczek 1991), and curvaton (Lyth & Wands 2003; Moroi & Takahashi 2001, 2002; Bartolo & Liddle 2002), all of which can be constrained from the limits on nonadiabatic fluctuations (Gordon & Lewis 2003; Gordon & Malik 2004; Beltrán et al. 2004, 2005b, 2007; Lazarides 2005; Parkinson et al. 2005; Kawasaki & Sekiguchi 2008).

We shall use the *WMAP* 5-year data, combined with the distance information from BAO and SN, to place more stringent limits on two types of nonadiabatic CDM fluctuations: (1) axion-type and (2) curvaton-type. Our study given below is similar to that by Kawasaki & Sekiguchi (2008) for the *WMAP* 3-year data.

3.6.2. Analysis

We define the nonadiabatic, or entropic, perturbation between the CDM and photons, $\mathcal{S}_{c,\gamma}$, as

$$\mathcal{S}_{c,\gamma} \equiv \frac{\delta\rho_c}{\rho_c} - \frac{3\delta\rho_\gamma}{4\rho_\gamma}, \tag{37}$$

and report on the limits on the ratio of the power spectrum of $\mathcal{S}_{c,\gamma}$, $P_{\mathcal{S}}(k)$, to the curvature perturbation, $P_{\mathcal{R}}(k)$, at a given pivot wavenumber, k_0, given by (e.g., Bean et al. 2006)

$$\frac{\alpha(k_0)}{1-\alpha(k_0)} \equiv \frac{P_{\mathcal{S}}(k_0)}{P_{\mathcal{R}}(k_0)}. \tag{38}$$

We shall take k_0 to be $0.002\,\mathrm{Mpc}^{-1}$.

While α parametrizes the ratio of the entropy power spectrum to the curvature power spectrum, it may be more informative to quantify "how much the adiabatic relation (Equation (36)) can be violated." To quantify this, we introduce the adiabaticity deviation parameter, δ_{adi}, given by

$$\delta_{\mathrm{adi}}^{(c,\gamma)} \equiv \frac{\delta\rho_c/\rho_c - 3\delta\rho_\gamma/(4\rho_\gamma)}{\frac{1}{2}[\delta\rho_c/\rho_c + 3\delta\rho_\gamma/(4\rho_\gamma)]}, \tag{39}$$

which can be used to say, "the deviation from the adiabatic relation between dark matter and photons must be less than $100\delta_{\mathrm{adi}}^{(c,\gamma)}$%." The numerator is just the definition of the entropy perturbation, $\mathcal{S}_{c,\gamma}$, whereas the denominator is given by

$$\frac{1}{2}\left(\frac{\delta\rho_c}{\rho_c} + \frac{3\delta\rho_\gamma}{4\rho_\gamma}\right) = 3\mathcal{R} + O(\mathcal{S}). \tag{40}$$

Therefore, we find, up to the first order in $\mathcal{S}/\mathcal{R}$,

$$\delta_{\mathrm{adi}}^{(c,\gamma)} \approx \frac{\mathcal{S}}{3\mathcal{R}} \approx \frac{\sqrt{\alpha}}{3}, \tag{41}$$

for $\alpha \ll 1$.

There could be a significant correlation between $\mathcal{S}_{c,\gamma}$ and $\mathcal{R}$ (Langlois 1999; Langlois & Riazuelo 2000; Gordon et al. 2001). We take this into account by introducing the cross-correlation coefficient, as

$$-\beta(k_0) \equiv \frac{P_{\mathcal{S},\mathcal{R}}(k_0)}{\sqrt{P_{\mathcal{S}}(k_0)P_{\mathcal{R}}(k_0)}}, \tag{42}$$

where $P_{\mathcal{S},\mathcal{R}}(k)$ is the cross-correlation power spectrum.

Here, we have a negative sign on the left-hand side because of the following reason. In our notation that we used for Gaussianity analysis, the sign convention of the curvature perturbation is such that it gives temperature anisotropy on large scales (the Sachs–Wolfe limit) as $\Delta T/T = -(1/5)\mathcal{R}$. However, those who investigate correlations between $\mathcal{S}$ and $\mathcal{R}$ usually use an opposite sign convention for the curvature perturbation, such that the temperature anisotropy is given by

$$\frac{\Delta T}{T} = \frac{1}{5}\tilde{\mathcal{R}} - \frac{2}{5}\mathcal{S} \tag{43}$$

on large angular scales (Langlois 1999), where $\tilde{\mathcal{R}} \equiv -\mathcal{R}$, and define the correlation coefficient by

$$\beta(k_0) = \frac{P_{\mathcal{S},\tilde{\mathcal{R}}}(k_0)}{\sqrt{P_{\mathcal{S}}(k_0)P_{\tilde{\mathcal{R}}}(k_0)}}. \tag{44}$$

Therefore, in order to use the same sign convention for β as most of the previous work, we shall use Equation (42), and call $\beta = +1$ "totally correlated" and $\beta = -1$ "totally anticorrelated," entropy perturbations.

It is also useful to understand how the correlation or anticorrelation affects the CMB power spectrum at low multipoles. By squaring Equation (43) and taking the average, we obtain

$$\frac{\langle(\Delta T)^2\rangle}{T^2} = \frac{1}{25}\left(P_{\tilde{\mathcal{R}}} + 4P_{\mathcal{S}} - 4\beta\sqrt{P_{\tilde{\mathcal{R}}}P_{\mathcal{S}}(k)}\right). \tag{45}$$

Therefore, the "correlation," $\beta > 0$, reduces the temperature power spectrum on low multipoles, whereas the "anticorrelation," $\beta < 0$, increases the power. This point will become important when we interpret our results: namely, models with $\beta < 0$ will result in a positive correlation between α and n_s (Gordon & Lewis 2003). Note that this property is similar to that of the tensor mode: as the tensor mode adds a significant power only to $l \lesssim 50$, the tensor-to-scalar ratio, r, is degenerate with n_s (see Figure 2).

Finally, we specify the power spectrum of S as a pure power law,

$$P_{\mathcal{S}}(k) \propto k^{m-4}, \qquad P_{\mathcal{S},\mathcal{R}}(k) \propto k^{(m+n_s)/2-4}, \tag{46}$$

in analogy to the curvature power spectrum, $P_{\mathcal{R}}(k) \propto k^{n_s-4}$. Note that β does not depend on k for this choice of $P_{\mathcal{S},\mathcal{R}}(k)$. With this parametrization, it is straightforward to compute the angular power spectra of the temperature and polarization of CMB.

In this paper, we shall pay attention to two limiting cases that are physically motivated: totally uncorrelated ($\beta = 0$) entropy perturbations, axion-type (Seckel & Turner 1985; Linde 1985, 1991; Turner & Wilczek 1991), and totally anticorrelated ($\beta = -1$) entropy perturbations, curvaton-type (Linde & Mukhanov 1997; Lyth & Wands 2003; Moroi & Takahashi 2001, 2002; Bartolo & Liddle 2002). Then, we shall use α_0 to denote α for $\beta = 0$ and α_{-1} for $\beta = -1$.

3.6.3. Results: Implications for Axion

First, let us consider the axion case in which $\mathcal{S}$ and $\mathcal{R}$ are totally uncorrelated, that is, $\beta = 0$. This case represents the entropy perturbation between photons and axions, with axions accounting for some fraction of dark matter in the universe. For simplicity, we take the axion perturbations to be scale invariant, that is, $m = 1$. In Appendix B, we show that this choice corresponds to taking one of the slow-roll parameters,

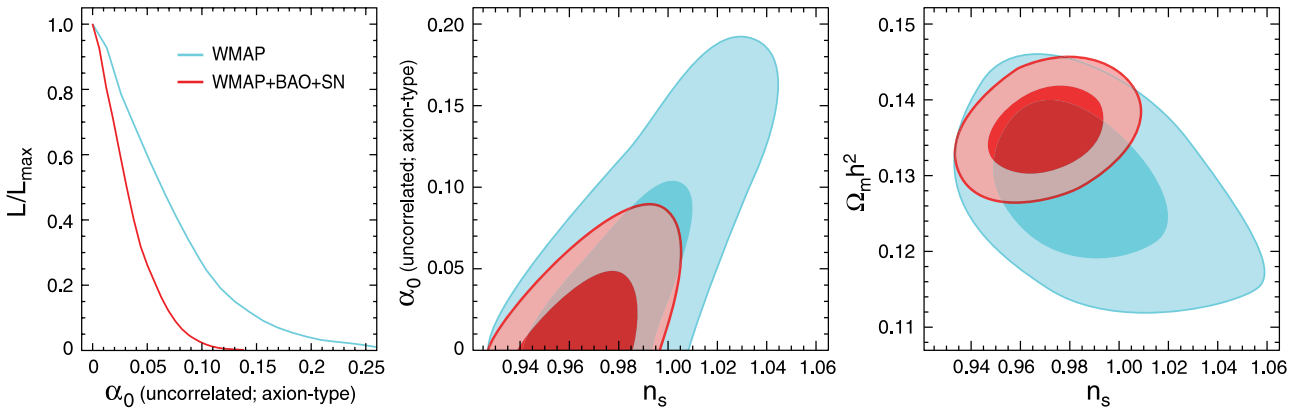

Figure 8. Constraint on the axion entropy perturbation fraction, α_0 (Section 3.6.3). In all panels, we show the *WMAP*-only results in blue and *WMAP*+BAO+SN in red. (Left) One-dimensional marginalized constraint on α_0, showing *WMAP*-only and *WMAP*+BAO+SN. (Middle) Joint two-dimensional marginalized constraint (68% and 95% CL), showing the correlation between α_0 and n_s for *WMAP*-only and *WMAP*+BAO+SN. (Right) Correlation between n_s and $\Omega_m h^2$. The BAO and SN data help to reduce this correlation which, in turn, reduces correlation between α_0 and n_s, resulting in a factor of 2.2 better limit on α_0.

ϵ, to be less than 10^{-2} or adding a tiny amount of gravitational waves, $r \ll 0.1$, which justifies our ignoring gravitational waves in the analysis.

The left panel of Figure 8 shows that we do not find any evidence for the axion entropy perturbations. The limits are $\alpha_0 < 0.16$ (95% CL) and $\alpha_0 < 0.072$ (95% CL) for the *WMAP*-only analysis and *WMAP*+BAO+SN, respectively. The latter limit is the most stringent to date, from which we find the adiabaticity deviation parameter of $\delta^{c,\gamma}_{\rm adi} < 0.089$ (Equation (39)); thus, we conclude that the axion dark matter and photons should obey the adiabatic relation (Equation (36)) to 8.9%, at the 95% CL.

We find that n_s and α_0 are strongly degenerate (see the middle panel of Figure 8). It is easy to understand the direction of correlation. As the entropy perturbation with a scale-invariant spectrum adds power to the temperature anisotropy on large angular scales only, the curvature perturbation tries to compensate it by reducing power on large scales with a larger tilt, n_s. However, since a larger n_s produces too much power on small angular scales, the fitting tries to increase $\Omega_b h^2$ to suppress the second peak and reduce $\Omega_c h^2$ to suppress the third peak. Overall, $\Omega_m h^2$ needs to be reduced to compensate an increase in n_s, as shown in the right panel of Figure 8.

Adding the distance information from the BAO and SN helps to break the correlation between $\Omega_m h^2$ and n_s by constraining $\Omega_m h^2$, independent of n_s. Therefore, with *WMAP*+BAO+SN we find an impressive, factor of 2.2 improvement in the constraint on α_0.

What does this imply for the axions? It has been shown that the limit on the axion entropy perturbation can be used to place a constraint on the energy scale of inflation which, in turn, leads to a stringent constraint on the tensor-to-scalar ratio, r (Kain 2006; Beltrán et al. 2007; Sikivie 2008; Kawasaki & Sekiguchi 2008).

In Appendix B, we study a particular axion cosmology called the "misalignment angle scenario," in which the Pecci–Quinn symmetry breaking occurred during inflation and was never restored after inflation. In other words, we assume that the Pecci–Quinn symmetry breaking scale set by the axion decay constant, f_a, which has been constrained to be greater than 10^{10} GeV from the SN 1987 A (Yao et al. 2006), is at least greater than the reheating temperature of the universe after inflation. This is a rather reasonable assumption, as the reheating temperature is usually taken to be as low as 10^8 GeV in order to avoid overproduction of unwanted relics (Pagels & Primack 1982; Coughlan et al. 1983; Ellis et al. 1986). Such a low reheating temperature is natural also because a coupling between inflaton and matter had to be weak; otherwise, it would terminate inflation prematurely.

There is another constraint. The Hubble parameter during inflation needs to be smaller than f_a, that is, $H_{\rm inf} \lesssim f_a$; otherwise, the Pecci–Quinn symmetry would be restored by quantum fluctuations (Lyth & Stewart 1992).

In this scenario, axions acquired quantum fluctuations during inflation, in the same way that inflaton fields would acquire fluctuations. These fluctuations were then converted to mass density fluctuations when axions acquired mass at the QCD phase transition at ~ 200 MeV. We observe a signature of the axion mass density fluctuations via CDM-photon entropy perturbations imprinted in the CMB temperature and polarization anisotropies.

We find that the tensor-to-scalar ratio, r, the axion density, Ω_a, the CDM density, Ω_c, the phase of the Pecci–Quinn field within our observable universe, θ_a, and α_0 are related as (for an alternative expression that has f_a left instead of θ_a, see Equation (B7))

$$r = \frac{4.7 \times 10^{-12}}{\theta_a^{10/7}} \left(\frac{\Omega_c h^2}{\gamma}\right)^{12/7} \left(\frac{\Omega_c}{\Omega_a}\right)^{2/7} \frac{\alpha_0}{1-\alpha_0}, \quad (47)$$

$$< \frac{(0.99 \times 10^{-13})\alpha_0}{\theta_a^{10/7}\gamma^{12/7}} \left(\frac{\Omega_c}{\Omega_a}\right)^{2/7} \quad (48)$$

where $\gamma \leqslant 1$ is a "dilution factor" representing the amount by which the axion density parameter, $\Omega_a h^2$, would have been diluted due to a potential late-time entropy production by, for example, decay of some (unspecified) heavy particles, between 200 MeV and the epoch of nucleosynthesis, 1 MeV. Here, we have used the limit on the CDM density parameter, $\Omega_c h^2$, from the axion entropy perturbation model that we consider here, $\Omega_c h^2 = 0.1052^{+0.0068}_{-0.0070}$, as well as the observational fact that $\alpha_0 \ll 1$.

With our limit, $\alpha_0 < 0.072$ (95% CL), we find a limit on r within this scenario as

$$r < \frac{6.6 \times 10^{-15}}{\theta_a^{10/7}\gamma^{12/7}} \left(\frac{\Omega_c}{\Omega_a}\right)^{2/7}. \quad (49)$$

Therefore, in order for the axion dark matter scenario that we have considered here to be compatible with $\Omega_c \sim \Omega_a$ and the

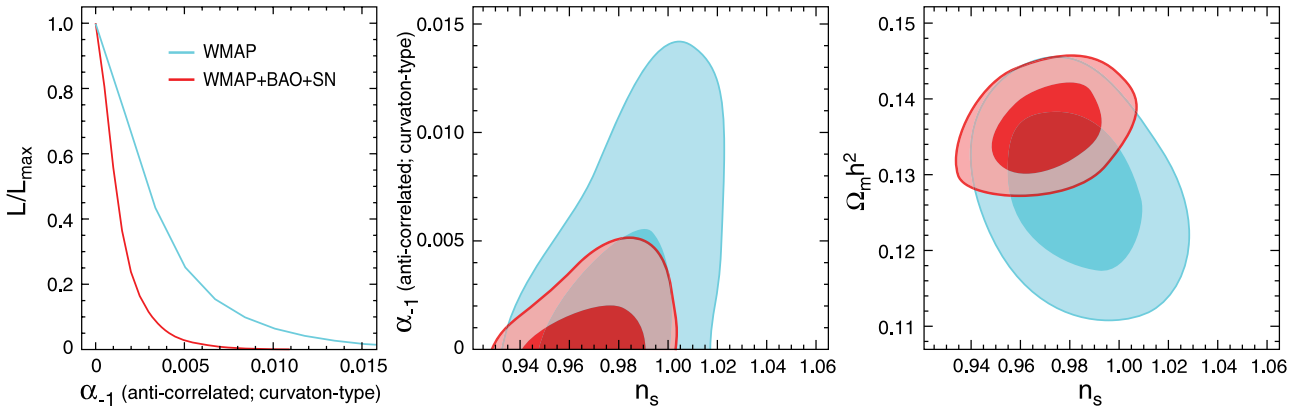

Figure 9. Constraint on the curvaton entropy perturbation fraction, α_{-1} (Section 3.6.4). In all panels, we show the *WMAP*-only results in blue and *WMAP*+BAO+SN in red. (Left) One-dimensional marginalized constraint on α_{-1}, showing *WMAP*-only and *WMAP*+BAO+SN. (Middle) Joint two-dimensional marginalized constraint (68% and 95% CL), showing the correlation between α_{-1} and n_s for *WMAP*-only and *WMAP*+BAO+SN. (Right) Correlation between n_s and $\Omega_m h^2$. The BAO and SN data help to reduce this correlation which, in turn, reduces correlation between α_{-1} and n_s, resulting in a factor of 2.7 better limit on α_{-1}. These properties are similar to those of the axion dark matter presented in Figure 8.

limits on the nonadiabaticity and $\Omega_c h^2$, the energy scale of inflation should be low, and hence the gravitational waves are predicted to be negligible, *unless* the axion density was diluted severely by a late-time entropy production, $\gamma \sim 0.8 \times 10^{-7}$ (for $\theta_a \sim 1$), the axion phase (or the misalignment angle) within our observable universe was close to zero, $\theta_a \sim 3 \times 10^{-9}$ (for $\gamma \sim 1$), or both γ and θ_a were close to zero with lesser degree. All of these possibilities would give $r \sim 0.01$, a value that could be barely detectable in the foreseeable future. One can also reverse Equation (49) to obtain

$$\frac{\Omega_a}{\Omega_c} < \frac{3.0 \times 10^{-39}}{\theta_a^5 \gamma^6} \left(\frac{0.01}{r}\right)^{7/2}. \quad (50)$$

Therefore, the axion density would be negligible for the detectable r, unless θ_a, or γ, or both are tuned to be small.

Whether such an extreme production of entropy is highly unlikely, or such a tiny angle is an undesirable fine-tuning, can be debated. In any case, it is clear that the cosmological observations, such as the CDM density, entropy perturbations, and gravitational waves, can be used to place a rather stringent limit on the axion cosmology based upon the misalignment scenario, one of the most popular scenarios for axions to become a dominant dark matter component in the universe.

3.6.4. Results: Implications for Curvaton

Next, let us consider one of the curvaton models in which $\mathcal{S}$ and $\tilde{\mathcal{R}}$ are totally anticorrelated, that is, $\beta = -1$ (Lyth & Wands 2003; Moroi & Takahashi 2001, 2002; Bartolo & Liddle 2002). One can also write $\mathcal{S}$ as $\mathcal{S} = B\mathcal{R} = -B\tilde{\mathcal{R}}$ where $B > 0$; thus, $B^2 = \alpha_{-1}/(1-\alpha_{-1})$.[38] We take the spectral index of the curvaton entropy perturbation, m, to be the same as that of the adiabatic perturbation, n_s, that is, $n_s = m$.

The left panel of Figure 9 shows that we do not find any evidence for the curvaton entropy perturbations, either. The limits, $\alpha_{-1} < 0.011$ (95% CL) and $\alpha_{-1} < 0.0041$ (95% CL) for the *WMAP*-only analysis and *WMAP*+BAO+SN, respectively, are more than a factor of 10 better than those for the axion perturbations. The *WMAP*-only limit is better than the previous limit by a factor of 4 (Bean et al. 2006). From the *WMAP*+BAO+SN limit, we find the adiabaticity deviation parameter of $\delta_{\rm adi}^{(c,\gamma)} < 0.021$ (Equation (39)); thus, we conclude that the curvaton dark matter and photons should obey the adiabatic relation (Equation (36)) to 2.1% at the 95% CL.

Once again, adding the distance information from the BAO and SN helps to reduce the correlation between n_s and $\Omega_m h^2$ (see the right panel of Figure 9) and reduces the correlation between n_s and α_{-1}. The directions in which these parameters are degenerate are similar to those for the axion case (see Figure 8), as the entropy perturbation with $\beta = -1$ also increases the CMB temperature power spectrum on large angular scales, as we described in Section 3.6.2.

What is the implication for this type of curvaton scenario, in which $\beta = -1$? This scenario would arise when CDM was created from the decay products of the curvaton field. One then finds a prediction (Lyth et al. 2003)

$$\frac{\alpha_{-1}}{1-\alpha_{-1}} \approx 9 \left(\frac{1-\rho_{\rm curvaton}/\rho_{\rm total}}{\rho_{\rm curvaton}/\rho_{\rm total}}\right)^2, \quad (51)$$

where $\rho_{\rm curvaton}$ and $\rho_{\rm total}$ are the curvaton density and total density at the curvaton decay, respectively. Note that there would be no entropy perturbation if curvaton dominated the energy density of the universe completely at the decay. The reason is simple: in such a case, *all* of the curvaton perturbation would become the adiabatic perturbation, so would the CDM perturbation. Our limit, $\alpha_{-1} < 0.0041$ (95% CL), indicates that $\rho_{\rm curvaton}/\rho_{\rm total}$ is close to unity, which simplifies the relation (Equation (51)) to give

$$\frac{\rho_{\rm curvaton}}{\rho_{\rm total}} \approx 1 - \frac{\sqrt{\alpha_{-1}}}{3} = 1 - \delta_{\rm adi}^{(c,\gamma)}. \quad (52)$$

Note that it is the adiabaticity deviation parameter given by Equation (39) that gives the deviation of $\rho_{\rm curvaton}/\rho_{\rm total}$ from unity. From this result, we find

$$1 \geqslant \frac{\rho_{\rm curvaton}}{\rho_{\rm total}} \gtrsim 0.98 \qquad (95\%\ {\rm CL}). \quad (53)$$

As we mentioned in Section 3.5.1, the curvaton scenario is capable of producting the local form of non-Gaussianity, and $f_{\rm NL}^{\rm local}$ is given by (Lyth & Rodriguez 2005, and references

[38] This variable, B, is the same as B used in Gordon & Lewis (2003), including the sign convention.

therein[39])

$$f_{\rm NL}^{\rm local} = \frac{5\rho_{\rm total}}{4\rho_{\rm curvaton}} - \frac{5}{3} - \frac{5\rho_{\rm curvaton}}{6\rho_{\rm total}}, \quad (54)$$

which gives $-1.25 \leqslant f_{\rm NL}^{\rm local}({\rm curvaton}) \lesssim -1.21$, for $\alpha_{-1} < 0.0041$ (95% CL). While we need to add additional contributions from postinflationary, nonlinear gravitational perturbations of order unity to this value in order to compare with what we measure from CMB, the limit from the curvaton entropy perturbation is consistent with the limit from the measured $f_{\rm NL}^{\rm local}$ (see Section 3.5.3).

However, should the future data reveal $f_{\rm NL}^{\rm local} \gg 1$, then either this scenario would be ruled out (Beltrán 2008; Li et al. 2008b) or the curvaton dark matter must have been in thermal equilibrium with photons.

For the other possibilities, including possible baryon entropy perturbations, see Gordon & Lewis (2003).

4. PROBING PARITY VIOLATION OF THE UNIVERSE: TB AND EB CORRELATION

4.1. Motivation

Since the temperature and E-mode polarization are parity-even and the B-mode polarization is parity-odd, the TB and EB correlations should vanish in a universe that conserves parity (Kamionkowski et al. 1997a, 1997b; Seljak & Zaldarriaga 1997; Zaldarriaga & Seljak 1997). For this reason, the TB and EB correlations are usually used to check for systematics, and not widely used as a cosmological probe.

However, parity is violated in the weak interactions (Lee & Yang 1956; Wu et al. 1957). Why cannot parity be violated at cosmological scales?

Polarization of photons offers a powerful way of probing the cosmological parity violation or the "cosmological birefringence" (Lue et al. 1999; Carroll 1998). Let us consider a parity-violating interaction term in the Lagrangian such as the Chern–Simons term, $\mathcal{L}_{\rm CS} = -(1/2)p_\alpha A_\beta \tilde{F}^{\alpha\beta}$, where $F^{\alpha\beta}$ and A_β are the usual electromagnetic tensor and vector potential, respectively, $\tilde{F}^{\alpha\beta} = (1/2)\epsilon^{\alpha\beta\mu\nu}F_{\mu\nu}$ is a dual tensor, and p_α is an arbitrary timelike four-vector.[40] Carroll et al. (1990) have shown that the Chern–Simons term makes two polarization states of photons propagate with different group velocities, *causing the polarization plane to rotate* by an angle $\Delta\alpha$.

What would p_α be? We may take this to be a derivative of a light scalar field, $p_\alpha = 2(\partial_\alpha\phi)/M$, where M is some unspecified energy scale. In this case, the rotation angle is given by $\Delta\alpha = \int \frac{dt}{a}\dot{\phi}/M = (\Delta\phi)/M$ (Carroll et al. 1990; Carroll 1998; Liu et al. 2006; Xia et al. 2008). Such a field might have something to do with dark energy, for example. We are, therefore, looking at a potential parity-violating interaction between the visible section (i.e., photons) and dark sector (i.e., dark energy).

Such an unusual rotation of polarization vectors has been constrained by observations of radio galaxies and quasars (Carroll 1998); one of the best datasets available today at a single redshift is 3C9 at $z = 2.012$, which gives a limit on the rotation angle, $\Delta\alpha = 2^\circ \pm 3^\circ$ (68% CL). There are about ten measurements between $z = 0.425$ and $z = 2.012$, whose average is $\Delta\alpha = -0.^\circ6 \pm 1.^\circ5$ (68% CL).

The rotation of the polarization plane converts the E-mode polarization to the B-mode. As a result, B modes can be produced from E modes even if inflation did not produce much B modes. This is similar to the gravitational lensing effect, which also produces B modes from E modes (Zaldarriaga & Seljak 1998), but there is an important difference: the lensing does not violate parity, but this interaction does. As a result, the lensing does not yield nonzero TB or EB, but this interaction yields both TB and EB.

We shall constrain $\Delta\alpha$ between the reionization epoch, $z \sim 10$, and the present epoch, as well as $\Delta\alpha$ between the decoupling epoch, $z \simeq 1090$, and the present epoch, using the TB and EB spectra that we measure from the *WMAP* 5-year data.

4.2. Analysis

Before we proceed, we should remember that the magnitude of polarization rotation angle, $\Delta\alpha$, depends on the path length over which photons experienced a parity-violating interaction. As pointed out by Liu et al. (2006), this leads to the polarization angle that depends on l. We can divide this l-dependence in two regimes:

1. $l \lesssim 20$: the polarization signal was generated during reionization (Zaldarriaga 1997). We are sensitive only to the polarization rotation between the reionization epoch and present epoch.
2. $l \gtrsim 20$: the polarization signal was generated at the decoupling epoch. We are sensitive to the polarization rotation between the decoupling epoch and present epoch; thus, we have the largest path length in this case.

Below, we shall explore two cases separately. Note that we shall use only the polarization spectra: TE, TB, EE, BB, and EB, and do not use the temperature spectrum, as the temperature spectrum is not affected by the parity-violating interaction.

Moreover, for the analysis at $l \leqslant 23$, we only vary the polarization angle, $\Delta\alpha$, and the optical depth, τ, and fix the other parameters at $\Omega_k = 0$, $\Omega_b h^2 = 0.02265$, $\Omega_c h^2 = 0.1143$, $H_0 = 70.1\,{\rm km\,s^{-1}\,Mpc^{-1}}$, and $n_s = 0.960$. At each value of τ, we readjust the overall normalization of power spectra such that the first peak of the temperature spectrum is held fixed. For the analysis at $l \geqslant 24$, we fix τ at 0.085 and vary only $\Delta\alpha$, as there is no correlation between $\Delta\alpha$ and τ at high multipoles. We ignore EE, BB, and EB at $l \geqslant 24$, as they are much noisier than TE and TB and thus do not add much information.

When the polarization plane is rotated by $\Delta\alpha$, the intrinsic (primordial) TE, EE, and BB spectra are converted into TE, TB, EE, BB, and EB spectra as (Lue et al. 1999; Feng et al. 2005)

$$C_l^{\rm TE,obs} = C_l^{\rm TE}\cos(2\Delta\alpha), \quad (55)$$

$$C_l^{\rm TB,obs} = C_l^{\rm TE}\sin(2\Delta\alpha), \quad (56)$$

$$C_l^{\rm EE,obs} = C_l^{\rm EE}\cos^2(2\Delta\alpha) + C_l^{\rm BB}\sin^2(2\Delta\alpha), \quad (57)$$

$$C_l^{\rm BB,obs} = C_l^{\rm EE}\sin^2(2\Delta\alpha) + C_l^{\rm BB}\cos^2(2\Delta\alpha), \quad (58)$$

$$C_l^{\rm EB,obs} = \tfrac{1}{2}\left(C_l^{\rm EE} - C_l^{\rm BB}\right)\sin(4\Delta\alpha), \quad (59)$$

where C_l's are the primordial power spectra in the absence of parity violation, while $C_l^{\rm obs}$'s are what we would observe in the presence of parity violation. To simplify the problem and

[39] Note that the sign convention of $f_{\rm NL}^{\rm local}$ inLyth & Rodriguez (2005) is such that $f_{\rm NL}^{\rm local}{}_{,WMAP} = -f_{\rm NL}^{\rm local}{}_{,\rm theirs}$.

[40] See Lepora (1998); Klinkhamer (2000); Adam & Klinkhamer (2001) for studies on a spacelike p_α, including its signatures in CMB.

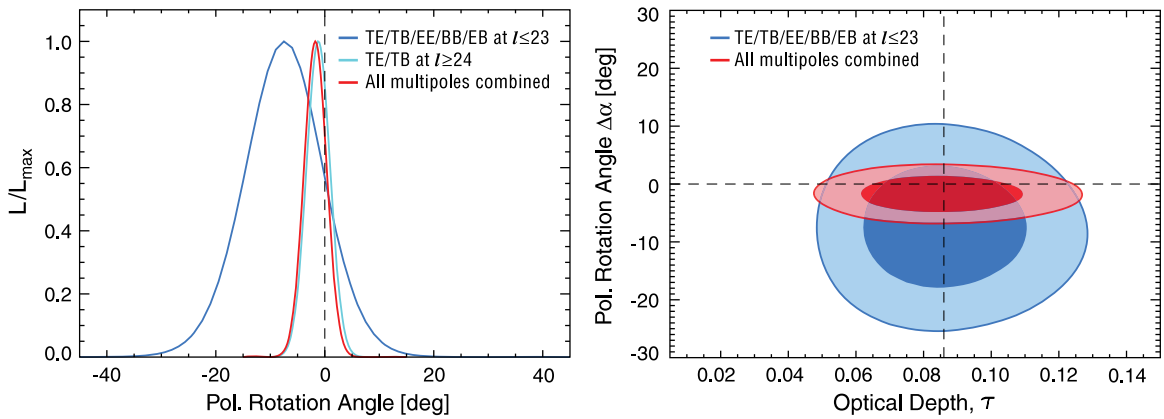

Figure 10. Constraint on the polarization rotation angle, $\Delta\alpha$, due to a parity-violating interaction that rotates the polarization angle of CMB (Section 4.3). We have used the polarization spectra (TE/TB/EE/BB/EB at $l \leqslant 23$ and TE/TB at $l \geqslant 24$) and did not use the TT power spectrum. (Left) One-dimensional marginalized constraint on $\Delta\alpha$ in units of degrees. The dark blue, light blue, and red curves show the limits from the low-l ($2 \leqslant l \leqslant 23$), high-$l$ ($24 \leqslant l \leqslant 450$), and combined ($2 \leqslant l \leqslant 450$) analysis of the polarization data, respectively. (Right) Joint two-dimensional marginalized constraint on τ and $\Delta\alpha$ (68% and 95% CL). The bigger contours are from the low-l analysis, while the smaller ones are from the combined analysis. The vertical dotted line shows the best-fitting optical depth in the absence of parity violation ($\tau = 0.086$), whereas the horizontal dotted line shows $\Delta\alpha = 0$ to guide eyes.

maximize our sensitivity to a potential signal of $\Delta\alpha$, we ignore the primordial BB and use only a reduced set:

$$C_l^{\mathrm{TE,obs}} = C_l^{\mathrm{TE}} \cos(2\Delta\alpha), \tag{60}$$

$$C_l^{\mathrm{TB,obs}} = C_l^{\mathrm{TE}} \sin(2\Delta\alpha), \tag{61}$$

$$C_l^{\mathrm{EE,obs}} = C_l^{\mathrm{EE}} \cos^2(2\Delta\alpha), \tag{62}$$

$$C_l^{\mathrm{BB,obs}} = C_l^{\mathrm{EE}} \sin^2(2\Delta\alpha), \tag{63}$$

$$C_l^{\mathrm{EB,obs}} = \tfrac{1}{2} C_l^{\mathrm{EE}} \sin(4\Delta\alpha). \tag{64}$$

Therefore, TB and EB will be produced via the "leakage" from TE and EE, respectively. Note that E and B are totally correlated in this case: $\left(C_l^{\mathrm{EB,obs}}\right)^2 = C_l^{\mathrm{EE,obs}} C_l^{\mathrm{BB,obs}}$.

Several groups have constrained $\Delta\alpha$ from the *WMAP* 3-year data and from the BOOMERanG data (Feng et al. 2006; Liu et al. 2006; Kostelecky & Mewes 2007; Cabella et al. 2007; Xia et al. 2008). All but Liu et al. (2006) assumed that $\Delta\alpha$ is constant at all multipoles, which is acceptable when they consider the TB and EB data at $l \gtrsim 20$, that is, the BOOMERanG data and high-l *WMAP* data. However, this requires care when one considers the low-l *WMAP* data. Moreover, all of the authors used a Gaussian form of the likelihood function for C_l, which is again acceptable at high multipoles, but it is inaccurate at low multipoles.

For the 5-year data release, we have added capabilities of computing the likelihood of TB and EB spectra at low multipoles, $2 \leqslant l \leqslant 23$, exactly, and that of the TB spectrum at high multipoles, $24 \leqslant l \leqslant 450$, using the MASTER (pseudo-C_l) algorithm. We shall use this code to obtain the limit on $\Delta\alpha$ from the 5-year *WMAP* polarization data. For the low-l polarization, we use the Ka-, Q-, and V-band data, whereas for the high-l polarization, we use the Q- and V-band data.

4.3. Results

Figure 10 shows our limit on $\Delta\alpha$ between (1) the reionization epoch and present epoch from the low-l polarization data (dark blue), (2) between the decoupling epoch and present epoch from the high-l polarization data (light blue), and (3) combined constraints from the low-l and high-l data assuming a constant $\Delta\alpha$ across the entire multipole range (red). We find no evidence for parity-violating interactions: the 95% CL (68% CL) limits are $-22.^\circ2 < \Delta\alpha < 7.^\circ2$ ($\Delta\alpha = -7.^\circ5 \pm 7.^\circ3$) for (1), $-5.^\circ5 < \Delta\alpha < 3.^\circ1$ ($\Delta\alpha = -1.^\circ2 \pm 2.^\circ2$) for (2), and $-5.^\circ9 < \Delta\alpha < 2.^\circ4$ ($\Delta\alpha = -1.^\circ7 \pm 2.^\circ1$) for (3).

The previous 95% CL (68% CL) limits on $\Delta\alpha$ are largely based upon the high-l TB and EB data from the *WMAP* 3-year data and/or BOOMERanG: $-13.^\circ7 < \Delta\alpha < 1.^\circ9$ ($\Delta\alpha = -6.^\circ0 \pm 4.^\circ0$; Feng et al. 2006), $-25^\circ < \Delta\alpha < 2^\circ$ ($\Delta\alpha = -12^\circ \pm 7^\circ$; Kostelecky & Mewes 2007) $-8.^\circ5 < \Delta\alpha < 3.^\circ5$ ($\Delta\alpha = -2.^\circ5 \pm 3.^\circ0$; Cabella et al. 2007), and $-13.^\circ8 < \Delta\alpha < 1.^\circ4$ ($\Delta\alpha = -6.^\circ2 \pm 3.^\circ8$; Xia et al. 2008). Our limits from the *WMAP* 5-year data are tighter than the previous ones by a factor of 1.5–2, and already comparable to those from the polarization data of radio galaxies and quasars (see Section 4.1). Note that the radio galaxies and quasars measure the rotation of polarization between up to $z = 2$ and the present epoch, whereas our limits measure the rotation between the decoupling epoch, $z \simeq 1090$, and the present epoch.

These results show that the TB and EB polarization data can provide interesting limits on parity-violating interaction terms. The future data will be able to place more stringent limits (Xia et al. 2008). In particular, adding the *Ka* and *W*-band data to the high-l polarization should improve our limit significantly.

5. DARK ENERGY

5.1. Motivation

Dark energy is one of the most mysterious observations in physics today. The issue is the following: when the luminosity distances out to Type Ia SNe (Riess et al. 1998; Perlmutter et al. 1999) and the angular diameter distances measured from the BAO (Eisenstein et al. 2005) as well as CMB (Bennett et al. 2003b) are put together in the context of homogeneous and isotropic cosmological models, one cannot fit these distances without having an accelerated expansion of the universe today. A straightforward interpretation of this result is that we need an additional energy component in the universe that has a large negative pressure, which causes the expansion to accelerate.

However, we do not know much about dark energy. A study of review articles written over the past 20 years reveals a growing circle of ignorance (Weinberg 1989; Carroll et al. 1992; Sahni & Starobinsky 2000; Padmanabhan 2003, 2005; Peebles & Ratra 2003; Copeland et al. 2006); physicists first struggled

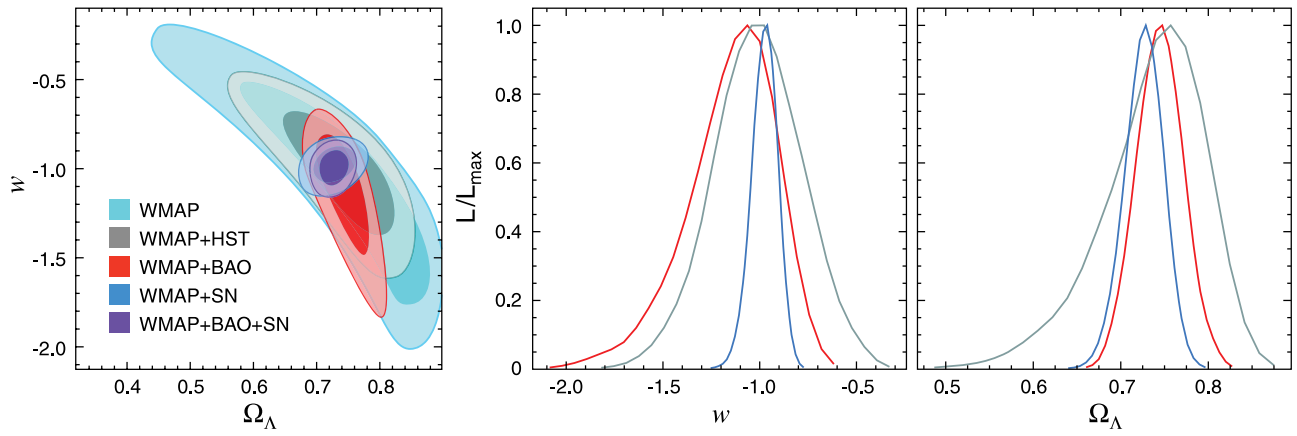

Figure 11. Constraint on the time-independent (constant) dark energy equation of state, w, and the present-day dark energy density, Ω_Λ, assuming a flat universe, $\Omega_k = 0$ (Section 5.2). Note that we have imposed a prior on w, $w > -2.5$. (Left) Joint two-dimensional marginalized distribution of w and Ω_k. The contours show the 68% and 95% CL. The *WMAP*-only constraint (light blue) is compared with *WMAP*+*HST* (gray), *WMAP*+BAO (red), *WMAP*+SN (dark blue), and *WMAP*+BAO+SN (purple). This figure shows how powerful a combination of the *WMAP* data and the current SN data is for constraining w. (Middle) One-dimensional marginalized constraint on w for a flat universe from *WMAP*+*HST* (gray), *WMAP*+BAO (red), and *WMAP*+SN (dark blue). The *WMAP*+BAO+SN result (not shown) is essentially the same as *WMAP*+SN. (Right) One-dimensional marginalized constraints on Ω_Λ for a flat universe from *WMAP*+*HST* (gray), *WMAP*+BAO (red), and *WMAP*+SN (dark blue). The *WMAP*+BAO+SN result (not shown) is essentially the same as *WMAP*+SN. See Figure 12 for the constraints on w for nonflat universes. Note that neither BAO nor SN alone is able to constrain w: they need the *WMAP* data for lifting the degeneracy. Note also that BAO+SN is unable to lift the degeneracy either, as BAO needs the sound horizon size measured by the *WMAP* data.

to understand why the cosmological constant or vacuum energy term was so close to zero and then to understand why it was nonzero. Cosmologists then explored the possibility that dark energy was dynamical, for example, in a form of some light scalar field (Ford 1987; Wetterich 1988; Ratra & Peebles 1988; Peebles & Ratra 1988; Fujii & Nishioka 1990; Chiba et al. 1997; Caldwell et al. 1998; Copeland et al. 1998; Ferreira & Joyce 1998; Zlatev et al. 1999). Recently, there has been significant interest in modifications to general relativity, in the context of explaining the acceleration of the universe (Dvali et al. 2000; Deffayet et al. 2002).

Currently, the properties of dark energy are mainly constrained by the distance information. There are other promising ways of finding dark energy independent of distances: the expansion rate of the universe at higher ($z \gtrsim 0.5$) redshifts, the ISW effect, and a slow-down of the growth of the large-scale structure in the universe due to dark energy. While these tools are powerful in principle, the current data are not accurate enough to distinguish between the effects of dark energy and spatial curvature of the universe, owing to the degeneracy between them (e.g., Nesseris & Perivolaropoulos 2008; Ho et al. 2008; Giannantonio et al. 2008).

Indeed, the properties of dark energy, such as the present-day density and its evolution, for example the equation of state parameter w, are degenerate with the spatial curvature of the universe, Ω_k. In this section, we shall explore both flat and curved universes when we report on our limits on the dark energy properties.

In Sections 5.2 and 5.3, we explore constraints on a time-independent (i.e., constant) equation of state, w, assuming flat ($\Omega_k = 0$) and curved ($\Omega_k \neq 0$) geometries, respectively. In Section 5.4, we introduce a set of "*WMAP* distance priors," and use them to explore a wider range of model space that has a time-dependent equation of state, $w = w(z)$. Throughout Section 5.4, we use the distance information only to constrain the properties of dark energy. We thus assume the standard homogeneous and isotropic Friedmann–Lemaitre–Robertson–Walker–universe, and do not consider modifications of gravity or local inhomogeneity, as the distance information alone cannot discriminate between these models and the accelerated expansion due to dark energy. Finally, in Section 5.5, we introduce a "*WMAP* normalization prior."

5.2. Constant Equation of State: Flat Universe

What are we doing by assuming a flat universe, when we constrain the dark energy equation of state, w? Most inflation models in which the inflationary periods last for much longer than 60 e-folds predict $\Omega_k \sim 10^{-5}$, which is three orders of magnitude below the current constraint (see Section 3.4). In this subsection, we use a "strong inflation prior," imposing a flatness prior, and explore dark energy models in the context of such inflation models. We shall explore curved universes in Section 5.3.

Figure 11 shows the constraints on w and the present-day dark energy density, Ω_Λ. The *WMAP* data alone cannot constrain this parameter space very well, as certain combinations of w and Ω_Λ can produce very similar angular diameter distances out to the decoupling epoch.

The *HST* prior helps a little bit $-0.47 < 1 + w < 0.42$ (95% CL) by constraining Ω_Λ: the *WMAP* data measure $\Omega_m h^2$ and a flatness prior imposes a constraint, $\Omega_\Lambda = 1 - (\Omega_m h^2)/h^2$; thus, an additional constraint on h from the *HST* Key Project helps determine Ω_Λ better.

The current angular diameter distance measurements from the BAO do not quite break the degeneracy between w and Ω_Λ, as they constrain the distances at relatively low redshifts, $z = 0.2$ and 0.35, whereas the transition from matter to dark energy domination, which is sensitive to w, happens at earlier times. Therefore, the future BAO surveys at higher redshifts should be more sensitive to w. The *WMAP*+BAO yields $-0.68 < 1 + w < 0.21$ (95% CL).[41]

Finally, the Type Ia SN data break the degeneracy nicely, as their constraint on this parameter space is nearly orthogonal

[41] The 68% limit is $w = -1.15^{+0.21}_{-0.22}$ (*WMAP*+BAO; $\Omega_k = 0$).

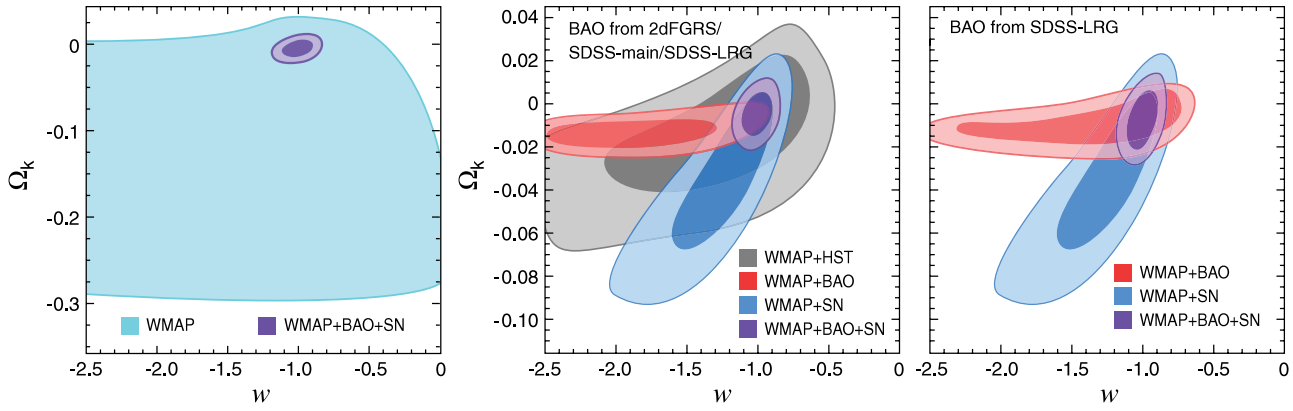

Figure 12. Joint two-dimensional marginalized constraint on the time-independent (constant) dark energy equation of state, w, and the curvature parameter, Ω_k (Section 5.3). Note that we have imposed a prior on w, $w > -2.5$. The contours show the 68% and 95% CL. (Left) The *WMAP*-only constraint (light blue; 95% CL) compared with *WMAP*+BAO+SN (purple; 68% and 95% CL). This figure shows how powerful the extra distance information from BAO and SN is for constraining Ω_k and w simultaneously. (Middle) A blow-up of the left panel, showing *WMAP*+*HST* (gray), *WMAP*+BAO (red), *WMAP*+SN (dark blue), and *WMAP*+BAO+SN (purple). This figure shows that we need both BAO and SN to constrain Ω_k and w simultaneously: *WMAP*+BAO fixes Ω_k and *WMAP*+SN fixes w. (Right) The same as the middle panel, but with the BAO prior re-weighted by a weaker BAO prior from the SDSS LRG sample (Eisenstein et al. 2005). The BAO data used in the other panels combine the SDSS main and LRG, as well as the 2dFGRS data (Percival et al. 2007). The constraints from these are similar, and thus our results are not sensitive to the exact form of the BAO data sets. Note that neither BAO nor SN alone is able to constrain w or Ω_k: they need the *WMAP* data for lifting the degeneracy. Also note that BAO+SN is unable to lift the degeneracy either, as BAO needs the sound horizon size measured by the *WMAP* data.

to what is determined by the CMB data: *WMAP*+SN yields $-0.12 < 1 + w < 0.14$ (95% CL).[42]

With a flatness prior, the constraint on w from SN is so powerful that *WMAP*+SN is similar to *WMAP*+BAO+SN. We conclude that, when the equation of state does not depend on redshifts, dark energy is consistent with vacuum energy, with $-0.12 < 1 + w < 0.13$ (95% CL)[43] (from *WMAP*+BAO+SN), in the context of a flat universe at the level of curvature that is predicted by long-lasting inflation models.

5.3. Constant Equation of State: Curved Universe

In this subsection, we do not assume a flat universe, but do assume a constant equation of state (for a time-dependent equation of state, see Section 5.4.2). As we discussed in Section 3.4, the *WMAP* data alone are unable to place meaningful constraints on the spatial curvature of the universe; however, two or more distance or expansion rate measurements break the degeneracy between Ω_k and Ω_m. As Figure 6 shows, the combination of the *WMAP* measurement of the distance to the decoupling epoch at $z \simeq 1090$, and the distance measurements out to $z = 0.2$ and 0.35 from BAO, strongly constrains the curvature, at the level of 1%–2%.

However, when dark energy is dynamical, we need three distance indicators that cover a wide range of redshift. As the current SN data cover a wider range in redshifts, $0.02 \lesssim z \leqslant 1.7$, than the BAO data, the SN data help to constrain the evolution of dark energy, that is, w.

Figure 12 shows the constraints on w and Ω_k from the *WMAP* 5-year data alone, *WMAP*+*HST*, *WMAP*+BAO, *WMAP*+SN, as well as *WMAP*+BAO+SN. The middle panel is particularly illuminating. The *WMAP*+BAO combination fixes Ω_k, nearly independent of w.[44] The *WMAP*+SN combination yields a degeneracy line that is tilted with respect to the *WMAP*+BAO line. The *WMAP*+BAO and *WMAP*+SN lines intersect at $\Omega_k \sim 0$ and $w \sim -1$, and the combined constraints are $-0.0179 < \Omega_k < 0.0081$ (95% CL) and $-0.14 < 1 + w < 0.12$ (95% CL), respectively.[45] It is remarkable that the limit on Ω_k is as good as that for a vacuum energy model, $-0.0178 < \Omega_k < 0.0066$ (95% CL). This is because the BAO and SN yield constraints on Ω_k and w that are complementary to each other, breaking the degeneracy effectively.

These limits give the lower bounds to the curvature radii of the observable universe as $R_{\rm curv} > 33\,h^{-1}$ Gpc and $R_{\rm curv} > 22\,h^{-1}$ Gpc for negatively and positively curved universes, respectively.

Is the apparent "tension" between the *WMAP*+BAO limit and the *WMAP*+SN limit in Figure 12 the signature of new physics? We have checked this by the BAO distance scale out to $z = 0.35$ from the SDSS LRG sample, obtained by Eisenstein et al. (2005), instead of the $z = 0.2$ and $z = 0.35$ constraints based on the combination of SDSS LRGs with the SDSS main sample and 2dFGRS (Percival et al. 2007). While it is not an independent check, it does provide some measurement of the sensitivity of the constraints to the details of the BAO dataset.

The right panel of Figure 12 shows that the results are not sensitive to the exact form of the BAO datasets.[46] The Eisenstein et al. (2005) BAO prior is a bit weaker than Percival et al.'s, and thus the *WMAP*+BAO contours extend more to $w \gtrsim -1$. The important point is that the direction of degeneracy does not change. Therefore, the combined limits from *WMAP*, SN, and the Eisenstein et al. BAO, $-0.15 < 1 + w < 0.13$ (95% CL), and $-0.0241 < \Omega_k < 0.0094$ (95% CL) are similar to those with Percival et al.'s BAO, $-0.14 < 1 + w < 0.12$ (95% CL), and $-0.0179 < \Omega_k < 0.0081$ (95% CL). As expected, a weaker BAO prior resulted in a weaker limit on Ω_k.

While the above argument suggests that there is no serious tension between *WMAP*+BAO and *WMAP*+SN constraints,

[42] The 68% limit is $w = -0.977^{+0.065}_{-0.064}$ (*WMAP*+SN; $\Omega_k = 0$).

[43] The 68% limit is $w = -0.992^{+0.061}_{-0.062}$ (*WMAP*+BAO+SN; $\Omega_k = 0$).

[44] For the *WMAP*+BAO limit, there is a long degenerate valley with a significant volume at $w < -1$. Models anywhere in this valley are good fits to both datasets. It is dangerous to marginalize over these degenerate parameters as conclusions are very sensitive to the choice and the form of priors.

[45] The 68% limits are $\Omega_k = -0.0049^{+0.0066}_{-0.0064}$ and $w = -1.006^{+0.067}_{-0.068}$ (*WMAP*+BAO+SN).

[46] To obtain the *WMAP*+BAO contours in the right panel of Figure 12, we have re-weighted the *WMAP*+BAO data in the middle panel of Figure 12 by the likelihood ratio of L(Eisenstein's BAO)/L(Percival's BAO). As a result, the contours do not extend to $w \sim 0$; however, the contours would extend more to $w \sim 0$ if we ran a MCMC from the beginning with the Eisenstein et al. BAO.

would it be possible that the tension, if any, could be caused by the *WMAP* data? As the BAO data use the sound horizon size measured by the *WMAP* data, $r_s(z_d)$, some systematic errors causing the miscalculation of $r_s(z_d)$ could lead to a misinterpretation of the BAO data. The current measurement errors in $r_s(z_d)/D_V(z)$ from the BAO data are 2.9% at $z = 0.2$ and 3.0% at $z = 0.35$. However, *WMAP* measures $r_s(z_d)$ with 1.3% accuracy (see Table 3). We are confident that the systematic error in $r_s(z_d)$, if any, is smaller than the statistical error; thus, it is unlikely that *WMAP* causes a misinterpretation of the BAO data.

From these studies, we are able to place rather stringent, simultaneous limits on Ω_k (to a 1%–2% level, depending upon the sign) and w (to a 14% level). The spatial curvature is consistent with zero and the dark energy is consistent with vacuum energy. How does this conclusion change when we allow w to vary?

5.4. *WMAP* Distance Priors for Testing Dark Energy Models

5.4.1. Motivation

Dark energy influences the distance scales as well as the growth of structure. The CMB power spectra are sensitive to both, although sensitivity to the growth of structure is fairly limited, as it influences the CMB power spectrum via the ISW effect at low multipoles ($l \lesssim 10$), whose precise measurement is hampered by a large cosmic variance.

However, CMB is sensitive to the distance to the decoupling epoch via the locations of peaks and troughs of the acoustic oscillations, which can be measured precisely. More specifically, CMB measures two distance ratios: (1) the angular diameter distance to the decoupling epoch divided by the sound horizon size at the decoupling epoch, $D_A(z_*)/r_s(z_*)$, and (2) the angular diameter distance to the decoupling epoch divided by the Hubble horizon size at the decoupling epoch, $D_A(z_*)H(z_*)/c$. This consideration motivates our using these two distance ratios to constrain various dark energy models, in the presence of the spatial curvature, on the basis of distance information (Wang & Mukherjee 2007; Wright 2007).

We shall quantify the first distance ratio, $D_A(z_*)/r_s(z_*)$, by the "acoustic scale," l_A, defined by

$$l_A \equiv (1+z_*)\frac{\pi D_A(z_*)}{r_s(z_*)}, \tag{65}$$

where a factor of $(1+z_*)$ arises because $D_A(z_*)$ is the proper (physical) angular diameter distance (Equation (2)), whereas $r_s(z_*)$ is the comoving sound horizon at z_* (Equation (6)). Here, we shall use the fitting function of z_* proposed by Hu & Sugiyama (1996):

$$z_* = 1048[1+0.00124(\Omega_b h^2)^{-0.738}][1+g_1(\Omega_m h^2)^{g_2}], \tag{66}$$

where

$$g_1 = \frac{0.0783(\Omega_b h^2)^{-0.238}}{1+39.5(\Omega_b h^2)^{0.763}}, \tag{67}$$

$$g_2 = \frac{0.560}{1+21.1(\Omega_b h^2)^{1.81}}. \tag{68}$$

Note that one could also use the peak of the probability of last scattering of photons, that is, the peak of the visibility function, to define the decoupling epoch, which we denote as $z_{\rm dec}$. Both quantities yield similar values. We shall adopt z_* here because it is easier to compute, and, therefore, it allows one to implement the *WMAP* distance priors in a straightforward manner.

The second distance ratio, $D_A(z_*)H(z_*)/c$, is often called the "shift parameter," R, given by (Bond et al. 1997)

$$R(z_*) \equiv \frac{\sqrt{\Omega_m H_0^2}}{c}(1+z_*)D_A(z_*). \tag{69}$$

This quantity is different from $D_A(z_*)H(z_*)/c$ by a factor of $\sqrt{1+z_*}$, and also ignores the contributions from radiation, curvature, or dark energy to $H(z_*)$. Nevertheless, we shall use R to follow the convention in the literature.

We give the 5-year *WMAP* constraints on l_A, R, and z_* that we recommend as the *WMAP* distance priors for constraining dark energy models. However, we note an important caveat. As pointed out by Elgarøy & Multamäki (2007) and Corasaniti & Melchiorri (2008), the derivation of the *WMAP* distance priors requires us to assume the underlying cosmology first, as all of these quantities are *derived parameters* from fitting the CMB power spectra. Therefore, one must be careful about which model one is testing. Here, we give the *WMAP* distance priors, assuming the following model.

1. The standard Friedmann–Lemaitre–Robertson–Walker universe with matter, radiation, dark energy, and spatial curvature.
2. Neutrinos with the effective number of neutrinos equal to 3.04, and the minimal mass ($m_\nu \sim 0.05$ eV).
3. Nearly power-law primordial power spectrum of curvature perturbations, $|dn_s/d\ln k| \ll 0.01$.
4. Negligible primordial gravitational waves relative to the curvature perturbations, $r \ll 0.1$.
5. Negligible entropy fluctuations relative to the curvature perturbations, $\alpha \ll 0.1$.

In Figure 13, we show the constraints on w and Ω_k from the *WMAP* distance priors (combined with BAO and SN). We find a good agreement with the full MCMC results (compare the middle and right panels of Figure 12 with the left and right panels of Figure 13, respectively). The constraints from the *WMAP* distance priors are slightly weaker than the full MCMC, as the distance priors use only a part of the information contained in the *WMAP* data.

Of course, the agreement between Figures 12 and 13 does not guarantee that these priors yield good results for the other, more complex dark energy models with a time-dependent w; however, the previous studies indicate that, under the assumptions given above, these priors can be used to constrain a wide variety of dark energy models (Wang & Mukherjee 2007; Elgarøy & Multamäki 2007; Corasaniti & Melchiorri 2008). Also see Li et al. (2008a) for the latest comparison between the *WMAP* distance priors and the full analysis.

Here is the prescription for using the *WMAP* distance priors.

1. For a given $\Omega_b h^2$ and $\Omega_m h^2$, compute z_* from Equation (66).
2. For a given H_0, $\Omega_m h^2$, $\Omega_r h^2$ (which includes $N_{\rm eff} = 3.04$), Ω_Λ, and $w(z)$, compute the expansion rate, $H(z)$, from Equation (7), as well as the comoving sound horizon size at z_*, $r_s(z_*)$, from Equation (6).
3. For a given Ω_k and $H(z)$ from the previous step, compute the proper angular diameter distance, $D_A(z)$, from Equation (2).
4. Use Equations (65) and (69) to compute $l_A(z_*)$ and $R(z_*)$, respectively.

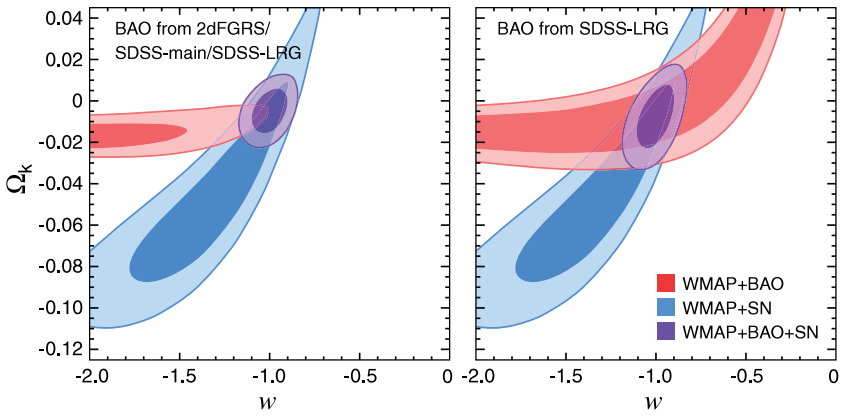

Figure 13. Joint two-dimensional marginalized constraint on the time-independent (constant) dark energy equation of state, w, and the curvature parameter, Ω_k, derived solely from the *WMAP* distance priors (l_A, R, z_*) (see Section 5.4.1), combined with either BAO (red), SN (dark blue), or both (purple). The contours show the $\Delta\chi^2_{\rm total} = 2.30$ (68.3% CL) and $\Delta\chi^2_{\rm total} = 6.17$ (95.4% CL). The left (BAO data from Percival et al. 2007) and right (BAO data from Eisenstein et al. 2005) panels should be compared with the middle and right panels of Figure 12, respectively, which have been derived from the full *WMAP* data combined with the same BAO and SN data. While the *WMAP* distance priors capture most of the information in this parameter space, the constraint is somewhat weaker than that from the full analysis.

5. Form a vector containing $x_i = (l_A, R, z_*)$ in this order.
6. Use Table 10 for the data vector, $d_i = \left(l_A^{WMAP}, R^{WMAP}, z_*^{WMAP}\right)$. We recommend the maximum likelihood (ML) values.
7. Use Table 11 for the inverse covariance matrix, $(C^{-1})_{ij}$.
8. Compute the likelihood, L, as $\chi^2_{WMAP} \equiv -2\ln L = (x_i - d_i)(C^{-1})_{ij}(x_j - d_j)$.
9. Add this to the favorite combination of the cosmological datasets. In this paper we add χ^2_{WMAP} to the BAO and SN data, that is, $\chi^2_{\rm total} = \chi^2_{WMAP} + \chi^2_{BAO} + \chi^2_{SN}$.
10. Marginalize the posterior distribution over $\Omega_b h^2$, $\Omega_m h^2$, and H_0 with uniform priors. Since the *WMAP* distance priors combined with the BAO and SN data provide tight constraints on these parameters, the posterior distribution of these parameters is close to a Gaussian distribution. Therefore, the marginalization is equivalent to minimizing $\chi^2_{\rm total}$ with respect to $\Omega_b h^2$, $\Omega_m h^2$, and H_0 (also see Cash 1976; Wright 2007). We use a downhill simplex method for minimization (amoeba routine in Numerical Recipes; Press et al. 1992). The marginalization over $\Omega_b h^2$, $\Omega_m h^2$, and H_0 leaves us with the the marginalized posterior distribution of the dark energy function, $w(a)$, and the curvature parameter, Ω_k.

Note that this prescription eliminates the need for running the MCMC entirely, and thus the computational cost for evaluating the posterior distribution of $w(a)$ and Ω_k is not demanding. In Section 5.4.2, we shall apply the *WMAP* distance priors to constrain the dark energy equation of state that depends on redshifts, $w = w(z)$.

For those who wish to include an additional prior on $\Omega_b h^2$, we give the inverse covariance matrix for the "extended" *WMAP* distance priors: ($l_A(z_*)$, $R(z_*)$, z_*, $100\Omega_b h^2$), as well as the maximum likelihood value of $100\Omega_b h^2$, in Table 12. We note, however, that it is sufficient to use the reduced set, ($l_A(z_*)$, $R(z_*)$, z_*), as the extended *WMAP* distance priors give very similar constraints on dark energy (see Wang 2008).

5.4.2. Application of the WMAP Distance Priors: Variable Equation of State

In this subsection, we explore a time-dependent equation of state of dark energy, $w(z)$. We use the following parametrized form:

$$w(a) = \frac{a\tilde{w}(a)}{a + a_{\rm trans}} - \frac{a_{\rm trans}}{a + a_{\rm trans}}, \qquad (70)$$

where $\tilde{w}(a) = \tilde{w}_0 + (1-a)\tilde{w}_a$. We give a motivation, derivation, and detailed discussion on this form of $w(a)$ in Appendix C. This form has a number of desirable properties, as follows.

1. $w(a)$ approaches -1 at early times, $a < a_{\rm trans}$, where $a_{\rm trans} = 1/(1 + z_{\rm trans})$ is the "transition epoch" and $z_{\rm trans}$ is the transition redshift. Therefore, the dark energy density tends to a constant value at $a < a_{\rm trans}$.

Table 10
WMAP Distance Priors Obtained from the *WMAP* 5-year Fit to Models with Spatial Curvature and Dark Energy

	5 Year ML[a]	5 Year Mean[b]	Error, σ
$l_A(z_*)$	302.10	302.45	0.86
$R(z_*)$	1.710	1.721	0.019
z_*^{c}	1090.04	1091.13	0.93

Notes.
The correlation coefficients are: $r_{l_A,R} = 0.1109$, $r_{l_A,z_*} = 0.4215$, and $r_{R,z_*} = 0.6928$.
[a] Maximum likelihood values (recommended).
[b] Mean of the likelihood.
[c] Equation (66).

Table 11
Inverse Covariance Matrix for the *WMAP* Distance Priors

	$l_A(z_*)$	$R(z_*)$	z_*
$l_A(z_*)$	1.800	27.968	−1.103
$R(z_*)$		5667.577	−92.263
z_*			2.923

Table 12
Inverse Covariance Matrix for the Extended *WMAP* Distance Priors

	$l_A(z_*)$	$R(z_*)$	z_*	$100\Omega_b h^2$
$l_A(z_*)$	31.001	−5015.642	183.903	2337.977
$R(z_*)$		876807.166	−32046.750	−403818.837
z_*			1175.054	14812.579
$100\Omega_b h^2$				187191.186

Note. The maximum likelihood value of $\Omega_b h^2$ is $100\Omega_b h^2 = 2.2765$.

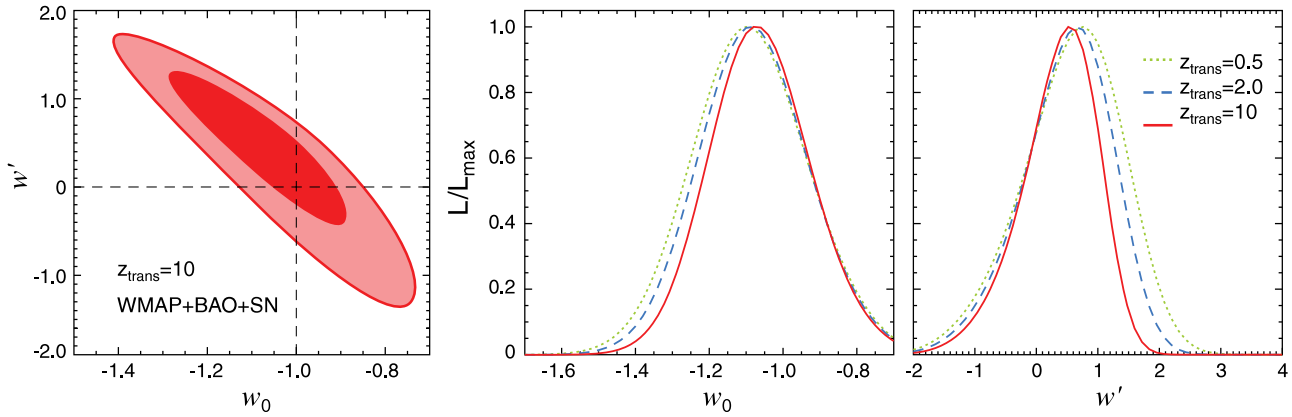

Figure 14. Constraint on models of time-dependent dark energy equation of state, $w(z)$ (Equation (70)), derived from the *WMAP* distance priors (l_A, R, and z_*) combined with the BAO and SN distance data (Section 5.4.2). There are three parameters: w_0 is the value of w at the present epoch, $w_0 \equiv w(z = 0)$, w' is the first derivative of w with respect to z at $z = 0$, $w' \equiv dw/dz|_{z=0}$, and $z_{\rm trans}$ is the transition redshift above which $w(z)$ approaches -1. Here, we assume flatness of the universe, $\Omega_k = 0$. (Left) Joint two-dimensional marginalized distribution of w_0 and w' for $z_{\rm trans} = 10$. The constraints are similar for the other values of $z_{\rm trans}$. The contours show the $\Delta\chi^2_{\rm total} = 2.30$ (68.3% CL) and $\Delta\chi^2_{\rm total} = 6.17$ (95.4% CL). (Middle) One-dimensional marginalized distribution of w_0 for $z_{\rm trans} = 0.5$ (dotted), 2 (dashed), and 10 (solid). (Right) One-dimensional marginalized distribution of w' for $z_{\rm trans} = 0.5$ (dotted), 2 (dashed), and 10 (solid). The constraints are similar for all $z_{\rm trans}$. We do not find evidence for the evolution of dark energy. Note that neither BAO nor SN alone is able to constrain w_0 or w': they need the *WMAP* data for lifting the degeneracy. Also note that BAO+SN is unable to lift the degeneracy either, as BAO needs the sound horizon size measured by the *WMAP* data.

2. The dark energy density remains totally subdominant relative to the matter density at the decoupling epoch.
3. We recover the widely-used linear form, $w(a) = w_0 + (1 - a)w_a$ (Chevallier & Polarski 2001; Linder 2003), at late times, $a > a_{\rm trans}$.
4. The early-time behavior is consistent with some of scalar field models classified as the "thawing models" (Caldwell & Linder 2005) in which a scalar field was moving very slowly at early times and then began to move faster at recent times.
5. Since the late-time form of $w(a)$ allows $w(a)$ to go below -1, our form is more general than models based upon a single scalar field.
6. The form is simple enough to give a closed, analytical form of the effective equation of state, $w_{\rm eff}(a) = (\ln a)^{-1} \int_0^{\ln a} d\ln a' w(a')$ (Equation C6), which determines the evolution of the dark energy density, $\rho_{\rm de}(a) = \rho_{\rm de}(0) a^{-3[1+w_{\rm eff}(a)]}$; thus, it allows one to easily compute the evolution of the expansion rate and cosmological distances.

While this form contains three free parameters, $\tilde{w}_0$, $\tilde{w}_a$, and $z_{\rm trans}$, we shall give constraints on the present-day value of w, $w_0 \equiv w(a = 1)$, and the first derivative of w at present, $w' \equiv dw/dz|_{z=0}$, instead of $\tilde{w}_0$ and $\tilde{w}_a$, as they can be compared to the previous results in the literature more directly. We find that the results are not sensitive to the exact values of $z_{\rm trans}$.

In Figure 14, we present the constraint on w_0 and w' that we have derived from the *WMAP* distance priors (l_A, R, z_*), combined with the BAO and SN data. Note that we have assumed a flat universe in this analysis, although it is straightforward to include the spatial curvature. Wang & Mukherjee (2007) and Wright (2007) showed that the two-dimensional distribution extends more towards southeast, that is, $w > -1$ and $w' < 0$, when the spatial curvature is allowed.

The 95% limit on w_0 for $z_{\rm trans} = 10$ is $-0.33 < 1 + w_0 < 0.21$.[47] Our results are consistent with the previous work using the *WMAP* 3-year data (see Zhao et al. 2007; Wang & Mukherjee 2007; Wright 2007; Lazkoz et al. 2008, for recent work and references therein). The *WMAP* 5-year data help tighten the upper limit on w' and the lower limit on w_0, whereas the lower limit on w' and the upper limit on w_0 come mainly from the Type Ia SN data. As a result, the lower limit on w' and the upper limit on w_0 are sensitive to whether we include the systematic errors in the SN data. For this investigation, see Appendix D.

Alternatively, one may take the linear form, $w(a) = w_0 + (1 - a)w_a$, literally and extend it to an arbitrarily high redshift. This can result in an undesirable situation in which the dark energy is as important as the radiation density at the epoch of the BBN; however, one can severely constrain such a scenario by using the limit on the expansion rate from BBN (Steigman 2007). We follow Wright (2007) to adopt a Gaussian prior on

$$\sqrt{1 + \frac{\Omega_\Lambda (1 + z_{\rm BBN})^{3[1+w_{\rm eff}(z_{\rm BBN})]}}{\Omega_m (1 + z_{\rm BBN})^3 + \Omega_r (1 + z_{\rm BBN})^4 + \Omega_k (1 + z_{\rm BBN})^2}} = 0.942 \pm 0.030, \quad (71)$$

where we have kept Ω_m and Ω_k for definiteness, but they are entirely negligible compared to the radiation density at the redshift of BBN, $z_{\rm BBN} = 10^9$. Figure 15 shows the constraint on w_0 and w' for the linear evolution model derived from the *WMAP* distance priors, the BAO and SN data, and the BBN prior. The 95% limit on w_0 is $-0.29 < 1 + w_0 < 0.21$,[48] which is similar to what we have obtained above.

5.5. *WMAP* Normalization Prior

So far, we have been mainly using the distance information to constrain the properties of dark energy; however, this is not the only information that one can use to constrain the properties of dark energy. The amplitude of fluctuations is a powerful tool for distinguishing between dark energy and modifications to gravity (Ishak et al. 2006; Koyama & Maartens 2006; Amarzguioui et al. 2006; Doré et al. 2007; Linder & Cahn 2007; Upadhye 2007; Zhang et al. 2007; Yamamoto et al. 2007; Chiba & Takahashi 2007; Bean et al. 2007b; Hu & Sawicki 2007; Song et al. 2007; Daniel et al. 2008; Jain & Zhang 2008; Bertschinger & Zukin

[47] The 68% intervals are $w_0 = -1.06 \pm 0.14$ and $w' = 0.36 \pm 0.62$ (*WMAP*+BAO+SN; $\Omega_k = 0$).

[48] The 68% intervals are $w_0 = -1.04 \pm 0.13$ and $w' = 0.24 \pm 0.55$ (*WMAP*+BAO+SN+BBN; $\Omega_k = 0$).

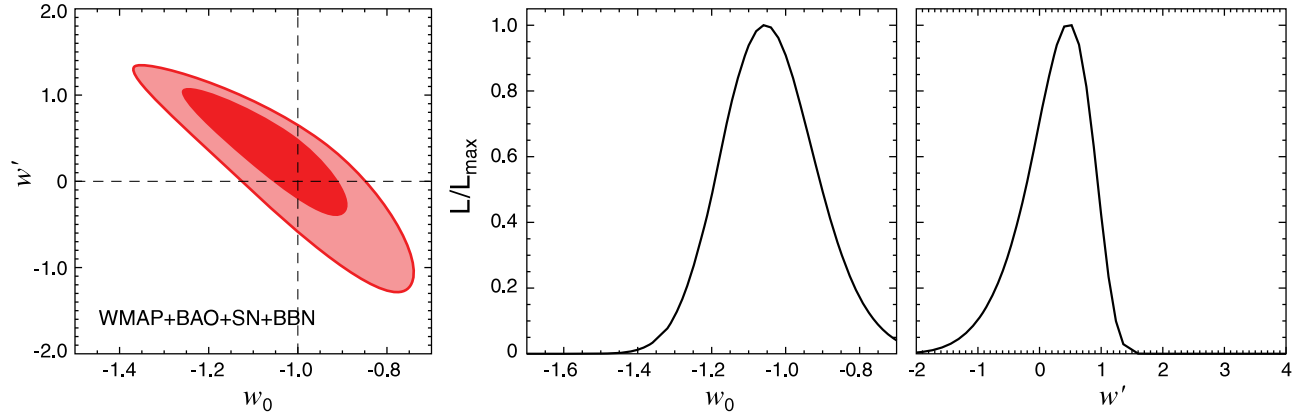

Figure 15. Constraint on the linear evolution model of dark energy equation of state, $w(z) = w_0 + w'z/(1+z)$, derived from the *WMAP* distance priors (l_A, R, and z_*) combined with the BAO and SN distance data as well as the BBN prior (Equation (71)). Here, we assume flatness of the universe, $\Omega_k = 0$. (Left) Joint two-dimensional marginalized distribution of w_0 and w'. The contours show the $\Delta\chi^2_{\rm total} = 2.30$ (68.3% CL) and $\Delta\chi^2_{\rm total} = 6.17$ (95.4% CL). (Middle) One-dimensional marginalized distribution of w_0. (Right) One-dimensional marginalized distribution of w'. We do not find evidence for the evolution of dark energy. Note that Linder (2003) defines w' as the derivative of w at $z = 1$, whereas we define it as the derivative at $z = 0$. They are related by $w'_{\rm linder} = 0.5w'_{WMAP}$.

2008; Amin et al. 2008; Hu 2008), as well as for determining the mass of neutrinos (Hu et al. 1998; Lesgourgues & Pastor 2006).

The microwave background observations measure the amplitude of fluctuations at the decoupling epoch. By combining this measurement with the amplitude measured from various low redshift tracers, one can learn more about the dark energy properties and the mass of neutrinos.

The overall amplitude of CMB anisotropy is set by the amplitude of primordial curvature perturbations, $\mathcal{R}$. For example, on very large angular scales where the Sachs–Wolfe limit can be used, the temperature anisotropy is given by $\Delta T/T = -\mathcal{R}/5$ or, in terms of the curvature perturbation during the matter era, Φ, it is given by $\Delta T/T = -\Phi/3$. On small angular scales where the acoustic physics must be taken into account, we have the acoustic oscillation whose amplitude is also given by $\mathcal{R}$.

This motivates our reporting the "*WMAP* normalization," a measurement of the overall normalization of the curvature perturbations expressed in terms of $\Delta^2_{\mathcal{R}}(k_{WMAP})$, where $\Delta^2_{\mathcal{R}}(k) \equiv k^3 P_{\mathcal{R}}(k)/(2\pi^2)$ is a contribution to the total variance of $\mathcal{R}$, $\langle\mathcal{R}^2\rangle$, per logarithmic interval of k (also see Equation (15) and descriptions below it).

Here, k_{WMAP} is different from $k_0 = 0.002\,{\rm Mpc}^{-1}$ that we used to define n_s, $dn_s/d\ln k$, r, and $\Delta^2_{\mathcal{R}}(k_0)$ reported in Tables 1 and 4. The goal in this subsection is to give the normalization that is *as model independent as possible*.

At $k_0 = 0.002\,{\rm Mpc}^{-1}$, for example, we find $10^9\Delta^2_{\mathcal{R}}(k_0) = 2.48$, 2.41, and 2.46 for a flat ΛCDM model, a curved ΛCDM model, and a flat ΛCDM model with massive neutrinos. The scatter between these values comes solely from the fact that $k_0 = 0.002\,{\rm Mpc}^{-1}$ is not a right place to define the normalization. In other words, this is not the pivot scale of the *WMAP* data.

We find that $k_{WMAP} = 0.02\,{\rm Mpc}^{-1}$, that is, a factor of 10 larger than k_0, gives similar values of $\Delta^2_{\mathcal{R}}(k_{WMAP})$ for a wide range of models, as summarized in Table 13. From these results, we give the *WMAP* normalization prior:

$$\Delta^2_{\mathcal{R}}(k_{WMAP}) = (2.21 \pm 0.09) \times 10^{-9}, \quad (72)$$

which is valid for models with $\Omega_k \neq 0$, $w \neq -1$, or $m_\nu > 0$. However, we find that these normalizations cannot be used for the models that have the tensor modes, $r > 0$, or the running index, $dn_s/d\ln k \neq 0$. We failed to find a universal normalization for these models. Nevertheless, our

Table 13
Amplitude of Curvature Perturbations, $\mathcal{R}$, Measured by *WMAP* at $k_{WMAP} = 0.02\,{\rm Mpc}^{-1}$

Model	$10^9 \times \Delta^2_{\mathcal{R}}(k_{WMAP})$
$\Omega_k = 0$ and $w = -1$	2.211 ± 0.083
$\Omega_k \neq 0$ and $w = -1$	2.212 ± 0.084
$\Omega_k = 0$ and $w \neq -1$	2.208 ± 0.087
$\Omega_k \neq 0$ and $w \neq -1$	2.210 ± 0.084
$\Omega_k = 0$, $w = -1$ and $m_\nu > 0$	2.212 ± 0.083
$\Omega_k = 0$, $w \neq -1$ and $m_\nu > 0$	2.218 ± 0.085
WMAP Normalization Prior	2.21 ± 0.09

WMAP normalization, given by Equation (72), is still valid for a wide range of cosmological models.

How can one use the *WMAP* normalization? In order to predict the linear matter density power spectrum, $P_{\rm lin}(k)$, one needs to relate the primordial curvature perturbations, $\mathcal{R}_{\mathbf{k}}$, to the linear matter density fluctuations at arbitrary redshifts, $\delta_{m,\mathbf{k}}(z)$. From Einstein's equations, we find (see, e.g., Appendix C of Takada et al. 2006)

$$\delta_{m,\mathbf{k}}(z) = \frac{2k^3}{5H_0^2\Omega_m}\mathcal{R}_{\mathbf{k}}T(k)D(k,z), \quad (73)$$

where $D(k,z)$ and $T(k)$ are the linear growth rate and the matter transfer function normalized such that $T(k) \to 1$ as $k \to 0$ and $(1+z)D(k,z) \to 1$ as $k \to 0$ during the matter era (e.g., $z = 30$, where the radiation density is less than 1% of the matter density), respectively. Note that $D(k, z)$ does not depend on k when neutrinos are massless; however, it depends on k when they are massive (e.g., Hu & Eisenstein 1998). The linear matter density power spectrum is given by

$$\frac{k^3 P_{\rm lin}(k,z)}{2\pi^2} = (2.21 \pm 0.09) \times 10^{-9}\left(\frac{2k^2}{5H_0^2\Omega_m}\right)^2 \times D^2(k,z)T^2(k)\left(\frac{k}{k_{WMAP}}\right)^{n_s-1}. \quad (74)$$

One application of the *WMAP* normalization is the computation of the present-day normalization of matter fluctuations,

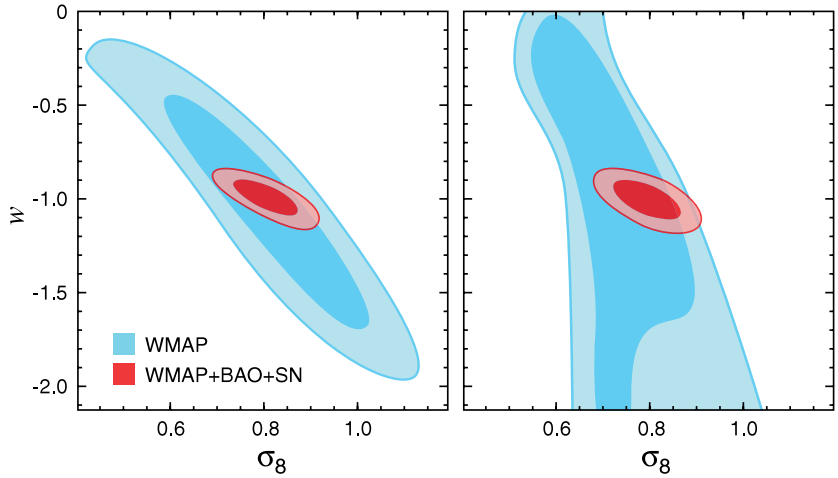

Figure 16. Predictions for the present-day amplitude of matter fluctuations, σ_8, as a function of the (constant) dark energy equation of state parameter, w, derived from the full *WMAP* data (blue) and from *WMAP*+BAO+SN (red). The contours show the 68% and 95% CL. (Left) Flat universe, $\Omega_k = 0$. (Right) Curved universe, $\Omega_k \neq 0$.

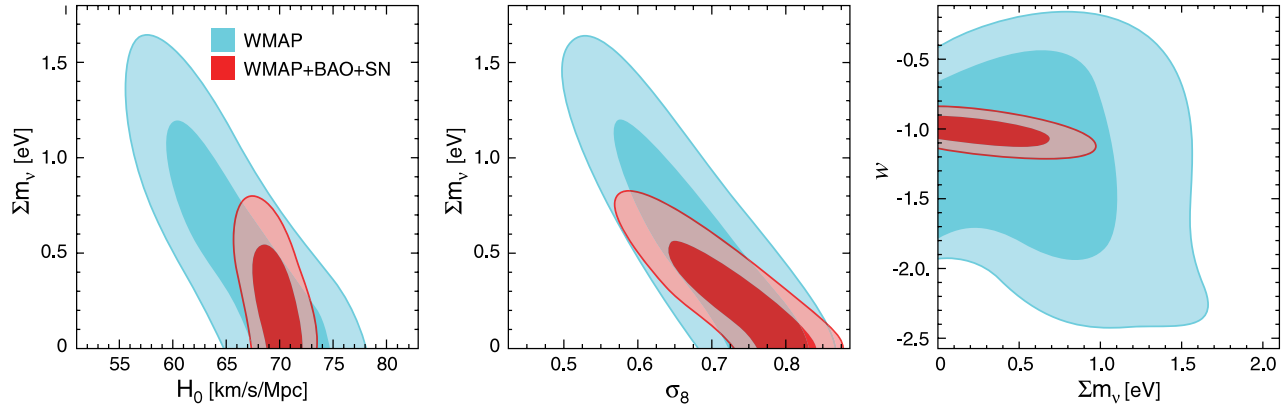

Figure 17. Constraint on the total mass of neutrinos, $\sum m_\nu$ (Section 6.1.3). In all panels, we show the *WMAP*-only results in blue and *WMAP*+BAO+SN in red. (Left) Joint two-dimensional marginalized distribution of H_0 and $\sum m_\nu$ (68% and 95% CL). The additional distance information from BAO helps reduce the correlation between H_0 and $\sum m_\nu$. (Middle) The *WMAP* data, combined with the distances from BAO and SN, predict the present-day amplitude of matter fluctuations, σ_8, as a function of $\sum m_\nu$. An independent determination of σ_8 will help determine $\sum m_\nu$ tremendously. (Right) Joint two-dimensional marginalized distribution of w and $\sum m_\nu$. No significant correlation is observed. Note that we have a prior on w, $w > -2.5$, and thus the *WMAP*-only lower limit on w in this panel cannot be trusted.

which is commonly expressed in terms of σ_8, given by

$$\sigma_8^2 = (2.21 \pm 0.09) \times 10^{-9} \left(\frac{2}{5\Omega_m}\right)^2 \times \int \frac{dk}{k} D^2(k, z=0) T^2(k) \frac{k^4}{H_0^4} \left(\frac{k}{k_{WMAP}}\right)^{n_s - 1} \times \left[\frac{3\sin(kR)}{(kR)^3} - \frac{3\cos(kR)}{(kR)^2}\right]^2, \quad (75)$$

where $R = 8\,h^{-1}$ Mpc. Both the dark energy properties (or modified gravity) and the mass of neutrinos change the value of $D(k, z = 0)$. The transfer function, $T(k)$, is much less affected, as long as neutrinos are still relativistic at the decoupling epoch, and the dark energy or modified gravity effect is unimportant at the decoupling epoch.

Ignoring the mass of neutrinos and modifications to gravity, one can obtain the growth rate by solving the following differential equation (Wang & Steinhardt 1998; Linder & Jenkins 2003):

$$\frac{d^2 g}{d\ln a^2} + \left[\frac{5}{2} + \frac{1}{2}\left(\Omega_k(a) - 3w_{\rm eff}(a)\Omega_{de}(a)\right)\right]\frac{dg}{d\ln a} + \left[2\Omega_k(a) + \frac{3}{2}(1 - w_{\rm eff}(a))\Omega_{de}(a)\right] g(a) = 0, \quad (76)$$

where

$$g(a) \equiv \frac{D(a)}{a} = (1+z)D(z), \quad (77)$$

$$\Omega_k(a) \equiv \frac{\Omega_k H_0^2}{a^2 H^2(a)}, \quad (78)$$

$$\Omega_{de}(a) \equiv \frac{\Omega_\Lambda H_0^2}{a^{3[1+w_{\rm eff}(a)]} H^2(a)}, \quad (79)$$

$$w_{\rm eff}(a) \equiv \frac{1}{\ln a}\int_0^{\ln a} d\ln a' w(a'). \quad (80)$$

During the matter era, $g(a)$ does not depend on a; thus, the natural choice for the initial conditions are $g(a_{\rm initial}) = 1$ and $dg/d\ln a|_{a=a_{\rm initial}} = 0$, where $a_{\rm initial}$ must be taken during the matter era, for example, $a_{\rm initial} = 1/31$ (i.e., $z = 30$).

In Figure 16, we show the predicted values of σ_8 as a function of w in a flat universe (left panel) and curved universes (right panel; see the middle panel of Figure 17 for σ_8 as a function of the mass of neutrinos). Here, we have used the full information in the *WMAP* data. The normalization information alone is unable

to give meaningful predictions for σ_8, which depends not only on $\Delta^2_{\mathcal{R}}(k_{WMAP})$, but also on the other cosmological parameters via $T(k)$ and $D(k, z = 0)$, especially w and $\Omega_m h^2$. While the predictions from the *WMAP* data alone are still weak, adding the extra distance information from the BAO and SN data helps improve the predictions. We find $\sigma_8 = 0.807^{+0.045}_{-0.044}$ for a flat universe and $\sigma_8 = 0.795 \pm 0.046$ for curved universes.

By combining these results with σ_8 measured from various low redshift tracers, one can reduce the remaining correlation between w and σ_8 to obtain a better limit on w. The precision of the current data from weak lensing surveys is comparable to these predictions, for example, $\sigma_8(\Omega_m/0.25)^{0.64} = 0.785 \pm 0.043$ (Canada-France-Hawaii Telescope Legacy Survey (CFHTLS); Fu et al. 2008). The weak lensing surveys will soon become powerful enough to yield smaller uncertainties in σ_8 than predicted from *WMAP*+BAO+SN.

6. NEUTRINOS

In this section, we shall use the *WMAP* data, combined with the distance information from BAO and SN observations, to place limits on the total mass of massive neutrino species (Section 6.1), as well as on the effective number of neutrino-like species that were still relativistic at the decoupling epoch (Section 6.2)

6.1. Neutrino Mass

6.1.1. Motivation

The existence of nonzero neutrino masses has been firmly established by the experiments detecting atmospheric neutrinos (Hirata et al. 1992; Fukuda et al. 1994, 1998; Allison et al. 1999; Ambrosio et al. 2001), solar neutrinos (Davis et al. 1968; Cleveland et al. 1998; Hampel et al. 1999; Abdurashitov et al. 1999; Fukuda et al. 2001b, 2001a; Ahmad et al. 2002; Ahmed et al. 2004), reactor neutrinos (Eguchi et al. 2003; Araki et al. 2005), and accelerator beam neutrinos (Ahn et al. 2003; Michael et al. 2006). These experiments have placed stringent limits on the squared mass *differences* between the neutrino mass eigenstates, $\Delta m^2_{21} \simeq 8 \times 10^{-5}\,\mathrm{eV}^2$, from the solar and reactor experiments, and $\Delta m^2_{32} \simeq 3 \times 10^{-3}\,\mathrm{eV}^2$, from the atmospheric and accelerator beam experiments.

One needs different experiments to measure the *absolute* masses. The next-generation tritium β-decay experiment, KATRIN,[49] is expected to reach the electron neutrino mass of as small as ~ 0.2 eV. Cosmology has also been providing useful limits on the mass of neutrinos (see Dolgov 2002; Elgarøy & Lahav 2005; Tegmark 2005; Lesgourgues & Pastor 2006; Fukugita 2006; Hannestad 2006b, for reviews). Since the determination of the neutrino mass is of fundamental importance in physics, there is enough motivation to pursue cosmological constraints on the neutrino mass.

How well can CMB constrain the mass of neutrinos? We do not expect massive neutrinos to affect the CMB power spectra very much (except through the gravitational lensing effect), if they were still relativistic at the decoupling epoch, $z \simeq 1090$. This means that, for massive neutrinos to affect the CMB power spectra, *at least* one of the neutrino masses must be greater than the mean energy of relativistic neutrinos per particle at $z \simeq 1090$ when the photon temperature of the universe is $T_\gamma \simeq 3000\,\mathrm{K} \simeq 0.26$ eV. Since the mean energy of relativistic neutrinos is given by $\langle E \rangle = (7\pi^4 T_\nu)/(180\zeta(3)) \simeq 3.15 T_\nu = 3.15(4/11)^{1/3} T_\gamma$, we need *at least* one neutrino species whose mass satisfies $m_\nu > 3.15(4/11)^{1/3} T_\gamma \simeq 0.58$ eV; thus, it would not be possible to constrain the neutrino mass using the CMB data alone, if the mass of the heaviest neutrino species is below this value.

If the neutrino mass eigenstates are degenerate with the effective number of species equal to 3.04, this argument suggests that $\sum m_\nu \sim 1.8$ eV would be the limit to which the CMB data are sensitive. Ichikawa et al. (2005) argued that $\sum m_\nu \sim 1.5$ eV would be the limit for the CMB data alone, which is fairly close to the value given above.

In order to go beyond ~ 1.5 eV, therefore, one needs to combine the CMB data with the other cosmological probes. We shall combine the *WMAP* data with the distance information from BAO and SN to place a limit on the neutrino mass. We shall not use the galaxy power spectrum in this paper, and, therefore, our limit on the neutrino mass is free from the uncertainty in the galaxy bias. We discuss this in more detail in Section 6.1.2.

6.1.2. Analysis

We assume that, for definiteness, the neutrino mass eigenstates are *degenerate*, which means that all of the three neutrino species have equal masses.[50] We measure the neutrino mass density parameter, $\Omega_\nu h^2$, and convert it to the total mass, $\sum m_\nu$, via

$$\sum m_\nu \equiv N_\nu m_\nu = 94\,\mathrm{eV}(\Omega_\nu h^2), \tag{81}$$

where N_ν is the number of massive neutrino species. We take it to be 3.04. Note that in this case, the mass density parameter is the sum of baryons, CDM, and neutrinos: $\Omega_m = \Omega_b + \Omega_c + \Omega_\nu$.

Since the release of the 1 year (Spergel et al. 2003) and 3 year (Spergel et al. 2007) results on the cosmological analysis of the *WMAP* data, there have been a number of studies with regard to the limits on the mass of neutrinos (Hannestad 2003; Elgarøy & Lahav 2003; Allen et al. 2003; Tegmark et al. 2004a; Barger et al. 2004; Hannestad & Raffelt 2004; Crotty et al. 2004; Seljak et al. 2005a, 2005b; Ichikawa et al. 2005; Hannestad 2005; Lattanzi et al. 2005; Hannestad & Raffelt 2006; Goobar et al. 2006; Feng et al. 2006; Lesgourgues et al. 2007). These analyses reached different limits depending upon (1) the choice of datasets and (2) the parameters in the cosmological model.

The strongest limits quoted on neutrino masses come from combining CMB measurements with measurements of the amplitude of density fluctuations in the recent universe. Clustering of galaxies and Lyα forest observations have been used to obtain some of the strongest limits on neutrino masses (Seljak et al. 2005b, 2006; Viel et al. 2006). As the neutrino mass increases, the amplitude of mass fluctuations on small scales decreases (Bond et al. 1980; Bond & Szalay 1983; Ma 1996; also see the middle panel of Figure 17), which can be used to weigh neutrinos in the universe (Hu et al. 1998; Lesgourgues & Pastor 2006).

These analyses are sensitive to correctly calculating the relationship between the level of observed fluctuations in galaxies (or gas) and the mass fluctuation with the strongest limits coming from the smallest scales in the analyses. With the new *WMAP* data, these limits are potentially even stronger. There are, however, several potential concerns with this limit:

[49] http://www-ik.fzk.de/~katrin.

[50] While the current cosmological data are not yet sensitive to the mass of *individual* neutrino species, that is, the mass hierarchy, this situation may change in the future, with high-z galaxy redshift surveys or weak lensing surveys (Takada et al. 2006; Slosar 2006; Hannestad & Wong 2007; Kitching et al. 2008; Abdalla & Rawlings 2007).

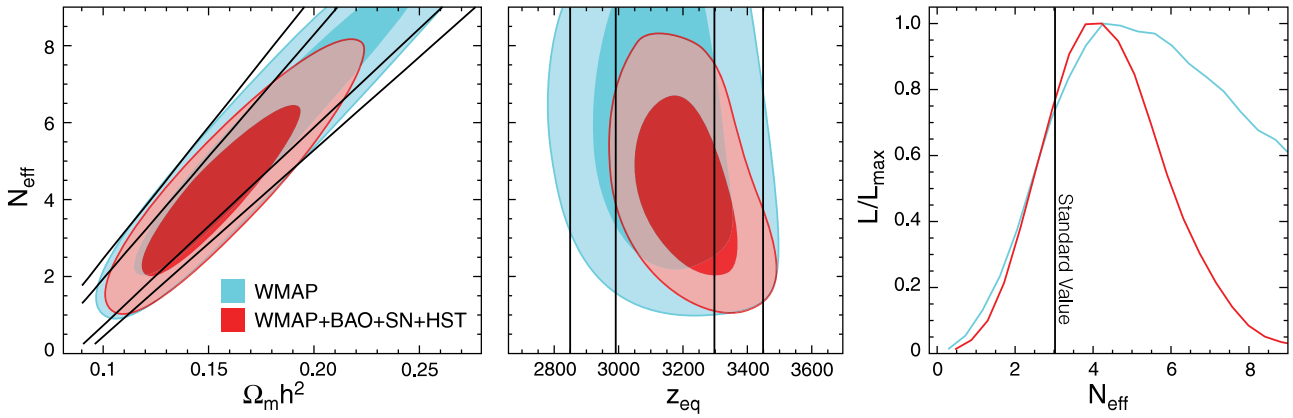

Figure 18. Constraint on the effective number of neutrino species, $N_{\rm eff}$ (Section 6.2.3). Note that we have imposed a prior on $N_{\rm eff}$, $0 < N_{\rm eff} < 10$. In all panels, we show the *WMAP*-only results in blue and *WMAP*+BAO+SN in red. (Left) Joint two-dimensional marginalized distribution (68% and 95% CL), showing a strong degeneracy between $\Omega_m h^2$ and $N_{\rm eff}$. This degeneracy line is given by the equality redshift, $1 + z_{\rm eq} = \Omega_m/\Omega_r = (4.050 \times 10^4)\Omega_m h^2/(1 + 0.2271 N_{\rm eff})$. The thick solid lines show the 68% and 95% limits calculated from the *WMAP*-only limit on $z_{\rm eq}$: $z_{\rm eq} = 3141^{+154}_{-157}$ (68% CL). The 95% CL contours do not follow the lines below $N_{\rm eff} \sim 1.5$ but close there, which shows a strong evidence for the cosmic neutrino background from its effects on the CMB power spectrum via the neutrino anisotropic stress. The BAO and SN provide an independent constraint on $\Omega_m h^2$, which helps reduce the degeneracy between $N_{\rm eff}$ and $\Omega_m h^2$. (Middle) When we transform the horizontal axis of the left panel to $z_{\rm eq}$, we observe no degeneracy. The vertical solid lines show the one-dimensional marginalized 68% and 95% distributions calculated from the *WMAP*-only limit on $z_{\rm eq}$: $z_{\rm eq} = 3141^{+154}_{-157}$ (68% CL). Therefore, the left panel is simply a rotation of this panel using a relation among $z_{\rm eq}$, $\Omega_m h^2$, and $N_{\rm eff}$. (Right) One-dimensional marginalized distribution of $N_{\rm eff}$ from *WMAP*-only and *WMAP*+BAO+SN+*HST*. Note that a gradual decline of the likelihood toward $N_{\rm eff} \gtrsim 6$ for the *WMAP*-only constraint should not be trusted, as it is affected by the hard prior, $N_{\rm eff} < 10$. The *WMAP*+BAO+SN+*HST* constraint is robust. This figure shows that the lower limit on $N_{\rm eff}$ comes solely from the *WMAP* data. The 68% interval from *WMAP*+BAO+SN+*HST*, $N_{\rm eff} = 4.4 \pm 1.5$, is consistent with the standard value, 3.04, which is shown by the vertical line.

there is already "tension" between the high level of fluctuations seen in the Lyman alpha forest and the amplitude of mass fluctuations inferred from *WMAP* (Lesgourgues et al. 2007), the relationship between gas temperature and density appears to be more complicated than assumed in the previous Lyα forest analysis (Kim et al. 2007; Bolton et al. 2008), and additional astrophysics could potentially be the source of some of the small-scale fluctuations seen in the Lyα forest data. Given the power of the Lyα forest data, it is important to address these issues; however, they are beyond the scope of this paper.

In this paper, we take the more conservative approach and use only the *WMAP* data and the distance measures to place limits on the neutrino masses. Our approach is more conservative than Goobar et al. (2006), who have found a limit of 0.62 eV on the sum of the neutrino mass from the *WMAP* 3-year data, the SDSS–LRG BAO measurement, the SNLS SN data, and the shape of the galaxy power spectra from the SDSS main sample and 2dFGRS. While we use the *WMAP* 5-year data, the SDSS+2dFGRS BAO measurements, and the union SN data, we do not use the shape of the galaxy power spectra. See Section 2.3 in this paper or Dunkley et al. (2009) for more detail on this choice.

In summary, we do not use the amplitude or shape of the matter power spectrum, but exclusively rely on the CMB data and the distance measurements. As a result, our limits are weaker than the strongest limits in the literature.

Next, let us discuss (2), the choice of parameters. A few correlations between the neutrino mass and other cosmological parameters have been identified. Hannestad (2005) has found that the limit on the neutrino mass degrades significantly when the dark energy equation of state, w, is allowed to vary (also see Figure 18 of Spergel et al. 2007). This correlation would arise only when the amplitude of the galaxy or Lyα forest power spectrum was included, as the dark energy equation of state influences the growth rate of the structure formation. Since we do not include them, our limit on the neutrino mass is not degenerate with w. We shall come back to this point later in the Section 6.1.3. Incidentally, our limit is not degenerate with the running index, $dn_s/d\ln k$, or the tensor-to-scalar ratio, r.

6.1.3. Results

Figure 17 summarizes our limits on the sum of neutrino masses, $\sum m_\nu$.

With the *WMAP* data alone we find $\sum m_\nu < 1.3$ eV (95% CL) for the ΛCDM model in which $w = -1$, and $\sum m_\nu < 1.5$ eV (95% CL) for $w \neq -1$. We assume a flat universe in both cases. These constraints are very similar, which means that w and $\sum m_\nu$ are not degenerate. We show this more explicitly on the right panel of Figure 17.

When the BAO and SN data are added, our limits improve significantly, by a factor 2, to $\sum m_\nu < 0.67$ eV (95% CL) for $w = -1$, and $\sum m_\nu < 0.80$ eV (95% CL) for $w \neq -1$. Again, we do not observe much correlation between w and $\sum m_\nu$. While the distances out to *either* BAO or SN cannot reduce correlation between Ω_m (or H_0) and w, a combination of the two can reduce this correlation effectively, leaving little correlation left on the right panel of Figure 17.

What information do BAO and SN add to improve the limit on $\sum m_\nu$? It's the Hubble constant, H_0, as shown in the left panel of Figure 17. This effect has been explained by Ichikawa et al. (2005) as follows.

The massive neutrinos modify the CMB power spectrum by their changing the matter-to-radiation ratio at the decoupling epoch. If the sum of degenerate neutrino masses is below 1.8 eV, the neutrinos were still relativistic at the decoupling epoch. However, *they are definitely nonrelativistic at the present epoch*, as the neutrino oscillation experiments have shown that at least one neutrino species is heavier than 0.05 eV. This means that the Ω_m that we measure must be the sum of Ω_b, Ω_c, and Ω_ν; however, at the decoupling epoch, neutrinos were still relativistic, and thus the matter density at the decoupling epoch was actually smaller than a naive extrapolation from the present value.

As the matter-to-radiation ratio was smaller than one would naively expect, it would accelerate the decay of gravitational potential around the decoupling epoch. This leads to an enhancement in the so-called early integrated Sachs–Wolfe (ISW) effect. The larger $\sum m_\nu$ is, the larger early ISW becomes, as long as the neutrinos were still relativistic at the decoupling epoch, that is, $\sum m_\nu \lesssim 1.8$ eV.

The large ISW causes the first peak position to shift to lower multipoles by adding power at $l \sim 200$; however, this shift can be absorbed by a reduction in the value of H_0.[51] This is why $\sum m_\nu$ and H_0 are anticorrelated (see Ichikawa et al. 2005, for a further discussion on this subject).

It is the BAO distance that provides a better limit on H_0, as BAO is an absolute distance indicator. The SN is totally insensitive to H_0, as their absolute magnitudes have been marginalized over (SN is a relative distance indicator); however, the SN data do help reduce the correlation between w and H_0 when w is allowed to vary. As a result, we have equally tight limits on $\sum m_\nu$ regardless of w.

Our limit, $\sum m_\nu < 0.67$ eV (95% CL) (for $w = -1$), is weaker than the best limit quoted in the literature, as we have not used the information on the amplitude of fluctuations traced by the large-scale structure. The middle panel of Figure 17 shows how the *WMAP* data combined with BAO and SN predict the present-day amplitude of matter fluctuations, σ_8, as a function of $\sum m_\nu$. From this, it is clear that an accurate, *independent* measurement of σ_8 will reduce the correlation between σ_8 and $\sum m_\nu$, and provide a significant improvement in the limit on $\sum m_\nu$.

Improving upon our understanding of nonlinear astrophysical effects, such as those raised by Bolton et al. (2008) for the Lyα forest data and Sánchez & Cole (2008) for the SDSS and 2dFGRS data, is a promising way to improve upon the numerical value of the limit, as well as the robustness of the limit, on the mass of neutrinos.

6.2. Effective Number of Neutrino Species

6.2.1. Motivation

While the absolute mass of neutrinos is unknown, the number of neutrino species is well known: it is 3. The high precision measurement of the decay width of Z into neutrinos (the total decay width minus the decay width to quarks and charged leptons), carried out by LEP using the production of Z in e^+e^- collisions, has yielded $N_\nu = 2.984 \pm 0.008$ (Yao et al. 2006). However, are there any *other* particles that we do not know yet, and that are relativistic at the photon decoupling epoch?

Such extra relativistic particle species can change the expansion rate of the universe during the radiation era. As a result, they change the predictions from the BBN for the abundance of light elements such as helium and deuterium (Steigman et al. 1977). One can use this property to place a tight bound on the relativistic dof, expressed in terms of the "effective number of neutrino species," $N_{\rm eff}$ (see Equation (84) for the precise definition). As the BBN occurred at the energy of ~ 0.1 MeV, which is later than the neutrino decoupling epoch immediately followed by e^+e^- annihilation, the value of $N_{\rm eff}$ for three neutrino species is slightly larger than 3. With other subtle corrections included, the current standard value is $N_{\rm eff}^{\rm standard} = 3.04$ (Dicus et al. 1982; Gnedin & Gnedin 1998; Dolgov et al. 1999; Mangano et al. 2002). The 2σ interval for $N_{\rm eff}$ from the observed helium abundance, $Y_P = 0.240 \pm 0.006$, is $1.61 < N_{\rm eff} < 3.30$ (see Steigman 2007, for a recent summary).

Many people have been trying to find evidence for the extra relativistic dof in the universe, using the cosmological probes such as CMB and the large-scale structure (Pierpaoli 2003; Hannestad 2003; Crotty et al. 2003b, 2004; Barger et al. 2003; Trotta & Melchiorri 2005; Lattanzi et al. 2005; Cirelli & Strumia 2006; Hannestad 2006a; Ichikawa et al. 2007; Mangano et al. 2007; Hamann et al. 2007; de Bernardis et al. 2008). There is a strong motivation to seek the answer for the following question, "can we detect the cosmic neutrino background, and confirm that the signal is consistent with the expected number of neutrino species that we know?" Although we cannot detect the cosmic neutrino background directly yet, there is a possibility that we can detect it indirectly by looking for the signatures of neutrinos in the CMB power spectrum.

In this section, we shall revisit this classical problem by using the *WMAP* 5-year data as well as the distance information from BAO and SN, and Hubble's constant measured by *HST*.

6.2.2. Analysis

It is common to write the energy density of neutrinos (including antineutrinos), when they were still relativistic, in terms of the effective number of neutrino species, $N_{\rm eff}$, as

$$\rho_\nu = N_{\rm eff} \frac{7\pi^2}{120} T_\nu^4, \tag{82}$$

where T_ν is the temperature of neutrinos. How do we measure $N_{\rm eff}$ from CMB?

The way that we use CMB to determine $N_{\rm eff}$ is relatively simple. The relativistic particles that stream freely influence CMB in two ways: (1) their energy density changing the matter-radiation equality epoch and (2) their anisotropic stress acting as an additional source for the gravitational potential via Einstein's equations. Incidentally, the relativistic particles that *do not* stream freely, but interact with matter frequently, do not have a significant anisotropic stress because they isotropize themselves via interactions with matter; thus, anisotropic stress of photons before the decoupling epoch was very small. Neutrinos, on the other hand, decoupled from matter much earlier (~ 2 MeV), and thus their anisotropic stress was significant at the decoupling epoch.

The amount of the early ISW effect changes as the equality redshift changes. The earlier the equality epoch is, the more the ISW effect CMB photons receive. This effect can be measured via the height of the third acoustic peak relative to the first peak. Therefore, the equality redshift, $z_{\rm eq}$, is one of the fundamental observables that one can extract from the CMB power spectrum.

One usually uses $z_{\rm eq}$ to determine $\Omega_m h^2$ from the CMB power spectrum, without noticing that it is actually $z_{\rm eq}$ that they are measuring. However, the conversion from $z_{\rm eq}$ to $\Omega_m h^2$ is automatic only when one knows the radiation content of the universe exactly—in other words, when one knows $N_{\rm eff}$ exactly:

$$1 + z_{\rm eq} = \frac{\Omega_m}{\Omega_r} = \frac{\Omega_m h^2}{\Omega_\gamma h^2} \frac{1}{1 + 0.2271 N_{\rm eff}}, \tag{83}$$

where $\Omega_\gamma h^2 = 2.469 \times 10^{-5}$ is the present-day photon energy density parameter for $T_{\rm cmb} = 2.725$ K. Here, we have used the

[51] This is similar to what happens to the curvature constraint from the CMB data alone. A positive curvature model, $\Omega_k < 0$, shifts the acoustic peaks to lower multipoles; however, this shift can be absorbed by a reduction in the value of H_0. As a result, a closed universe with $\Omega_k \sim -0.3$ and $\Omega_\Lambda \sim 0$ is still a good fit, if Hubble's constant is as low as $H_0 \sim 30\,{\rm km\,s^{-1}\,Mpc^{-1}}$ (Spergel et al. 2007).

standard relation between the photon temperature and neutrino temperature, $T_\nu = (4/11)^{1/3} T_\gamma$, derived from the entropy conservation across the electron–positron annihilation (see, e.g., Weinberg 1972; Kolb & Turner 1990).

However, if we do not know $N_{\rm eff}$ precisely, it is not possible to use $z_{\rm eq}$ to measure $\Omega_m h^2$. In fact, we lose our ability to measure $\Omega_m h^2$ from CMB almost completely if we do not know $N_{\rm eff}$. Likewise, if we do not know $\Omega_m h^2$ precisely, it is not possible to use $z_{\rm eq}$ to measure $N_{\rm eff}$. As a result, $N_{\rm eff}$ and $\Omega_m h^2$ are linearly correlated (degenerate), with the width of the degeneracy line given by the uncertainty in our determination of $z_{\rm eq}$.

The distance information from BAO and SN provides us with an independent constraint on $\Omega_m h^2$, which helps to reduce the degeneracy between $z_{\rm eq}$ and $\Omega_m h^2$.

The anisotropic stress of neutrinos also leaves distinct signatures in the CMB power spectrum, which is not degenerate with $\Omega_m h^2$ (Hu et al. 1995; Bashinsky & Seljak 2004). Trotta & Melchiorri (2005; also see Melchiorri & Serra 2006) have reported on evidence for the neutrino anisotropic stress at slightly more than 95% CL. They have parametrized the anisotropic stress by the viscosity parameter, $c^2_{\rm vis}$ (Hu 1998), and found $c^2_{\rm vis} > 0.12$ (95% CL). However, they had to combine the *WMAP* 1-year data with the SDSS data to see the evidence for nonzero $c^2_{\rm vis}$.

In Dunkley et al. (2009), we reported on the lower limit to $N_{\rm eff}$ solely from the *WMAP* 5-year data. In this paper, we shall combine the *WMAP* data with the distance information from BAO and SN as well as Hubble's constant from *HST* to find the best-fitting value of $N_{\rm eff}$.

6.2.3. Results

Figure 18 shows our constraint on $N_{\rm eff}$. The contours in the left panel lie on the expected linear correlation between $\Omega_m h^2$ and $N_{\rm eff}$ given by

$$N_{\rm eff} = 3.04 + 7.44 \left(\frac{\Omega_m h^2}{0.1308} \frac{3139}{1 + z_{\rm eq}} - 1 \right), \qquad (84)$$

which follows from Equation (83). Here, $\Omega_m h^2 = 0.1308$ and $z_{\rm eq} = 3138$ are the maximum likelihood values from the simplest ΛCDM model. The width of the degeneracy line is given by the accuracy of our determination of $z_{\rm eq}$, which is given by $z_{\rm eq} = 3141^{+154}_{-157}$ (*WMAP*-only) for this model. Note that the mean value of $z_{\rm eq}$ for the simplest ΛCDM model with $N_{\rm eff} = 3.04$ is $z_{\rm eq} = 3176^{+151}_{-150}$, which is close. This confirms that $z_{\rm eq}$ is one of the fundamental observables, and $N_{\rm eff}$ is merely a secondary parameter that can be derived from $z_{\rm eq}$. The middle panel of Figure 18 shows this clearly: $z_{\rm eq}$ is determined independently of $N_{\rm eff}$. For each value of $N_{\rm eff}$ along a constant $z_{\rm eq}$ line, there is a corresponding $\Omega_m h^2$ that gives the same value of $z_{\rm eq}$ along the line.

However, the contours do not extend all the way down to $N_{\rm eff} = 0$, although Equation (84) predicts that $N_{\rm eff}$ should go to zero when $\Omega_m h^2$ is sufficiently small. This indicates that we see the effect of the neutrino anisotropic stress at a high significance. While we need to repeat the analysis of Trotta & Melchiorri (2005) in order to prove that our finding of $N_{\rm eff} > 0$ comes from the neutrino anisotropic stress, we believe that there is a strong evidence that we see nonzero $N_{\rm eff}$ via the effect of neutrino anisotropic stress, rather than via $z_{\rm eq}$.

While the *WMAP* data alone can give a lower limit on $N_{\rm eff}$ (Dunkley et al. 2009), they cannot give an upper limit owing to the strong degeneracy with $\Omega_m h^2$. Therefore, we use the BAO, SN, and *HST* data to break the degeneracy. We find $N_{\rm eff} = 4.4 \pm 1.5$ (68%) from *WMAP*+BAO+SN+*HST*, which is fully consistent with the standard value, 3.04 (see the right panel of Figure 18).

7. CONCLUSION

With 5-years of integration, the *WMAP* temperature and polarization data have improved significantly. An improved determination of the third acoustic peak has enabled us to reduce the uncertainty in the amplitude of matter fluctuation, parametrized by σ_8, by a factor of 1.4 from the *WMAP* 3-year result. The E-mode polarization is now detected at five standard deviations (see 3.0 standard deviations for the 3-year data; Page et al. 2007), which rules out an instantaneous reionization at $z_{\rm reion} = 6$ at the 3.5σ level. Overall, the *WMAP* 5-year data continue to support the simplest, six-parameter ΛCDM model (Dunkley et al. 2009).

In this paper, we have explored our ability to limit deviations from the simplest picture, namely non-Gaussianity, nonadiabatic fluctuations, nonzero gravitational waves, nonpower-law spectrum, nonzero curvature, dynamical dark energy, parity-violating interactions, nonzero neutrino mass, and nonstandard number of neutrino species. Detection of any of these items will immediately lead us to the new era in cosmology and a better understanding of the physics of our universe.

From these studies, we conclude that we have not detected any convincing deviations from the simplest six-parameter ΛCDM model at the level greater than 99% CL. By combining *WMAP* data with the distance information from BAO and SN, we have improved the accuracy of the derived cosmological parameters. As the distance information provides strong constraints on the matter density (both BAO and SN) and Hubble's constant (BAO), the uncertainties in $\Omega_m h^2$ and H_0 have been reduced by factors of 1.7 and 2, respectively, from the *WMAP*-only limits. The better determination of H_0 reduces the uncertainty in Ω_Λ (as well as Ω_b and Ω_c) by a factor of 2, and the better determination of $\Omega_m h^2$ reduces the uncertainty in σ_8 by a factor of 1.4. These results are presented visually in Figure 19. Also see Table 1 for the summary of the cosmological parameters of the ΛCDM model. The addition of BAO and SN does not improve the determinations of $\Omega_b h^2$ or τ as expected. Since n_s is mainly degenerate with $\Omega_b h^2$ and τ, with the former being more degenerate, the addition of BAO and SN does not improve our determination of n_s, when we consider the simplest six-parameter ΛCDM model.

To find the limits on various deviations from the simplest model, we have explored the parameter space by combining the *WMAP* 5-year data with the distance measurements from the BAO and Type Ia SN observations. Here, we summarize significant findings from our analysis (also see Table 2).

1. **Gravitational waves and primordial power spectrum.** Improved simultaneous constraint on the amplitude of primordial gravitational waves and the shape of the primordial power spectrum (from *WMAP*+BAO+SN). In terms of the tensor-to-scalar ratio, r, we have found $r < 0.22$ (95% CL), which is the tightest bound to date. A blue primordial spectrum index, $n_s > 1$, now begins to be disfavored even in the presence of gravitational waves. We find no evidence for the running index, $dn_s/d\ln k$. The parameter space allowed for inflation models has shrunk significantly since the 3-year data release (Section 3.3), most notably for models that produce significant gravitational waves, such as chaotic or power-law inflation models, and models that produce $n_s > 1$, such as hybrid inflation models.

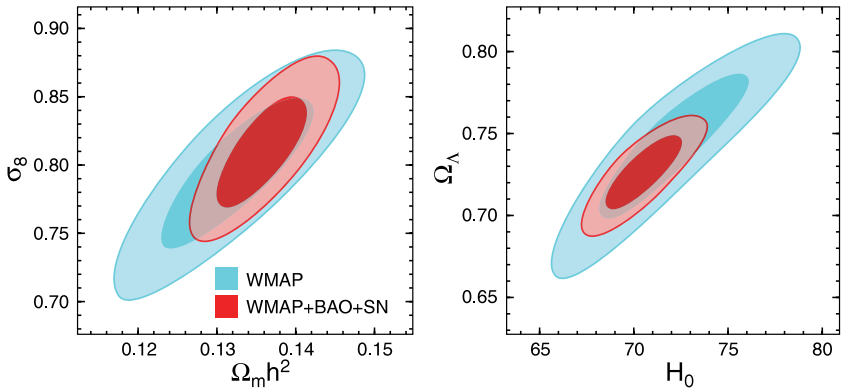

Figure 19. Four representative cosmological parameters that have improved significantly by adding the BAO and SN data. (Also see Table 1.) The contours show the 68% and 95% CL. The *WMAP*-only constraint is shown in blue, while *WMAP*+BAO+SN in red. (Left) The distance information from BAO and SN provides a better determination of $\Omega_m h^2$, which results in 40% better determination of σ_8. (Right) The BAO data, being the absolute distance indicator, provides a better determination of H_0, which results in a factor of 2 better determination of Ω_Λ, Ω_b, and Ω_c.

2. **Dark energy and curvature.** Improved simultaneous constraint on the dark energy equation of state, w, and the spatial curvature of the universe, Ω_k (from *WMAP*+BAO+SN). We find $-0.0179 < \Omega_k < 0.0081$ (95% CL) and $-0.14 < 1 + w < 0.12$ (95% CL). The curvature radius of the universe should be greater than $R_{\rm curv} > 22$ and $33\,h^{-1}$ Gpc for positive and negative curvatures, respectively. The combination of *WMAP*, BAO, and SN is particularly powerful for constraining w and Ω_k simultaneously.
3. **Time-dependent equation of state.** Using the *WMAP* distance priors (l_A, R, z_*) combined with the BAO and SN distance data, we have constrained time-dependent w. The present-day value of w, w_0, is constrained as $-0.33 < 1 + w_0 < 0.21$ (95% CL), for a flat universe.
4. **Non-Gaussianity.** Improved constraints on primordial non-Gaussianity parameters, $-9 < f_{\rm NL}^{\rm local} < 111$ and $-151 < f_{\rm NL}^{\rm equil} < 253$ (95% CL), from the *WMAP* temperature data. The Gaussianity tests show that the primordial fluctuations are Gaussian to the 0.1% level, which provides the strongest evidence for the quantum origin of the primordial fluctuations.
5. **Nonadiabaticity.** Improved constraints on nonadiabatic fluctuations. The photon and matter fluctuations are found to obey the adiabatic relation to 8.9% and 2.1% for axion- and curvaton-type nonadiabatic fluctuations, respectively.
6. **Parity violation.** *WMAP*'s limits on the TB and EB correlations indicate that parity-violating interactions that couple to photons could not have rotated the polarization angle by more than $-5.^\circ9 < \Delta\alpha < 2.^\circ4$ between the decoupling epoch and present epoch.
7. **Neutrino mass.** With the *WMAP* data combined with the distance information from BAO and SN, we find a limit on the neutrino mass, $\sum m_\nu < 0.67$ eV (95% CL), which is better than the WMAP-only limit by a factor of 2, owing to an additional constraint on H_0 provided by BAO. The limit does not get worse very much even when w is allowed to vary, as the SN data reduce correlation between H_0 and w effectively. Since we rely only on the CMB data and distance information, our limit is not sensitive to our understanding of nonlinear astrophysical effects in the large-scale structure data.
8. **Number of neutrino species.** With the *WMAP* data alone, we find evidence for nonzero $N_{\rm eff}$ (Dunkley et al. 2009), which is likely coming from our measurement of the effect of neutrino anisotropic stress on the CMB power spectrum. With the BAO, SN, and *HST* added, we break the degeneracy between $\Omega_m h^2$ and $N_{\rm eff}$, and find $N_{\rm eff} = 4.4 \pm 1.5$ (68% CL) and $1.8 < N_{\rm eff} < 7.6$ (95% CL), which are consistent with the standard value, $N_{\rm eff} = 3.04$; thus, we do not find any evidence for the extra relativistic species in the universe.

The limits that we have obtained from our analysis in this paper are already quite stringent; however, we emphasize that they should still be taken as a prototype of what we can achieve in the future, including more integration of the *WMAP* observations.

A smaller noise level in the temperature data will reduce the uncertainty in non-Gaussianity parameters. An improved determination of the TE spectrum increases our sensitivity to nonadiabatic fluctuations and to the primordial gravitational waves. The E-mode polarization will be more dominated by the signal, to the point where we begin to constrain the detailed history of the reionization of the universe beyond a simple parametrization. Our limit on the B-mode polarization continues to improve, which will provide us with a better understanding of the polarized foreground. The improved TB and EB correlations will provide better limits on the cosmological birefringence.

While we have chosen to combine the *WMAP* data mainly with the distance indicators, one should be able to put even more stringent limits on important parameters such as r, n_s, $dn_s/d\ln k$, $w(z)$, m_ν, and $N_{\rm eff}$, by including the other datasets that are sensitive to the *amplitude* of density fluctuations, such as the amplitude of the galaxy power spectrum, Lyα forest, weak lensing, and cluster abundance. With the Lyα forest data from Seljak et al. (2006), for example, the limit on the running index improves from $-0.068 < dn_s/d\ln k < 0.012$ (95% CL) to $-0.034 < dn_s/d\ln k < 0.011$ (95% CL) for $r = 0$, and $-0.11484 < dn_s/d\ln k < -0.00079$ (95% CL) to $-0.0411 < dn_s/d\ln k < 0.0067$ (95% CL) for $r \neq 0$. A better understanding of systematic errors in these methods will be crucial in improving our understanding of the physics of our universe. Hints for new physics may well be hidden in the deviations from the simplest six-parameter ΛCDM model.

The *WMAP* mission is made possible by the support of the Science Mission Directorate Office at NASA Headquarters. This research was additionally supported by NASA grants NNG05GE76G, NNX07AL75G S01, LTSA03-000-

0090, ATPNNG04GK55G, and ADP03-0000-092. E.K. acknowledges support from an Alfred P. Sloan Research Fellowship. We thank M. Greason and N. Odegard for their help on the analysis of the *WMAP* data, and B. Griswold for the artwork. We thank U. Seljak, A. Slosar, and P. McDonald for providing the Lyα forest likelihood code, W. Percival for useful information on the implementation of the BAO data, E. Hivon for providing a new HEALPix routine to remove the monopole and dipole from the weighted temperature maps, and K. Smith for his help on implementing the bispectrum optimization algorithm. We thank A. Conley for valuable comments on our original treatment of the Type Ia SN data, and M. Kowalski, J. Guy, and A. Slosar for making the union SN data available to us. Computations for the analysis of non-Gaussianity in Section 3.5 were carried out by the Terascale Infrastructure for Groundbreaking Research in Engineering and Science (TIGRESS) at the Princeton Institute for Computational Science and Engineering (PICSciE). This research has made use of NASA's Astrophysics Data System Bibliographic Services. We acknowledge use of the HEALPix (Gorski et al. 2005), CAMB (Lewis et al. 2000), and CMBFAST (Seljak & Zaldarriaga 1996) packages.

APPENDIX A

FAST CUBIC ESTIMATORS

We use the following estimators for $f_{\rm NL}^{\rm local}$, $f_{\rm NL}^{\rm equil}$, and $b_{\rm src}$ (the amplitude of the point-source bispectrum):

$$f_{\rm NL}^{\rm local} = (F^{-1})_{11} S_1 + (F^{-1})_{12} S_2 + (F^{-1})_{13} S_3, \tag{A1}$$

$$f_{\rm NL}^{\rm equil} = (F^{-1})_{21} S_1 + (F^{-1})_{22} S_2 + (F^{-1})_{23} S_3, \tag{A2}$$

$$b_{\rm src} = (F^{-1})_{31} S_1 + (F^{-1})_{32} S_2 + (F^{-1})_{33} S_3, \tag{A3}$$

where F_{ij} is the Fisher matrix given by

$$F_{ij} \equiv \sum_{2 \leqslant l_1 \leqslant l_2 \leqslant l_3} \frac{B^{(i)}_{l_1 l_2 l_3} B^{(j)}_{l_1 l_2 l_3}}{\tilde{C}_{l_1} \tilde{C}_{l_2} \tilde{C}_{l_3}}. \tag{A4}$$

Here, $B^{(i)}_{l_1 l_2 l_3}$ are theoretically calculated angular bispectra (given below), where $i = 1$ is used for $f_{\rm NL}^{\rm local}$, $i = 2$ for $f_{\rm NL}^{\rm equil}$, and $i = 3$ for $b_{\rm src}$. The denominator of F_{ij} contains the total power spectrum including the CMB signal ($C_l^{\rm CMB}$) and noise (N_l), $\tilde{C}_l \equiv C_l^{\rm CMB} b_l^2 + N_l$, and b_l is the beam transfer function given in Hill et al. (2009).

While this formula allows one to estimate $f_{\rm NL}^{\rm local}$, $f_{\rm NL}^{\rm equil}$, and $b_{\rm src}$ simultaneously, we find that a simultaneous estimation does not change the results significantly. Therefore, we use

$$f_{\rm NL}^{\rm local} = S_1/F_{11}, \qquad f_{\rm NL}^{\rm equil} = S_2/F_{22}, \qquad b_{\rm src} = S_3/F_{33}, \tag{A5}$$

to simplify the analysis, as well as to make the comparison with the previous work easier. However, we do take into account a potential leakage of the point sources into $f_{\rm NL}^{\rm local}$ and $f_{\rm NL}^{\rm equil}$ by using the Monte Carlo simulation of point sources, as described later. These Monte Carlo estimates of the bias in $f_{\rm NL}^{\rm local}$ and $f_{\rm NL}^{\rm equil}$ due to the source contamination roughly agree with contributions from the off-diagonal terms in Equations (A1) and (A2).

Assuming white noise, which is a good approximation at high multipoles in which noise becomes important, one can analytically compute the noise power spectrum as

$$N_l = \Omega_{\rm pix} \int \frac{d^2\hat{\mathbf{n}}}{4\pi f_{\rm sky}} \frac{\sigma_0^2 M(\hat{\mathbf{n}})}{N_{\rm obs}(\hat{\mathbf{n}})}, \tag{A6}$$

where $\Omega_{\rm pix} \equiv 4\pi/N_{\rm pix}$ is the solid angle per pixel, $M(\hat{\mathbf{n}})$ is the *KQ75* mask, $f_{\rm sky} = 0.718$ is the fraction of sky retained by the *KQ75* mask, σ_0 is the rms noise per observation, and $N_{\rm obs}(\hat{\mathbf{n}})$ is the number of observations per pixel.

The angular bispectra are given by

$$B^{(1)}_{l_1 l_2 l_3} = 2 I_{l_1 l_2 l_3} \int_0^\infty r^2 dr [\alpha_{l_1}(r) \beta_{l_2}(r) \beta_{l_3}(r) + ({\rm cyc.})], \tag{A7}$$

$$B^{(2)}_{l_1 l_2 l_3} = -3 B^{(1)}_{l_1 l_2 l_3} + 6 I_{l_1 l_2 l_3} \int_0^\infty r^2 dr \{[\beta_{l_1}(r) \gamma_{l_2}(r) \delta_{l_3}(r) + ({\rm cyc.})] - 2 \delta_{l_1}(r) \delta_{l_2}(r) \delta_{l_3}(r)\}, \tag{A8}$$

$$B^{(3)}_{l_1 l_2 l_3} = I_{l_1 l_2 l_3}, \tag{A9}$$

where

$$I_{l_1 l_2 l_3} \equiv \sqrt{\frac{(2l_1+1)(2l_2+1)(2l_3+1)}{4\pi}} \begin{pmatrix} l_1 & l_1 & l_3 \\ 0 & 0 & 0 \end{pmatrix}. \tag{A10}$$

Various functions in $B^{(i)}_{l_1 l_2 l_3}$ are given by

$$\alpha_l(r) \equiv \frac{2}{\pi} \int k^2 dk g_{Tl}(k) j_l(kr), \tag{A11}$$

$$\beta_l(r) \equiv \frac{2}{\pi} \int k^2 dk P_\Phi(k) g_{Tl}(k) j_l(kr), \tag{A12}$$

$$\gamma_l(r) \equiv \frac{2}{\pi} \int k^2 dk P_\Phi^{1/3}(k) g_{Tl}(k) j_l(kr), \tag{A13}$$

$$\delta_l(r) \equiv \frac{2}{\pi} \int k^2 dk P_\Phi^{2/3}(k) g_{Tl}(k) j_l(kr). \tag{A14}$$

Here, $P_\Phi(k) \propto k^{n_s - 4}$ is the primordial power spectrum of Bardeen's curvature perturbations, and $g_{Tl}(k)$ is the radiation transfer function that gives the angular power spectrum as $C_l = (2/\pi) \int k^2 dk P_\Phi(k) g_{Tl}^2(k)$.

The skewness parameters, S_i, are given by (Komatsu et al. 2005; Babich 2005; Creminelli et al. 2006; Yadav et al. 2008)

$$S_1 \equiv 4\pi \int r^2 dr \int \frac{d^2\hat{\mathbf{n}}}{w_3} \big[A(\hat{\mathbf{n}}, r) B^2(\hat{\mathbf{n}}, r) - 2 B(\hat{\mathbf{n}}, r) \langle A_{\rm sim}(\hat{\mathbf{n}}, r) B_{\rm sim}(\hat{\mathbf{n}}, r) \rangle_{\rm MC} - A(\hat{\mathbf{n}}, r) \times \langle B^2_{\rm sim}(\hat{\mathbf{n}}, r) \rangle_{\rm MC} \big], \tag{A15}$$

$$S_2 \equiv -3 S_1 + 24\pi \int r^2 dr \int \frac{d^2\hat{\mathbf{n}}}{w_3} \Big\{ [B(\hat{\mathbf{n}}, r) C(\hat{\mathbf{n}}, r) D(\hat{\mathbf{n}}, r) - B(\hat{\mathbf{n}}, r) \langle C_{\rm sim}(\hat{\mathbf{n}}, r) D_{\rm sim}(\hat{\mathbf{n}}) \rangle_{\rm MC} - C(\hat{\mathbf{n}}, r) \langle B_{\rm sim}(\hat{\mathbf{n}}, r) \times D_{\rm sim}(\hat{\mathbf{n}}) \rangle_{\rm MC} - D(\hat{\mathbf{n}}, r) \langle B_{\rm sim}(\hat{\mathbf{n}}, r) C_{\rm sim}(\hat{\mathbf{n}}, r) \rangle_{\rm MC}] - \frac{1}{3} [D^3(\hat{\mathbf{n}}, r) - 3 D(\hat{\mathbf{n}}, r) \langle D^2_{\rm sim}(\hat{\mathbf{n}}, r) \rangle_{\rm MC}] \Big\} \tag{A16}$$

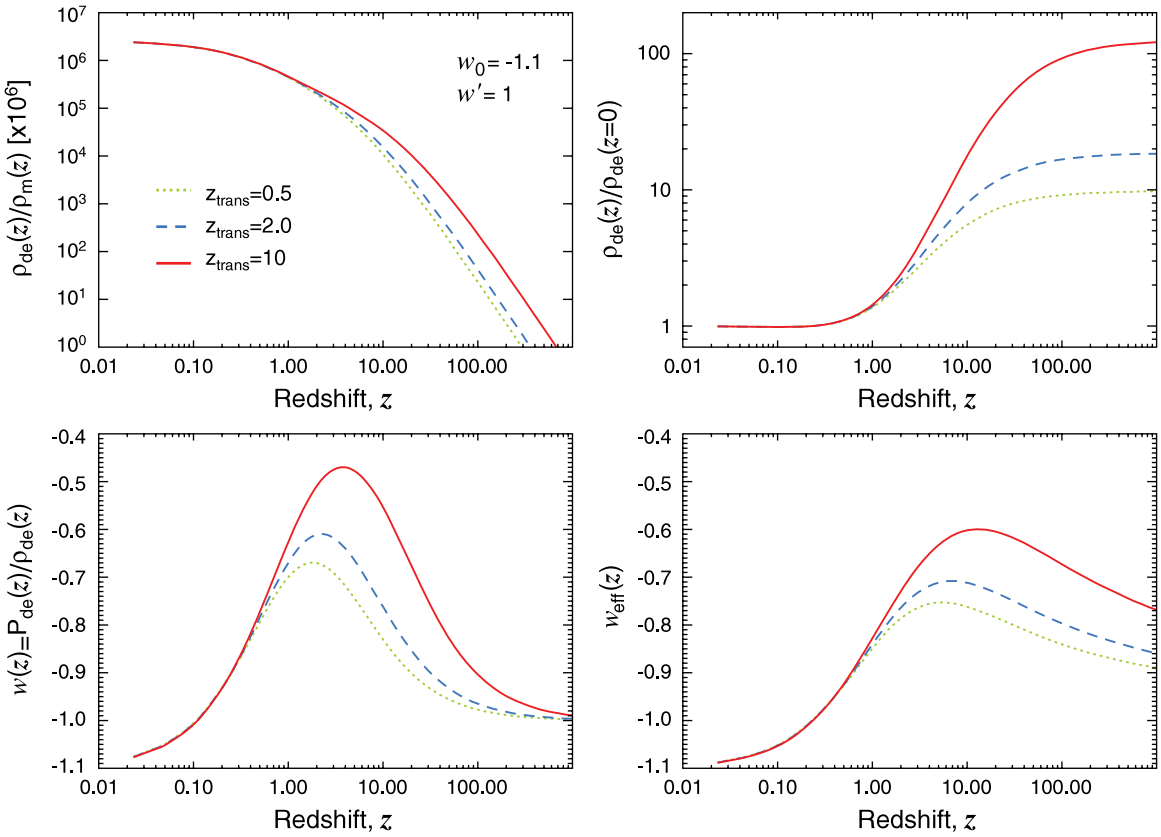

Figure 20. Evolution of dark energy for $w_0 = -1.1$ and $w' = 1$, and various transition redshifts, $z_{\rm trans} = 0.5$, 2, and 10, above which $w(z)$ approaches -1. (Top left) Evolution of the dark energy to matter density ratio as a function of z. Note that the vertical axis has been multiplied by 10^6. (Top right) Evolution of the dark energy density relative to the dark energy density at present. The dark energy density was nearly constant at high redshifts above $z_{\rm trans}$; thus, these models can describe the "thawing models" (Caldwell & Linder 2005), in which dark energy was nearly constant at early times, and had become dynamical at lower redshifts. (Bottom left) Evolution of the equation of state, $w(z) = P_{\rm de}(z)/\rho_{\rm de}(z)$. By construction of the model, $w(z)$ approaches -1 beyond $z_{\rm trans}$. (Bottom right) Evolution of the effective equation of state, $w_{\rm eff}(z)$, which determines the evolution of dark energy density as $\rho_{\rm de}(z) = \rho_{\rm de}(0)(1+z)^{3[1+w_{\rm eff}(z)]}$.

$$S_3 \equiv \frac{2\pi}{3}\int \frac{d^2\hat{\mathbf{n}}}{w_3}\left[E^3(\hat{\mathbf{n}}) - 3E(\hat{\mathbf{n}})\left\langle E^2_{\rm sim}(\hat{\mathbf{n}})\right\rangle_{\rm MC}\right], \tag{A17}$$

where w_3 is the sum of the weighting function cubed:

$$w_3 \equiv \int d^2\hat{\mathbf{n}} W^3(\hat{\mathbf{n}}). \tag{A18}$$

For a uniform weighting, the weighting function is simply given by the *KQ75* mask, that is, $W(\hat{\mathbf{n}}) = M(\hat{\mathbf{n}})$, which gives $w_3 = 4\pi f_{\rm sky}$. For our measurements of $f_{\rm NL}^{\rm local}$, $f_{\rm NL}^{\rm equil}$, and $b_{\rm src}$, we shall use a "combination signal-plus-noise weight," given by

$$W(\mathbf{n}) = \frac{M(\hat{\mathbf{n}})}{\sigma^2_{\rm cmb} + \sigma_0^2/N_{\rm obs}(\hat{\mathbf{n}})}, \tag{A19}$$

where $\sigma^2_{\rm cmb} \equiv (1/4\pi)\sum_l (2l+1)C_l^{\rm cmb} b_l^2$ is the CMB signal variance, σ_0 is the rms noise per observation, and $N_{\rm obs}(\hat{\mathbf{n}})$ is the number of observations per pixel. This combination weighting yields a nearly optimal performance for $b_{\rm src}$ and $f_{\rm NL}^{\rm equil}$, whereas it results in a minor improvement in $f_{\rm NL}^{\rm local}$ over the uniform weighting. The bracket, $\langle\rangle_{\rm MC}$, denotes the average over Monte Carlo realizations and "sim" denotes that these are the filtered maps of the Monte Carlo realizations.

The filtered temperature maps, A, B, C, D, and E, are given by

$$A(\hat{\mathbf{n}}, r) \equiv \sum_{l=2}^{l_{\rm max}}\sum_{m=-l}^{l} \alpha_l(r)\frac{b_l}{\tilde{C}_l} a_{lm} Y_{lm}(\hat{\mathbf{n}}), \tag{A20}$$

$$B(\hat{\mathbf{n}}, r) \equiv \sum_{l=2}^{l_{\rm max}}\sum_{m=-l}^{l} \beta_l(r)\frac{b_l}{\tilde{C}_l} a_{lm} Y_{lm}(\hat{\mathbf{n}}), \tag{A21}$$

$$C(\hat{\mathbf{n}}, r) \equiv \sum_{l=2}^{l_{\rm max}}\sum_{m=-l}^{l} \gamma_l(r)\frac{b_l}{\tilde{C}_l} a_{lm} Y_{lm}(\hat{\mathbf{n}}), \tag{A22}$$

$$D(\hat{\mathbf{n}}, r) \equiv \sum_{l=2}^{l_{\rm max}}\sum_{m=-l}^{l} \delta_l(r)\frac{b_l}{\tilde{C}_l} a_{lm} Y_{lm}(\hat{\mathbf{n}}), \tag{A23}$$

$$E(\hat{\mathbf{n}}) \equiv \sum_{l=2}^{l_{\rm max}}\sum_{m=-l}^{l} \frac{b_l}{\tilde{C}_l} a_{lm} Y_{lm}(\hat{\mathbf{n}}), \tag{A24}$$

respectively. Here, $l_{\rm max}$ is the maximum multipole that we use in the analysis. We vary $l_{\rm max}$ to see how much the results depend on $l_{\rm max}$.

Equations (A15) and (A16) involve the integrals over the conformal distances, r. We evaluate these integrals as

$$\int r^2 dr [\ldots](r) = \sum_i (w_i)_{\rm opt} r_i^2 \Delta r_i [\ldots](r_i). \tag{A25}$$

We use the bispectrum optimization algorithm described in Smith & Zaldarriaga (2006) to compute the optimal weights, $(w_i)_{\rm opt}$, and decide on which quadrature points, r_i, to keep. We choose the number of quadrature points such that the bispectrum computed in this way agrees with that from more dense sampling

in r to 10^{-5}, which typically gives ~ 5 quadrature points for $f_{\rm NL}^{\rm local}$ and ~ 15 points for $f_{\rm NL}^{\rm equil}$.[52]

The measurement of these estimators proceeds as follows.

1. Generate the simulated realizations of CMB signal maps, T_S, from the input signal power spectrum, $C_l^{\rm cmb}$, and the beam transfer function, b_l. We have generated 300 realizations for the analysis given in this paper.
2. Add random noise, T_N, using the rms noise per pixel given by $\sigma_0/\sqrt{N_{\rm obs}(\hat{\mathbf{n}})}$.
3. Add point sources. We use a simplified treatment for the source simulation,

$$\frac{T_{\rm src}(\hat{\mathbf{n}})}{2.725\,{\rm K}} = \left[\frac{\sinh^2(x/2)}{x^4}\frac{F_{\rm src}/\Omega_{\rm pix}}{67.55{\rm MJy}}\right]\epsilon, \tag{A26}$$

where $\Omega_{\rm pix}$ is the solid angle of pixel, $x = h\nu/(k_B T_{\rm cmb}) = 56.80\,{\rm GHz}$ (for $T_{\rm cmb} = 2.725$ K), ϵ is a Poisson random variable with the mean of $\langle\epsilon\rangle = n_{\rm src}\Omega_{\rm pix}$, and $n_{\rm src}$ is the average number of sources per steradians. This simplified model assumes that there is only one population of sources with a fixed flux, $F_{\rm src}$, and each source's flux is independent of frequency. We choose $n_{\rm src} = 0.85\,{\rm sr}^{-1}$ and $F_{\rm src} = 0.5\,{\rm Jy}$, which yields the source power spectrum in the Q band of $C_{\rm ps} = 8.7\times10^{-3}\,\mu{\rm K}^2\,{\rm sr}$ and the source bispectrum in the Q band of $b_{\rm src} = 8.7\times10^{-5}\,\mu{\rm K}^3\,{\rm sr}^2$, which roughly reproduce the measured values. However, this model does not reproduce the source counts very well. (The source density of $n_{\rm src} = 0.85\,{\rm sr}^{-1}$ at 0.5 Jy is too low.) The main purpose of this phenomenological model is to reproduce the power spectrum and bispectrum—we include point sources in the simulations, in order to take into account the potential effects of the unresolved sources on primordial non-Gaussianity, $f_{\rm NL}^{\rm local}$ and $f_{\rm NL}^{\rm equil}$.
4. Coadd them to create the simulated temperature maps, $T(\hat{\mathbf{n}}) = T_S(\hat{\mathbf{n}}) + T_N(\hat{\mathbf{n}}) + T_{\rm src}(\hat{\mathbf{n}})$.
5. Mask and weight the temperature maps, $T(\hat{\mathbf{n}}) \rightarrow \tilde{T}(\hat{\mathbf{n}}) = W(\hat{\mathbf{n}})T(\hat{\mathbf{n}})$, where $W(\hat{\mathbf{n}})$ is given by Equation (A19).
6. Remove the monopole and dipole from $\tilde{T}(\hat{\mathbf{n}})$.
7. Compute the harmonic coefficients as

$$a_{lm} = \int d^2\hat{\mathbf{n}}\tilde{T}(\hat{\mathbf{n}})Y^*_{lm}(\hat{\mathbf{n}}). \tag{A27}$$

8. Generate the filtered maps, $A_{\rm sim}$, $B_{\rm sim}$, $C_{\rm sim}$, $D_{\rm sim}$, and $E_{\rm sim}$, and compute the appropriate Monte Carlo averages such as $\langle A_{\rm sim}B_{\rm sim}\rangle_{\rm MC}$. This is the most time-consuming part.
9. Compute the filtered maps from the *WMAP* data. When we coadd the V- and W-band data, we weight them as $T_{V+W} = (T_V + 0.9T_W)/1.9$. The beam transfer function of the coadded map is given by $b_l^{V+W} = \left(b_l^V + 0.9b_l^W\right)/1.9$, and $\sigma_0/N_{\rm obs}$ of the coadded map is given by

$$\frac{\left(\sigma_0^{V+W}\right)^2}{N_{\rm obs}^{V+W}(\hat{\mathbf{n}})} = \frac{1}{1.9^2}\left[\frac{\left(\sigma_0^V\right)^2}{N_{\rm obs}^V(\hat{\mathbf{n}})} + \frac{\left(0.9\sigma_0^W\right)^2}{N_{\rm obs}^W(\hat{\mathbf{n}})}\right]. \tag{A28}$$

10. Compute the skewness parameters, S_i, from the filtered *WMAP* data, and obtain $f_{\rm NL}^{\rm local}$, $f_{\rm NL}^{\rm equil}$, and $b_{\rm src}$, either jointly or separately.
11. Compute these parameters from the simulated realizations as well, and obtain the uncertainties.

For the computations of $g_{Tl}(k)$ and generation of Monte Carlo realizations, we have used the maximum-likelihood values of the *WMAP* 3-year data (the power-law ΛCDM model fit by the *WMAP* data alone with the Sunyaev–Zel'dovich effect marginalized): $\Omega_b = 0.0414$, $\Omega_{\rm CDM} = 0.1946$, $\Omega_\Lambda = 0.7640$, $H_0 = 73.2\,{\rm km\,s^{-1}\,Mpc^{-1}}$, $\tau = 0.091$, and $n_s = 0.954$ (Spergel et al. 2007). These parameters yield the conformal distance to $t = 0$ as $c\tau_0 = 14.61$ Gpc.

APPENDIX B

AXION

In this Appendix, we derive relations among the tensor-to-scalar ratio r, the axion mass density $\Omega_a h^2$, the entropy-to-curvature perturbation ratio α, the phase of the Pecci–Quinn field θ_a, and the axion decay constant f_a.

Let us write the expectation value of the complex Pecci–Quinn field, $\psi_{\rm PQ}$, as

$$\langle\psi_{\rm PQ}\rangle = \frac{f_a}{\sqrt{2}}e^{i\theta_a}, \tag{B1}$$

where f_a is the axion decay constant and θ_a is the phase. Quantum fluctuations during inflation generate fluctuations in the phase, $\delta\theta_a$, as

$$\delta\theta_a = \frac{H}{2\pi f_a}. \tag{B2}$$

As the number density of axions scales as the phase squared, $n_a \propto \theta_a^2$, the mass density fluctuation is given by

$$\frac{\delta\rho_a}{\rho_a} = 2\frac{\delta\theta_a}{\theta_a} = \frac{H}{\pi\theta_a f_a}. \tag{B3}$$

As the energy density of axions was negligible during inflation, the axion density perturbation, $\delta\rho_a/\rho_a$, would produce the isocurvature perturbation. While radiation (including photons) is generated by decay of inflaton fields, (some of) dark matter is in the form of axions whose generation is independent of photons; thus, the entropy perturbation between photons and axions would be generated. We assume that axions were not in thermal equilibrium with photons in the subsequent evolution of the universe.

The entropy perturbations and curvature perturbations are given, respectively, by

$$\frac{k^3P_{\mathcal{S}}(k)}{2\pi^2} = \frac{\Omega_a^2}{\Omega_c^2}\frac{H_k^2}{\pi^2\theta_a^2 f_a^2},\quad \frac{k^3P_{\mathcal{R}}(k)}{2\pi^2} = \frac{H_k^4}{4\pi^2\dot{\phi}_k^2} \approx \frac{H_k^2}{8\pi^2M_{\rm pl}^2\epsilon}, \tag{B4}$$

where $\Omega_a \leqslant \Omega_c$ is the axion mass density, H_k is the expansion rate during inflation at which the wavenumber k went outside of the horizon, ϕ_k is the value of inflaton at the same time, $\epsilon \equiv -\dot{H}/H \approx \left(M_{\rm pl}^2/2\right)(V'/V)^2$ is the usual slow-roll parameter, $V(\phi)$ is the inflaton potential, and $M_{\rm pl} = 1/\sqrt{8\pi G}$ is the reduced Planck mass. We have used the slow-roll approximation, $\dot{\phi} \approx -V'/(3H)$ and $H^2 \approx V\left/\left(3M_{\rm pl}^2\right)\right.$.

Here, let us comment on our choice of $m = 1$, which makes $k^3P_{\mathcal{S}} \propto k^{m-1}$ independent of k. Since $k^3P_{\mathcal{S}} \propto H_k^2 \propto k^{-2\epsilon}$, where $\epsilon = -\dot{H}/H^2$, this choice corresponds to having a very

[52] Note that Smith & Zaldarriaga (2006) used 10^{-6} as a criterion, which gives more quadrature points to evaluate. We find that 10^{-5} is sufficient for the size of statistical and systematic errors in the current measurements.

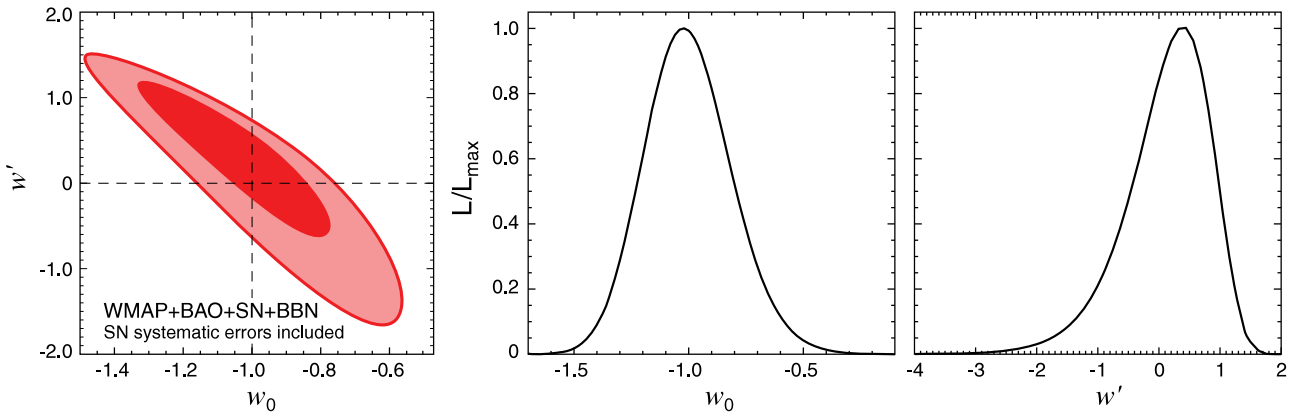

Figure 21. The same as Figure 15, but the systematic errors in the Type Ia SN data are included.

small slow-roll parameter, $\epsilon \ll 1$. This is consistent with our limit on the curvature power spectrum, $n_s = 1 + 6\epsilon - 4\eta \simeq 1 - 4\eta < 1$, where η is another slow-roll parameter. As the current limit is $1 - n_s \approx 4\eta \simeq 0.04$, our approximation, $m = 1$, is valid for $\epsilon < 0.01$. It should be straightforward to extend our analysis to the case in which $m \neq 1$.

By dividing $P_{\mathcal{S}}(k)$ by $P_{\mathcal{R}}(k)$, we find the entropy-to-curvature perturbation ratio for axions, $\alpha_0(k)$, as

$$\frac{\alpha_0(k)}{1-\alpha_0(k)} \equiv \frac{P_{\mathcal{S}}(k)}{P_{\mathcal{R}}(k)} = \frac{\Omega_a^2}{\Omega_c^2}\frac{8\epsilon}{\theta_a^2 (f_a/M_{\rm pl})^2}. \quad \text{(B5)}$$

At this point, it is clear that one cannot solve this constraint uniquely for any of ϵ, f_a, or θ_a.

In order to break the degeneracy, we use the axion mass density (Kawasaki & Sekiguchi 2008, and references therein)

$$\Omega_a h^2 = 1.0 \times 10^{-3} \gamma \theta_a^2 \left(\frac{f_a}{10^{10}\,{\rm GeV}}\right)^{7/6}, \quad \text{(B6)}$$

where γ is a dilution factor, representing the amount by which the axion density could have been diluted by a late-time entropy production between the QCD phase transition at ~ 200 MeV and the epoch of nucleosynthesis at ~ 1 Mpc.

Combining equation (B5) and (B6) to eliminate the phase, θ_a, and using the relation between the tensor-to-scalar ratio r and the slow-roll parameter ϵ, $r = 16\epsilon$, we find

$$r = (1.6 \times 10^{-12}) \left(\frac{\Omega_c h^2}{\gamma}\right) \left(\frac{\Omega_c}{\Omega_a}\right) \left(\frac{f_a}{10^{12}\,{\rm GeV}}\right)^{5/6} \frac{\alpha_0}{1-\alpha_0}. \quad \text{(B7)}$$

Alternatively, we can eliminate the axion decay constant, f_a, to obtain

$$r = \frac{4.7 \times 10^{-12}}{\theta_a^{10/7}} \left(\frac{\Omega_c h^2}{\gamma}\right)^{12/7} \left(\frac{\Omega_c}{\Omega_a}\right)^{2/7} \frac{\alpha_0}{1-\alpha_0}. \quad \text{(B8)}$$

This is Equation (48).

APPENDIX C

EQUATION OF STATE OF DARK ENERGY: A NEW PARAMETRIZED FORM

In this Appendix, we describe the models of dark energy that we explore in Section 5.4. Our goal is to obtain a sensible form of time-dependent dark energy equation of state, $w(a)$. One of the most commonly used form of $w(a)$ is a linear form (Chevallier & Polarski 2001; Linder 2003)

$$w(a) = w_0 + (1-a)w_a, \quad \text{(C1)}$$

where w_0 and w_a parametrize the present-day value of w and the first derivative. However, this form cannot be adopted as it is when one uses the CMB data to constrain $w(a)$. Since this form is basically the leading-order term of a Taylor series expansion, the value of $w(a)$ can become unreasonably too large or too small when extrapolated to the decoupling epoch at $z_* \simeq 1090$ (or $a_* \simeq 9.17 \times 10^{-4}$), and thus one cannot extract meaningful constraints on the quantities, such as w_0 and w_a, that are defined at the *present epoch*.

To avoid this problem, yet to keep a close contact with the previous work in the literature, we shall consider an alternative parametrized form. Our idea is the following: we wish to keep the form given by Equation (C1) at low redshifts, lower than some transition redshift, $z_{\rm trans}$. However, we demand that $w(a)$ approach -1 at higher redshifts, $z > z_{\rm trans}$. This form of $w(a)$, therefore, has the following property: at early times, before the transition redshift, $z_{\rm trans}$, dark energy was just like a cosmological constant, and thus the dark energy density was nearly constant, that is, $\rho_{\rm de}(z > z_{\rm trans}) \approx$ constant. Then, dark energy began to become dynamical at $z \sim z_{\rm trans}$, with the equation of state given by the conventional linear form, Equation (C1).

Some of the properties of our form of $w(a)$ are similar to those of "thawing models," (Caldwell & Linder 2005) in which a scalar field was moving very slowly initially, giving $w(a) \approx -1$ at early times, and then began to move faster toward low redshifts, causing $w(a)$ to deviate more and more from -1 at low redshifts. Our parametrization can describe a more general class of models than single scalar field models, as it allows for w to go below -1. However, models that are based upon a single scalar field cannot have $w < -1$ (e.g., Hu 2005). The "Forever regular" parametrization, explored in Wang & Tegmark (2004), also approaches a constant density at early times, if the late-time equation of state is $w < -1$. The "Kink model" explored in Bassett et al. (2002, 2004) and Corasaniti et al. (2004) also extrapolates a constant equation of state at early times to a different constant equation of state at late times. Our parametrization is more general than theirs, as their form only allows for a constant equation of state at late times.

We wish to find a smooth interpolation between $w_{\rm early} = -1$ and $w_{\rm late} = w_0 + (1-a)w_a$. We begin by writing

$$w(a) = \tilde{w}(a) f(a/a_{\rm trans}) + (-1)\,[1 - f(a/a_{\rm trans})], \quad \text{(C2)}$$

Table 14
Comparison of ΛCDM Parameters from *WMAP*+BAO+SN with Various SN Compilations

Class	Parameter	Union[a]	Union+Sys. Err.[b]	Davis[c]	Alternative[d]
Primary	$100\Omega_b h^2$	$2.267^{+0.058}_{-0.059}$	2.267 ± 0.059	2.270 ± 0.060	2.265 ± 0.059
	$\Omega_c h^2$	0.1131 ± 0.0034	$0.1134^{+0.0036}_{-0.0037}$	0.1121 ± 0.0035	0.1143 ± 0.0034
	Ω_Λ	0.726 ± 0.015	0.725 ± 0.016	$0.732^{+0.014}_{-0.015}$	0.721 ± 0.015
	n_s	0.960 ± 0.013	0.960 ± 0.013	0.962 ± 0.013	$0.960^{+0.014}_{-0.013}$
	τ	0.084 ± 0.016	0.085 ± 0.016	0.085 ± 0.016	0.084 ± 0.016
	$\Delta^2_{\mathcal{R}}(k_0^e)$	$(2.445 \pm 0.096) \times 10^{-9}$	$(2.447^{+0.096}_{-0.095}) \times 10^{-9}$	$(2.429^{+0.096}_{-0.095}) \times 10^{-9}$	$(2.457^{+0.092}_{-0.093}) \times 10^{-9}$
Derived	σ_8	0.812 ± 0.026	$0.813^{+0.026}_{-0.027}$	0.807 ± 0.027	0.817 ± 0.026
	H_0	70.5 ± 1.3 km s^{-1} Mpc^{-1}	70.4 ± 1.4 km s^{-1} Mpc^{-1}	70.9 ± 1.3 km s^{-1} Mpc^{-1}	70.1 ± 1.3 km s^{-1} Mpc^{-1}
	Ω_b	0.0456 ± 0.0015	0.0458 ± 0.0016	$0.0451^{+0.0016}_{-0.0015}$	0.0462 ± 0.0015
	Ω_c	0.228 ± 0.013	$0.229^{+0.014}_{-0.015}$	0.223 ± 0.013	0.233 ± 0.013
	$\Omega_m h^2$	$0.1358^{+0.0037}_{-0.0036}$	$0.1361^{+0.0038}_{-0.0039}$	0.1348 ± 0.0038	0.1369 ± 0.0037
	$z^f_{\rm reion}$	10.9 ± 1.4	10.9 ± 1.4	10.9 ± 1.4	10.8 ± 1.4
	t_0^g	13.72 ± 0.12 Gyr	13.72 ± 0.12 Gyr	13.71 ± 0.12 Gyr	13.73 ± 0.12 Gyr

Notes.
[a] Compilation by Kowalski et al. (2008) *without* the systematic errors included.
[b] Compilation by Kowalski et al. (2008) *with* the systematic errors included.
[c] Compilation by Davis et al. (2007).
[d] Compilation used in the original version of this paper (version 1 of arXiv:0803.0547).
[e] $k_0 = 0.002\,\mathrm{Mpc}^{-1}$. $\Delta^2_{\mathcal{R}}(k) = k^3 P_{\mathcal{R}}(k)/(2\pi^2)$ (Equation (15)).
[f] "Redshift of reionization," if the universe was reionized instantaneously from the neutral state to the fully ionized state at $z_{\rm reion}$.
[g] The present-day age of the universe.

where $a_{\rm trans} = 1/(1+z_{\rm trans})$, and the function $f(x)$ goes to zero for $x \ll 1$ and to unity for $x \gg 1$. Here, $\tilde{w}(a)$ is the form of w at low redshifts. Any function that has this property is adequate for $f(x)$. We choose

$$f(x) = \tfrac{1}{2}\,[\tanh(\ln x) + 1] = \frac{x}{x+1}, \tag{C3}$$

which gives the desired form of the equation of state of dark energy,

$$w(a) = \frac{a\tilde{w}(a)}{a + a_{\rm trans}} - \frac{a_{\rm trans}}{a + a_{\rm trans}}, \tag{C4}$$

where

$$\tilde{w}(a) = \tilde{w}_0 + (1-a)\tilde{w}_a. \tag{C5}$$

One nice property of this form is that it allows one to obtain a closed, analytical form of the effective equation of state, $w_{\rm eff}(a)$, which gives the evolution of dark energy density, $\rho_{\rm de}(a) = \rho(0)a^{-3[1+w_{\rm eff}(a)]}$:

$$\begin{aligned} w_{\rm eff}(a) &= \frac{1}{\ln a}\int_0^{\ln a} d\ln a'\, w(a') \\ &= -1 + \frac{(1-a)\tilde{w}_a}{\ln a} + \frac{1+\tilde{w}_0 + (1+a_{\rm trans})\tilde{w}_a}{\ln a} \\ &\quad \times \ln\frac{a + a_{\rm trans}}{1 + a_{\rm trans}}. \end{aligned} \tag{C6}$$

This property allows one to compute the expansion rate, $H(a)$ (Equation (7)), and hence the distance (Equation (2)), easily.

Finally, we use the present-day value of w, $w_0 \equiv w(z=0)$, and the first derivative, $w' \equiv dw/dz|_{z=0}$, as free parameters. They are related to $\tilde{w}_0$ and $\tilde{w}_a$ as

$$1 + w_0 = \frac{1+\tilde{w}_0}{1+a_{\rm trans}}, \tag{C7}$$

$$w' = \frac{\tilde{w}_a}{1+a_{\rm trans}} - \frac{a_{\rm trans}(1+\tilde{w}_0)}{(1+a_{\rm trans})^2}. \tag{C8}$$

The inverse relations are

$$1 + \tilde{w}_0 = (1+a_{\rm trans})(1+w_0), \tag{C9}$$

$$\tilde{w}_a = (1+a_{\rm trans})w' + a_{\rm trans}(1+w_0). \tag{C10}$$

In the limit of very early transition, $a_{\rm trans} \ll 1$, one finds $w_0 \approx \tilde{w}_0$ and $w' \approx \tilde{w}_a$, as expected. This completes the description of our form of $w(a)$.

Figure 20 shows the evolution of dark energy density, $\rho_{\rm de}(z) = \rho(0)(1+z)^{3[1+w_{\rm eff}(a)]}$, the equation of state, $w(z)$, and the effective equation of state, $w_{\rm eff}(z)$, computed from Equation (C4) and (C6). We choose $w_0 = -1.1$ and $w' = 1$, which are close to the best-fitting values that we found in Section 5.4 (see Figure 14). We show three curves for the transition redshifts of $z_{\rm trans} = 0.5$, 2, and 10. We find that the form of $w(z)$ that we have derived achieves our goal: $w(z)$ approaches -1 and the dark energy density tends to a constant value at high redshifts, giving sensible results at the decoupling epoch. The dark energy density is totally subdominant compared to the matter density at high redshifts, which is also desirable.

The constraints that we have obtained for w_0 and w' are not sensitive to the exact values of $z_{\rm trans}$ (see the right panel of Figure 14). This is because all of the curves shown in Figure 20 are very similar at $z \lesssim 1$, where the BAO and SN data are currently available.

APPENDIX D

COMPARISON OF SN COMPILATIONS AND EFFECTS OF SYSTEMATIC ERRORS

In Table 14, we show the ΛCDM parameters derived from *WMAP*+BAO+SN, where we use various SN compilations: "Union" for the latest union compilation (Kowalski et al. 2008), "Union+Sys.Err." for the union compilation with systematic errors included, "Davis" for the previous compilation by Davis et al. (2007), and "Alternative" for the compilation that we used in the original version of this paper (version 1 of arXiv:0803.0547).

For the "Alternative" compilation, we have combined measurements from the *Hubble Space Telescope* (*HST*; Riess et al. 2004, 2007), the SNLS (Astier et al. 2006), and the Equation of State: ESSENCE survey (Wood-Vasey et al. 2007), as well as some nearby Type Ia SNe. In the "Davis" and "Alternative" compilations, different light curve fitters were used for the SN data taken by different groups, and thus these compilations were not as optimal as the union compilation, for which the same SALT fitter was used for all the SNe samples. Moreover, the union compilation is the largest of all. For this reason, we have decided to update all the cosmological parameters using the union compilation.

Nevertheless, we find that all of these compilations yield similar results: the mean values shift no more than $\sim 0.5\sigma$.

The effects of the systematic errors in the Type Ia SN data on the ΛCDM parameters are also very small for *WMAP*+BAO+SN; however, the effects on the dark energy parameters, w_0 and w', turn out to be significant. In Figure 21, we show the two-dimensional joint constraint on w_0 and w' from *WMAP*+BAO+SN+BBN (also see Section 5.4.2) with the systematic errors included. Comparing this with Figure 15, where the systematic errors are ignored, we find that the constraints on w_0 and w' weaken significantly: we find $w_0 = -1.00 \pm 0.19$ and $w' = 0.11 \pm 0.70$ with the systematic errors included, whereas $w_0 = -1.04 \pm 0.13$ and $w' = 0.24 \pm 0.55$ without the systematic errors.

REFERENCES

Abbott, L. F., & Wise, M. B. 1984, Nucl. Phys. B, 244, 541
Abdalla, F. B., & Rawlings, S. 2007, MNRAS, 381, 1313
Abdurashitov, J. N., et al. 1999, Phys. Rev., C60, 055801
Accetta, F. S., Zoller, D. J., & Turner, M. S. 1985, Phys. Rev. D, 31, 3046
Acquaviva, V., Bartolo, N., Matarrese, S., & Riotto, A. 2003, Nucl. Phys. B, 667, 119
Adam, C., & Klinkhamer, F. R. 2001, Nucl. Phys. B, 607, 247
Adams, F. C., Bond, J. R., Freese, K., Frieman, J. A., & Olinto, A. V. 1993, Phys. Rev. D, 47, 426
Ahmad, Q. R., et al. 2002, Phys. Rev. Lett., 89, 011301
Ahmed, S. N., et al. 2004, Phys. Rev. Lett., 92, 181301
Ahn, M. H., et al. 2003, Phys. Rev. Lett., 90, 041801
Alabidi, L., & Lyth, D. H. 2006a, J. Cosmol. Astropart. Phys., JCAP08(2006)013
Alabidi, L., & Lyth, D. H. 2006b, J. Cosmol. Astropart. Phys., JCAP05(2006)016
Albrecht, A., & Steinhardt, P. J. 1982, Phys. Rev. Lett., 48, 1220
Alishahiha, M., Silverstein, E., & Tong, D. 2004, Phys. Rev. D, 70, 123505
Allen, S. W., Schmidt, R. W., & Bridle, S. L. 2003, MNRAS, 346, 593
Allison, W. W. M., et al. 1999, Phys. Lett. B, 449, 137
Amarzguioui, M., Elgarøy, Ø., Mota, D. F., & Multamäki, T. 2006, A&A, 454, 707
Ambrosio, M., et al. 2001, Phys. Lett. B, 517, 59
Amin, M. A., Wagoner, R. V., & Blandford, R. D. 2008, MNRAS, 390, 131
Araki, T., et al. 2005, Phys. Rev. Lett., 94, 081801
Argüeso, F., González-Nuevo, J., & Toffolatti, L. 2003, ApJ, 598, 86
Arkani-Hamed, N., Creminelli, P., Mukohyama, S., & Zaldarriaga, M. 2004, J. Cosmol. Astropart. Phys., JCAP04(2004)001
Armendariz-Picon, C., Damour, T., & Mukhanov, V. F. 1999, Phys. Lett. B, 458, 209
Arroja, F., & Koyama, K. 2008, Phys. Rev. D, 77, 083517
Astier, P., et al. 2006, A&A, 447, 31
Babich, D. 2005, Phys. Rev. D, 72, 043003
Babich, D., Creminelli, P., & Zaldarriaga, M. 2004, J. Cosmol. Astropart. Phys., JCAP08(2004)009
Bardeen, J. M., Steinhardt, P. J., & Turner, M. S. 1983, Phys. Rev. D, 28, 679
Barger, V., Kneller, J. P., Lee, H.-S., Marfatia, D., & Steigman, G. 2003, Phys. Lett. B, 566, 8
Barger, V., Marfatia, D., & Tregre, A. 2004, Phys. Lett. B, 595, 55
Barris, B. J., et al. 2004, ApJ, 602, 571
Bartolo, N., Komatsu, E., Matarrese, S., & Riotto, A. 2004, Phys. Rep., 402, 103
Bartolo, N., & Liddle, A. R. 2002, Phys. Rev. D, 65, 121301
Bartolo, N., Matarrese, S., & Riotto, A. 2006, J. Cosmol. Astropart. Phys., JCAP06(2006)024
Bartolo, N., Matarrese, S., & Riotto, A. 2007, J. Cosmol. Astropart. Phys., JCAP01(2007)019
Bashinsky, S., & Seljak, U. 2004, Phys. Rev. D, 69, 083002
Basko, M. M., & Polnarev, A. G. 1980, MNRAS, 191, 207
Bassett, B. A., Corasaniti, P. S., & Kunz, M. 2004, ApJ, 617, L1
Bassett, B. A., Kunz, M., Silk, J., & Ungarelli, C. 2002, MNRAS, 336, 1217
Bassett, B. A., Tsujikawa, S., & Wands, D. 2006, Rev. Mod. Phys., 78, 537
Bean, R., Bernat, D., Pogosian, L., Silvestri, A., & Trodden, M. 2007b, Phys. Rev. D, 75, 064020
Bean, R., Chen, X., Peiris, H. V., & Xu, J. 2008, Phys. Rev. D, 77, 023527
Bean, R., Dunkley, J., & Pierpaoli, E. 2006, Phys. Rev. D, 74, 063503
Bean, R., Shandera, S. E., Henry Tye, S. H., & Xu, J. 2007a, J. Cosmol. Astropart. Phys., JCAP07(2005)004
Beltrán, M. 2008, Phys. Rev. D, 78, 023530
Beltrán, M., Garcia-Bellido, J., & Lesgourgues, J. 2007, Phys. Rev. D, 75, 103507
Beltrán, M., García-Bellido, J., Lesgourgues, J., Liddle, A. R., & Slosar, A. 2005a, Phys. Rev. D, 71, 063532
Beltrán, M., Garcia-Bellido, J., Lesgourgues, J., & Riazuelo, A. 2004, Phys. Rev. D, 70, 103530
Beltrán, M., Garcia-Bellido, J., Lesgourgues, J., & Viel, M. 2005b, Phys. Rev. D, 72, 103515
Bennett, C. L., et al. 1994, ApJ, 436, 423
Bennett, C. L., et al. 1996, ApJ, 464, L1
Bennett, C. L., et al. 2003a, ApJ, 583, 1
Bennett, C. L., et al. 2003b, ApJS, 148, 1
Bennett, C. L., et al. 2003c, ApJS, 148, 97
Bernui, A., Mota, B., Rebouças, M. J., & Tavakol, R. 2007, A&A, 464, 479
Bertschinger, E., & Zukin, P. 2008, Phys. Rev. D, 78, 024015
Bielewicz, P., Eriksen, H. K., Banday, A. J., Górski, K. M., & Lilje, P. B. 2005, ApJ, 635, 750
Bolton, J. S., Viel, M., Kim, T.-S., Haehnelt, M. G., & Carswell, R. F. 2008, MNRAS, 386, 1131
Bond, J. R., & Efstathiou, G. 1984, ApJ, 285, L45
Bond, J. R., Efstathiou, G., & Silk, J. 1980, Phys. Rev. Lett., 45, 1980
Bond, J. R., Efstathiou, G., & Tegmark, M. 1997, MNRAS, 291, L33
Bond, J. R., & Szalay, A. S. 1983, ApJ, 274, 443
Boubekeur, L., & Lyth, D. H. 2006, Phys. Rev. D, 73, 021301
Bridges, M., McEwen, J. D., Cruz, M., Hobson, M. P., Lasenby, A. N., Vielva, P., & Martinez-Gonzalez, E. 2008, MNRAS, 390, 1372
Bridle, S. L., Lewis, A. M., Weller, J., & Efstathiou, G. 2003, MNRAS, 342, L72
Buchbinder, E. I., Khoury, J., & Ovrut, B. A. 2007, Phys. Rev. D, 76, 123503
Buchbinder, E. I., Khoury, J., & Ovrut, B. A. 2008, Phys. Rev. Lett., 100, 171302
Bucher, M., Dunkley, J., Ferreira, P. G., Moodley, K., & Skordis, C. 2004, Phys. Rev. Lett., 93, 081301
Byrnes, C. T., Sasaki, M., & Wands, D. 2006, Phys. Rev. D, 74, 123519
Cabella, P., Hansen, F., Marinucci, D., Pagano, D., & Vittorio, N. 2004, Phys. Rev. D, 69, 063007
Cabella, P., Hansen, F. K., Liguori, M., Marinucci, D., Matarrese, S., Moscardini, L., & Vittorio, N. 2006, MNRAS, 369, 819
Cabella, P., Natoli, P., & Silk, J. 2007, Phys. Rev. D, 76, 123014
Caldwell, R. R., Dave, R., & Steinhardt, P. J. 1998, Phys. Rev. Lett., 80, 1582
Caldwell, R. R., & Linder, E. V. 2005, Phys. Rev. Lett., 95, 141301
Carroll, S. M. 1998, Phys. Rev. Lett., 81, 3067
Carroll, S. M., Field, G. B., & Jackiw, R. 1990, Phys. Rev. D, 41, 1231
Carroll, S. M., Press, W. H., & Turner, E. L. 1992, ARA&A, 30, 499
Cash, W. 1976, A&A, 52, 307
Cayón, L., Jin, J., & Treaster, A. 2005, MNRAS, 362, 826
Chambers, A., & Rajantie, A. 2008, Phys. Rev. Lett., 100, 041302
Chen, G., & Szapudi, I. 2005, ApJ, 635, 743
Chen, G., & Szapudi, I. 2006, ApJ, 647, L87
Chen, X. 2005a, J. High Energy Phys., JHEP08(2005)045
Chen, X. 2005b, Phys. Rev. D, 71, 063506
Chen, X., Easther, R., & Lim, E. A. 2007a, J. Cosmol. Astropart. Phys., JCAP06(2007)023
Chen, X., Easther, R., & Lim, E. A. 2008, J. Cosmol. Astropart. Phys., JCAP04(2008)010
Chen, X., Huang, M.-X., Kachru, S., & Shiu, G. 2007b, J. Cosmol. Astropart. Phys., JCAP01(2007)002
Cheung, C., Creminelli, P., Fitzpatrick, A. L., Kaplan, J., & Senatore, L. 2008, J. High Energy Phys., JHEP03(2008)014
Chevallier, M., & Polarski, D. 2001, Int. J. Mod. Phys. D, 10, 213

Chiang, L., Naselsky, P. D., Verkhodanov, O. V., & Way, M. J. 2003, ApJ, 590, L65
Chiang, L.-Y., Naselsky, P. D., & Coles, P. 2007, ApJ, 664, 8
Chiba, T., Sugiyama, N., & Nakamura, T. 1997, MNRAS, 289, L5
Chiba, T., & Takahashi, R. 2007, Phys. Rev. D, 75, 101301
Chu, M., Eriksen, H. K., Knox, L., Górski, K. M., Jewell, J. B., Larson, D. L., O'Dwyer, I. J., & Wandelt, B. D. 2005, Phys. Rev. D, 71, 103002
Cirelli, M., & Strumia, A. 2006, J. Cosmol. Astropart. Phys., JCAP12(2006)013
Cleveland, B. T., et al. 1998, ApJ, 496, 505
Cole, S., et al. 2005, MNRAS, 362, 505
Copeland, E. J., Liddle, A. R., & Wands, D. 1998, Phys. Rev. D, 57, 4686
Copeland, E. J., Sami, M., & Tsujikawa, S. 2006, Int. J. Mod. Phys.D, 15, 1753
Copi, C. J., Huterer, D., Schwarz, D. J., & Starkman, G. D. 2006, MNRAS, 367, 79
Copi, C. J., Huterer, D., Schwarz, D. J., & Starkman, G. D. 2007, Phys. Rev. D, 75, 023507
Copi, C. J., Huterer, D., & Starkman, G. D. 2004, Phys. Rev. D, 70, 043515
Corasaniti, P. S., Kunz, M., Parkinson, D., Copeland, E. J., & Bassett, B. A. 2004, Phys. Rev. D, 70, 083006
Corasaniti, P. S., & Melchiorri, A. 2008, Phys. Rev. D, 77, 103507
Coughlan, G. D., Fischler, W., Kolb, E. W., Raby, S., & Ross, G. G. 1983, Phys. Lett. B, 131, 59
Coulson, D., Crittenden, R. G., & Turok, N. G. 1994, Phys. Rev. Lett., 73, 2390
Covi, L., Hamann, J., Melchiorri, A., Slosar, A., & Sorbera, I. 2006, Phys. Rev. D, 74, 083509
Creminelli, P., Nicolis, A., Senatore, L., Tegmark, M., & Zaldarriaga, M. 2006, J. Cosmol. Astropart. Phys., JCAP05(2006)004
Creminelli, P., & Senatore, L. 2007, J. Cosmol. Astropart. Phys., JCAP11(2007)010
Creminelli, P., Senatore, L., Zaldarriaga, M., & Tegmark, M. 2007, J. Cosmol. Astropart. Phys., JCAP03(2007)005
Crittenden, R., Bond, J. R., Davis, R. L., Efstathiou, G., & Steinhardt, P. J. 1993, Phys. Rev. Lett., 71, 324
Crittenden, R., Davis, R. L., & Steinhardt, P. J. 1993, ApJ, 417, L13
Crittenden, R. G., Coulson, D., & Turok, N. G. 1995, Phys. Rev. D, 52, 5402
Crotty, P., Garcia-Bellido, J., Lesgourgues, J., & Riazuelo, A. 2003a, Phys. Rev. Lett., 91, 171301
Crotty, P., Lesgourgues, J., & Pastor, S. 2003b, Phys. Rev. D, 67, 123005
Crotty, P., Lesgourgues, J., & Pastor, S. 2004, Phys. Rev. D, 69, 123007
Cruz, M., Cayón, L., Martínez-González, E., Vielva, P., & Jin, J. 2007a, ApJ, 655, 11
Cruz, M., Martínez-González, E., Vielva, P., & Cayón, L. 2005, MNRAS, 356, 29
Cruz, M., Tucci, M., Martínez-González, E., & Vielva, P. 2006, MNRAS, 369, 57
Cruz, M., Turok, N., Vielva, P., Martínez-González, E., & Hobson, M. 2007b, Science, 318, 1612
Curto, A., Aumont, J., Macías-Pérez, J. F., Martínez-González, E., Barreiro, R. B., Santos, D., Désert, F. X., & Tristram, M. 2007, A&A, 474, 23
Daniel, S. F., Caldwell, R. R., Cooray, A., & Melchiorri, A. 2008, Phys. Rev. D, 77, 103513
Davis, J., Raymond, , Harmer, D. S., & Hoffman, K. C. 1968, Phys. Rev. Lett., 20, 1205
Davis, T. M., et al. 2007, ApJ, 666, 716
de Bernardis, F., Melchiorri, A., Verde, L., & Jimenez, R. 2008, J. Cosmol. Astropart. Phys., JCAP03(2008)020
de Bernardis, P., et al. 2000, Nature, 404, 955
de Oliveira-Costa, A., Tegmark, M., Zaldarriaga, M., & Hamilton, A. 2004, Phys. Rev. D, 69, 063516
De Troia, G., et al. 2007, ApJ, 670, L73
Deffayet, C., Dvali, G., & Gabadadze, G. 2002, Phys. Rev. D, 65, 44023
Destri, C., de Vega, H. J., & Sanchez, N. G. 2008, Phys. Rev. D, 77, 043509
Dickinson, C., et al. 2004, MNRAS, 353, 732
Dicus, D. A., et al. 1982, Phys. Rev. D, 26, 2694
Dimopoulos, S., Kachru, S., McGreevy, J., & Wacker, J. 2005, arXiv:hep-th/0507205
Dodelson, S., Kinney, W. H., & Kolb, E. W. 1997, Phys. Rev. D, 56, 3207
Dolgov, A. D. 2002, Phys. Rep., 370, 333
Dolgov, A. D., Hansen, S. H., & Semikoz, D. V. 1999, Nucl. Phys. B, 543, 269
Doré, O., et al. 2007, arXiv:0712.1599
Dunkley, J., Bucher, M., Ferreira, P. G., Moodley, K., & Skordis, C. 2005, Phys. Rev. Lett., 95, 261303
Dunkley, J., et al. 2008, arXiv:0811.4280
Dunkley, J., et al. 2009, ApJS, 180, 306
Dvali, G., Gruzinov, A., & Zaldarriaga, M. 2004a, Phys. Rev. D, 69, 083505
Dvali, G., Gruzinov, A., & Zaldarriaga, M. 2004b, Phys. Rev. D, 69, 023505
Dvali, G. R., Gabadadze, G., & Porrati, M. 2000, Phys. Lett. B, 485, 208
Dvali, G. R., Shafi, Q., & Schaefer, R. 1994, Phys. Rev. Lett., 73, 1886
Easther, R., & McAllister, L. 2006, J. Cosmol. Astropart. Phys., JCAP05(2006)018
Easther, R., & Peiris, H. 2006, J. Cosmol. Astropart. Phys., JCAP09(2006)010
Eguchi, K., et al. 2003, Phys. Rev. Lett., 90, 021802
Eisenstein, D. J., & Hu, W. 1998, ApJ, 496, 605
Eisenstein, D. J., et al. 2005, ApJ, 633, 560
Elgarøy, Ø., & Lahav, O. 2003, J. Cosmol. Astropart. Phys., JCAP04(2003)004
Elgarøy, Ø., & Lahav, O. 2005, New J. Phys., 7, 61
Elgarøy, Ø., & Multamäki, T. 2007, A&A, 471, 65
Ellis, J. R., Nanopoulos, D. V., & Quiros, M. 1986, Phys. Lett., B174, 176
Enqvist, K., Jokinen, A., Mazumdar, A., Multamäki, T., & Väihkönen, A. 2005, Phys. Rev. Lett., 94, 161301
Eriksen, H. K., Banday, A. J., Górski, K. M., Hansen, F. K., & Lilje, P. B. 2007a, ApJ, 660, L81
Eriksen, H. K., Hansen, F. K., Banday, A. J., Górski, K. M., & Lilje, P. B. 2004b, ApJ, 605, 14
Eriksen, H. K., Huey, G., Banday, A. J., Górski, K. M., Jewell, J. B., O'Dwyer, I. J., & Wandelt, B. D. 2007b, ApJ, 665, L1
Eriksen, H. K., Novikov, D. I., Lilje, P. B., Banday, A. J., & Gorski, K. M. 2004c, ApJ, 612, 64
Eriksen, H. K., et al. 2004a, ApJS, 155, 227
Eriksen, H. K., et al. 2007c, ApJ, 656, 641
Fabbri, R., & Pollock, M. D. 1983, Phys. Lett. B, 125, 445
Falk, T., Rangarajan, R., & Srednicki, M. 1993, ApJ, 403, L1
Feng, B., Li, H., Li, M.-Z., & Zhang, X.-M. 2005, Phys. Lett. B, 620, 27
Feng, B., Li, M., Xia, J.-Q., Chen, X., & Zhang, X. 2006, Phys. Rev. Lett., 96, 221302
Ferreira, P. G., & Joyce, M. 1998, Phys. Rev. D, 58, 023503
Ford, L. H. 1987, Phys. Rev. D, 35, 2339
Freedman, W. L., et al. 2001, ApJ, 553, 47
Freese, K., Frieman, J. A., & Olinto, A. V. 1990, Phys. Rev. Lett., 65, 3233
Fu, L., et al. 2008, A&A, 479, 9
Fujii, Y., & Nishioka, T. 1990, Phys. Rev. D, 42, 361
Fukuda, S., et al. 2001a, Phys. Rev. Lett., 86, 5656
Fukuda, S., et al. 2001b, Phys. Rev. Lett., 86, 5651
Fukuda, Y., et al. 1994, Phys. Lett. B, 335, 237
Fukuda, Y., et al. 1998, Phys. Rev. Lett., 81, 1562
Fukugita, M. 2006, Nucl. Phys. Proc. Suppl., 155, 10
Futamase, T., & Maeda, K. I. 1989, Phys. Rev. D, 39, 399
Gangui, A., Lucchin, F., Matarrese, S., & Mollerach, S. 1994, ApJ, 430, 447
Garriga, J., & Mukhanov, V. F. 1999, Phys. Lett. B, 458, 219
Gaztañaga, E., & Wagg, J. 2003, Phys. Rev. D, 68, 021302
Giannantonio, T., Scranton, R., Crittenden, R. G., Nichol, R. C., Boughn, S. P., Myers, A. D., & Richards, G. T. 2008, Phys. Rev. D, 77, 123520
Gnedin, N. Y., & Gnedin, O. Y. 1998, ApJ, 509, 11
Gold, B., et al. 2009, ApJS, 180, 265
Goobar, A., Hannestad, S., Mortsell, E., & Tu, H. 2006, J. Cosmol. Astropart. Phys., JCAP06(2006)019
Gordon, C., Hu, W., Huterer, D., & Crawford, T. 2005, Phys. Rev. D, 72, 103002
Gordon, C., & Lewis, A. 2003, Phys. Rev. D, 67, 123513
Gordon, C., & Malik, K. A. 2004, Phys. Rev. D, 69, 063508
Gordon, C., Wands, D., Bassett, B. A., & Maartens, R. 2001, Phys. Rev. D, 63, 023506
Gorski, K. M., Hivon, E., Banday, A. J., Wandelt, B. D., Hansen, F. K., Reinecke, M., & Bartlemann, M. 2005, ApJ, 622, 759
Gott, J. R., Colley, W. N., Park, C.-G., Park, C., & Mugnolo, C. 2007, MNRAS, 377, 1668
Gott, J. R. I., Park, C., Juszkiewicz, R., Bies, W. E., Bennett, D. P., Bouchet, F. R., & Stebbins, A. 1990, ApJ, 352, 1
Grishchuk, L. P. 1975, Sov. Phys.—JETP, 40, 409
Grivell, I. J., & Liddle, A. R. 2000, Phys. Rev. D, 61, 081301
Guth, A. H. 1981, Phys. Rev. D, 23, 347
Guth, A. H., & Pi, S. Y. 1982, Phys. Rev. Lett., 49, 1110
Guy, J., Astier, P., Nobili, S., Regnault, N., & Pain, R. 2005, A&A, 443, 781
Hajian, A., & Souradeep, T. 2003, ApJ, 597, L5
Hajian, A., & Souradeep, T. 2006, Phys. Rev. D, 74, 123521
Hajian, A., Souradeep, T., & Cornish, N. 2005, ApJ, 618, L63
Hamann, J., Hannestad, S., Raffelt, G. G., & Wong, Y. Y. Y. 2007, J. Cosmol. Astropart. Phys., JCAP08(2007)021
Hampel, W., et al. 1999, Phys. Lett. B, 447, 127
Hamuy, M., Phillips, M. M., Suntzeff, N. B., Schommer, R. A., Maza, J., & Aviles, R. 1996, AJ, 112, 2391
Hanany, S., et al. 2000, ApJ, 545, L5
Hannestad, S. 2003, J. Cosmol. Astropart. Phys., JCAP05(2003)004
Hannestad, S. 2004, J. Cosmol. Astropart. Phys., JCAP04(2004)002
Hannestad, S. 2005, Phys. Rev. Lett., 95, 221301

Hannestad, S. 2006a, J. Cosmol. Astropart. Phys., JCAP01(2006)001
Hannestad, S. 2006b, Ann. Rev. Nucl. Part. Sci., 56, 137
Hannestad, S., & Raffelt, G. 2004, J. Cosmol. Astropart. Phys., JCAP04(2004)008
Hannestad, S., & Raffelt, G. G. 2006, J. Cosmol. Astropart. Phys., JCAP11(2006)016
Hannestad, S., & Wong, Y. Y. Y. 2007, J. Cosmol. Astropart. Phys., JCAP07(2007)004
Hansen, F. K., Banday, A. J., & Gorski, K. M. 2004a, MNRAS, 354, 641
Hansen, F. K., Cabella, P., Marinucci, D., & Vittorio, N. 2004b, ApJ, 607, L67
Hawking, S. W. 1982, Phys. Lett., B115, 295
Hikage, C., Komatsu, E., & Matsubara, T. 2006, ApJ, 653, 11
Hikage, C., Matsubara, T., Coles, P., Liguori, M., Hansen, F. K., & Matarrese, S. 2008, MNRAS, 389, 1439
Hill, R., et al. 2009, ApJS, 180, 246
Hinshaw, G., et al. 2007, ApJS, 170, 288
Hinshaw, G., et al. 2009, ApJS, 180, 225
Hirata, K. S., et al. 1992, Phys. Lett. B, 280, 146
Ho, S., Hirata, C. M., Padmanabhan, N., Seljak, U., & Bahcall, N. 2008, Phys. Rev. D, 78, 043519
Holman, R., & Tolley, A. J. 2008, J. Cosmol. Astropart. Phys., JCAP05(2008)001
Hu, W. 1998, ApJ, 506, 485
Hu, W. 2005, Phys. Rev. D, 71, 047301
Hu, W. 2008, Phys. Rev. D, 77, 103524
Hu, W., & Eisenstein, D. J. 1998, ApJ, 498, 497
Hu, W., Eisenstein, D. J., & Tegmark, M. 1998, Phys. Rev. Lett., 80, 5255
Hu, W., & Okamoto, T. 2004, Phys. Rev. D, 69, 043004
Hu, W., & Sawicki, I. 2007, Phys. Rev. D, 76, 104043
Hu, W., Scott, D., Sugiyama, N., & White, M. 1995, Phys. Rev. D, 52, 5498
Hu, W., & Sugiyama, N. 1996, ApJ, 471, 542
Huang, M.-X., & Shiu, G. 2006, Phys. Rev. D, 74, 121301
Huffenberger, K. M., Eriksen, H. K., & Hansen, F. K. 2006, ApJ, 651, L81
Hwang, J., & Noh, H. 1998, Phys. Rev. Lett., 81, 5274
Ichikawa, K., Fukugita, M., & Kawasaki, M. 2005, Phys. Rev. D, 71, 043001
Ichikawa, K., Kawasaki, M., & Takahashi, F. 2007, J. Cosmol. Astropart. Phys., JCAP05(2007)007
Ishak, M., Upadhye, A., & Spergel, D. N. 2006, Phys. Rev. D, 74, 043513
Jaffe, T. R., Banday, A. J., Eriksen, H. K., Górski, K. M., & Hansen, F. K. 2005, ApJ, 629, L1
Jaffe, T. R., Banday, A. J., Eriksen, H. K., Górski, K. M., & Hansen, F. K. 2006, A&A, 460, 393
Jain, B., & Zhang, P. 2008, Phys. Rev. D, 78, 063503
Jewell, J., Levin, S., & Anderson, C. H. 2004, ApJ, 609, 1
Jha, S., et al. 2006, AJ, 131, 527
Jokinen, A., & Mazumdar, A. 2006, J. Cosmol. Astropart. Phys., JCAP04(2006)003
Jones, W. C., et al. 2006, ApJ, 647, 823
Kadota, K., Dodelson, S., Hu, W., & Stewart, E. D. 2005, Phys. Rev. D, 72, 023510
Kain, B. 2006, Phys. Rev., D73, 123521
Kalara, S., Kaloper, N., & Olive, K. A. 1990, Nucl. Phys. B, 341, 252
Kallosh, R., Kang, J. U., Linde, A., & Mukhanov, V. 2008, J. Cosmol. Astropart. Phys., JCAP04(2008)018
Kallosh, R., Kofman, L., & Linde, A. D. 2001a, Phys. Rev. D, 64, 123523
Kallosh, R., Kofman, L., Linde, A. D., & Tseytlin, A. A. 2001b, Phys. Rev. D, 64, 123524
Kamionkowski, M., Kosowsky, A., & Stebbins, A. 1997b, Phys. Rev. Lett., 78, 2058
Kamionkowski, M., Kosowsky, A., & Stebbins, A. 1997a, Phys. Rev. D, 55, 7368
Kawasaki, M., & Sekiguchi, T. 2008, Prog. Theor. Phys., 120, 995
Kazanas, D. 1980, ApJ, 241, L59
Keskitalo, R., Kurki-Suonio, H., Muhonen, V., & Valiviita, J. 2007, J. Cosmol. Astropart. Phys., JCAP09(2007)008
Khoury, J., Ovrut, B. A., Seiberg, N., Steinhardt, P. J., & Turok, N. 2002a, Phys. Rev. D, 65, 086007
Khoury, J., Ovrut, B. A., Steinhardt, P. J., & Turok, N. 2001, Phys. Rev. D, 64, 123522
Khoury, J., Ovrut, B. A., Steinhardt, P. J., & Turok, N. 2002b, Phys. Rev. D, 66, 046005
Khoury, J., Steinhardt, P. J., & Turok, N. 2003, Phys. Rev. Lett., 91, 161301
Kim, T.-S., Bolton, J. S., Viel, M., Haehnelt, M. G., & Carswell, R. F. 2007, MNRAS, 382, 1657
Kinney, W. H. 1998, Phys. Rev. D, 58, 123506
Kinney, W. H., Kolb, E. W., Melchiorri, A., & Riotto, A. 2006, Phys. Rev., D74, 023502
Kitching, T. D., Heavens, A. F., Verde, L., Serra, P., & Melchiorri, A. 2008, Phys. Rev. D, 77, 103008
Klinkhamer, F. R. 2000, Nucl. Phys. B, 578, 277
Knop, R. A., et al. 2003, ApJ, 598, 102
Knox, L. 2006, Phys. Rev. D, 73, 023503
Kodama, H., & Sasaki, M. 1984, Prog. Theor. Phys. Suppl., 78, 1
Kofman, L., Blumenthal, G. R., Hodges, H., & Primack, J. R. 1991, in ASP Conf. Ser. 15, Large-Scale Structures and Peculiar Motions in the Universe (San Francisco, CA: ASP), 339
Kogo, N., & Komatsu, E. 2006, Phys. Rev. D, 73, 083007
Kogo, N., Matsumiya, M., Sasaki, M., & Yokoyama, J. 2004, ApJ, 607, 32
Kogo, N., Sasaki, M., & Yokoyama, J. 2005, Prog. Theor. Phys., 114, 555
Kolb, E. W., & Turner, M. S. 1990, The Early Universe (New York: Addison-Wesley)
Komatsu, E. 2001, PhD thesis, Tohoku Univ. (arXiv:astro-ph/0206039)
Komatsu, E., & Futamase, T. 1999, Phys. Rev. D, 59, 064029
Komatsu, E., & Seljak, U. 2002, MNRAS, 336, 1256
Komatsu, E., & Spergel, D. N. 2001, Phys. Rev. D, 63, 63002
Komatsu, E., Spergel, D. N., & Wandelt, B. D. 2005, ApJ, 634, 14
Komatsu, E., Wandelt, B. D., Spergel, D. N., Banday, A. J., & Górski, K. M. 2002, ApJ, 566, 19
Komatsu, E., et al. 2003, ApJS, 148, 119
Kosowsky, A., & Turner, M. S. 1995, Phys. Rev. D, 52, 1739
Kostelecky, A., & Mewes, M. 2007, Phys. Rev. Lett., 99, 011601
Kowalski, M., et al. 2008, ApJ, 686, 749
Koyama, K., & Maartens, R. 2006, J. Cosmol. Astropart. Phys., JCAP01(2006)016
Koyama, K., Mizuno, S., Vernizzi, F., & Wands, D. 2007, J. Cosmol. Astropart. Phys., JCAP11(2007)024
Koyama, K., & Wands, D. 2007, J. Cosmol. Astropart. Phys., JCAP04(2007)008
Krisciunas, K., et al. 2001, AJ, 122, 1616
Krisciunas, K., et al. 2004a, AJ, 127, 1664
Krisciunas, K., et al. 2004b, AJ, 128, 3034
Kuo, C. L., et al. 2004, ApJ, 600, 32
Kuo, C. L., et al. 2007, ApJ, 664, 687
Kurki-Suonio, H., Muhonen, V., & Valiviita, J. 2005, Phys. Rev. D, 71, 063005
La, D., & Steinhardt, P. J. 1989, Phys. Rev. Lett., 62, 376
Land, K., & Magueijo, J. 2005a, MNRAS, 357, 994
Land, K., & Magueijo, J. 2005b, Phys. Rev. Lett., 95, 071301
Land, K., & Magueijo, J. 2007, MNRAS, 378, 153
Langlois, D. 1999, Phys. Rev. D, 59, 123512
Langlois, D., & Riazuelo, A. 2000, Phys. Rev. D, 62, 043504
Larson, D. L., Eriksen, H. K., Wandelt, B. D., Górski, K. M., Huey, G., Jewell, J. B., & O'Dwyer, I. J. 2007, ApJ, 656, 653
Larson, D. L., & Wandelt, B. D. 2004, ApJ, 613, L85
Lattanzi, M., Ruffini, R., & Vereshchagin, G. V. 2005, Phys. Rev. D, 72, 063003
Lazarides, G. 2005, Nucl. Phys. Proc. Suppl., 148, 84
Lazarides, G., de Austri, R. R., & Trotta, R. 2004, Phys. Rev. D, 70, 123527
Lazkoz, R., Nesseris, S., & Perivolaropoulos, L. 2008, J. Cosmol. Astropart. Phys., JCAP07(2008)012
Lee, T. D., & Yang, C.-N. 1956, Phys. Rev., 104, 254
Lehners, J.-L., & Steinhardt, P. J. 2008a, Phys. Rev. D, 78, 023506
Lehners, J.-L., & Steinhardt, P. J. 2008b, Phys. Rev. D, 77, 063533
Lepora, N. F. 1998, arXiv:gr-gc 9812077
Lesgourgues, J., & Pastor, S. 2006, Phys. Rep., 429, 307
Lesgourgues, J., & Valkenburg, W. 2007, Phys. Rev. D, 75, 123519
Lesgourgues, J., Viel, M., Haehnelt, M. G., & Massey, R. 2007, J. Cosmol. Astropart. Phys., JCAP11(2007)008
Lewis, A., & Challinor, A. 2006, Phys. Rep., 429, 1
Lewis, A., Challinor, A., & Lasenby, A. 2000, ApJ, 538, 473
Li, H., Xia, J.-Q., Zhao, G.-B., Fan, Z.-H., & Zhang, X. 2008a, ApJ, 683, L1
Li, M., Lin, C., Wang, T., & Wang, Y. 2008b, arXiv:0805.1299
Li, M., Wang, T., & Wang, Y. 2008, J. Cosmol. Astropart. Phys., JCAP03(2008)028
Liddle, A. R., & Leach, S. M. 2003, Phys. Rev. D, 68, 103503
Liddle, A. R., & Lyth, D. H. 2000, Cosmological Inflation and Large-Scale Structure (Cambridge: Cambridge Univ. Press)
Liddle, A. R., Mazumdar, A., & Schunck, F. E. 1998, Phys. Rev. D, 58, 061301
Lidsey, J. E., Liddle, A. R., Kolb, E. W., Copeland, E. J., Barreiro, T., & Abney, M. 1997, Rev. Mod. Phys., 69, 373
Liguori, M., Hansen, F. K., Komatsu, E., Matarrese, S., & Riotto, A. 2006, Phys. Rev. D, 73, 043505
Linde, A. 2002, arXiv:hep-th/0211048
Linde, A. 2008, Lect. Notes Phys., 738, 1
Linde, A., & Mukhanov, V. 1997, Phys. Rev. D, 56, 535
Linde, A. D. 1982, Phys. Lett. B, 108, 389
Linde, A. D. 1983, Phys. Lett. B, 129, 177

Linde, A. D. 1985, Phys. Lett. B, 158, 375
Linde, A. D. 1991, Phys. Lett. B, 259, 38
Linde, A. D. 1994, Phys. Rev. D, 49, 748
Linder, E. V. 2003, Phys. Rev. Lett., 90, 091301
Linder, E. V., & Cahn, R. N. 2007, Astropart. Phys., 28, 481
Linder, E. V., & Jenkins, A. 2003, MNRAS, 346, 573
Liu, G.-C., Lee, S., & Ng, K.-W. 2006, Phys. Rev. Lett., 97, 161303
Lorenz, L., Martin, J., & Ringeval, C. 2008, J. Cosmol. Astropart. Phys., JCAP04(2008)001
Lucchin, F., & Matarrese, S. 1985, Phys. Rev. D, 32, 1316
Lue, A., Wang, L., & Kamionkowski, M. 1999, Phys. Rev. Lett., 83, 1506
Lyth, D. H., Malik, K. A., & Sasaki, M. 2005, J. Cosmol. Astropart. Phys., JCAP05(2005)004
Lyth, D. H., & Rodriguez, Y. 2005, Phys. Rev. Lett., 95, 121302
Lyth, D. H., & Stewart, E. D. 1992, Phys. Rev. D, 46, 532
Lyth, D. H., Ungarelli, C., & Wands, D. 2003, Phys. Rev. D, 67, 23503
Lyth, D. H., & Wands, D. 2003, Phys. Rev. D, 68, 103516
Ma, C.-P. 1996, ApJ, 471, 13
Maldacena, J. M. 2003, J. High Energy Phys., JHEP05(2003)013
Mangano, G., Melchiorri, A., Mena, O., Miele, G., & Slosar, A. 2007, J. Cosmol. Astropart. Phys., JCAP03(2007)006
Mangano, G., Miele, G., Pastor, S., & Peloso, M. 2002, Phys. Lett. B, 534, 8
Martin, J., & Ringeval, C. 2006, J. Cosmol. Astropart. Phys., JCAP08(2006)009
Mason, B. S., et al. 2003, ApJ, 591, 540
Matsumiya, M., Sasaki, M., & Yokoyama, J. 2002, Phys. Rev. D, 65, 083007
Matsumiya, M., Sasaki, M., & Yokoyama, J. 2003, J. Cosmol. Astropart. Phys., JCAP02(2003)003
McAllister, L., & Silverstein, E. 2008, Gen. Rel. Grav., 40, 565
Mecke, K. R., Buchert, T., & Wagner, H. 1994, A&A, 288, 697
Melchiorri, A., & Serra, P. 2006, Phys. Rev. D, 74, 127301
Michael, D. G., et al. 2006, Phys. Rev. Lett., 97, 191801
Miller, A. D., et al. 1999, ApJ, 524, L1
Miller, A. D., et al. 2002, ApJS, 140, 115
Miller, N. J., Keating, B. G., & Polnarev, A. G. 2007, arXiv:0710.3651
Mollerach, S., & Matarrese, S. 1997, Phys. Rev. D, 56, 4494
Montroy, T. E., et al. 2006, ApJ, 647, 813
Moodley, K., Bucher, M., Dunkley, J., Ferreira, P. G., & Skordis, C. 2004, Phys. Rev. D, 70, 103520
Moroi, T., & Takahashi, T. 2001, Phys. Lett. B, 522, 215
Moroi, T., & Takahashi, T. 2002, Phys. Rev. D, 66, 063501
Moss, I. G., & Graham, C. M. 2007, J. Cosmol. Astropart. Phys., JCAP11(2007)004
Moss, I. G., & Xiong, C. 2007, J. Cosmol. Astropart. Phys., JCAP04(2007)007
Mukhanov, V. F., & Chibisov, G. V. 1981, JETP Lett., 33, 532
Mukherjee, P., & Wang, Y. 2003a, ApJ, 598, 779
Mukherjee, P., & Wang, Y. 2003b, ApJ, 599, 1
Mukherjee, P., & Wang, Y. 2003c, ApJ, 593, 38
Mukherjee, P., & Wang, Y. 2004, ApJ, 613, 51
Naselsky, P. D., Christensen, P. R., Coles, P., Verkhodanov, O., Novikov, D., & Kim, J. 2007, arXiv:0712.1118
Nesseris, S., & Perivolaropoulos, L. 2008, Phys. Rev. D, 77, 023504
Netterfield, C. B., et al. 2002, ApJ, 571, 604
Nolta, M. R., et al. 2009, ApJS, 180, 296
O'Dwyer, I. J., et al. 2004, ApJ, 617, L99
Okamoto, T., & Hu, W. 2002, Phys. Rev. D, 66, 063008
Okumura, T., Matsubara, T., Eisenstein, D. J., Kayo, I., Hikage, C., Szalay, A. S., & Schneider, D. P. 2008, ApJ, 676, 889
Padmanabhan, T. 2003, Phys. Rep., 380, 235
Padmanabhan, T. 2005, Curr. Sci., 88, 1057
Page, L., et al. 2003, ApJS, 148, 39
Page, L., et al. 2007, ApJS, 170, 335
Pagels, H., & Primack, J. R. 1982, Phys. Rev. Lett., 48, 223
Park, C. 2004, MNRAS, 349, 313
Park, C.-G., Park, C., & Gott, J. R. I. 2007, ApJ, 660, 959
Parkinson, D., Tsujikawa, S., Bassett, B. A., & Amendola, L. 2005, Phys. Rev. D, 71, 063524
Pearson, T. J., et al. 2003, ApJ, 591, 556
Peebles, P. J., & Ratra, B. 2003, Rev. Mod. Phys., 75, 559
Peebles, P. J. E., & Ratra, B. 1988, ApJ, 325, L17
Peiris, H., & Easther, R. 2006a, J. Cosmol. Astropart. Phys., JCAP07(2006)002
Peiris, H., & Easther, R. 2006b, J. Cosmol. Astropart. Phys., JCAP10(2006)017
Peiris, H. V., et al. 2003, ApJS, 148, 213
Percival, W. J., Cole, S., Eisenstein, D. J., Nichol, R. C., Peacock, J. A., Pope, A. C., & Szalay, A. S. 2007, MNRAS, 381, 1053
Perlmutter, S., et al. 1999, ApJ, 517, 565
Pettini, M., Zych, B. J., Murphy, M. T., Lewis, A., & Steidel, C. C. 2008, MNRAS, 391, 1499
Piacentini, F., et al. 2006, ApJ, 647, 833
Piao, Y.-S. 2006, Phys. Rev. D, 74, 047302
Pierpaoli, E. 2003, MNRAS, 342, L63
Polarski, D., & Starobinsky, A. A. 1992, Nucl. Phys. B, 385, 623
Polarski, D., & Starobinsky, A. A. 1994, Phys. Rev. D, 50, 6123
Polnarev, A. G. 1985, AZh, 62, 1041
Polnarev, A. G., Miller, N. J., & Keating, B. G. 2008, MNRAS, 386, 1053
Powell, B. A., & Kinney, W. H. 2007, J. Cosmol. Astropart. Phys., JCAP08(2007)006
Press, W. H., Teukolsky, S. A., Vetterling, W. T., & Flannery, B. P. 1992, Numerical Recipes in C (2nd ed.; Cambridge: Cambridge Univ. Press)
Prunet, S., Uzan, J.-P., Bernardeau, F., & Brunier, T. 2005, Phys. Rev. D, 71, 083508
Pyne, T., & Carroll, S. M. 1996, Phys. Rev. D, 53, 2920
Rakić, A., & Schwarz, D. J. 2007, Phys. Rev. D, 75, 103002
Räth, C., Schuecker, P., & Banday, A. J. 2007, MNRAS, 380, 466
Ratra, B., & Peebles, P. J. E. 1988, Phys. Rev. D, 37, 3406
Readhead, A. C. S., et al. 2004, ApJ, 609, 498
Refregier, A., Spergel, D. N., & Herbig, T. 2000, ApJ, 531, 31
Reichardt, C. L., et al. 2008, arXiv:0801.1491
Riess, A. G., et al. 1998, AJ, 116, 1009
Riess, A. G., et al. 1999, AJ, 117, 707
Riess, A. G., et al. 2004, ApJ, 607, 665
Riess, A. G., et al. 2007, ApJ, 659, 98
Rubakov, V. A., Sazhin, M. V., & Veryaskin, A. V. 1982, Phys. Lett. B, 115, 189
Ruhl, J. E., et al. 2003, ApJ, 599, 786
Sachs, R. K., & Wolfe, A. M. 1967, ApJ, 147, 73
Sahni, V., & Starobinsky, A. A. 2000, Int. J. Mod. Phys.D, 9, 373
Saito, S., Ichiki, K., & Taruya, A. 2007, J. Cosmol. Astropart. Phys., JCAP09(2007)002
Salopek, D. S., & Bond, J. R. 1990, Phys. Rev. D, 42, 3936
Sánchez, A. G., & Cole, S. 2008, MNRAS, 385, 830
Santos, M. G., et al. 2003, MNRAS, 341, 623
Sasaki, M., & Stewart, E. D. 1996, Prog. Theor. Phys., 95, 71
Sato, K. 1981, MNRAS, 195, 467
Savage, C., Freese, K., & Kinney, W. H. 2006, Phys. Rev. D, 74, 123511
Schmalzing, J., & Buchert, T. 1997, ApJ, 482, L1
Schmalzing, J., & Gorski, K. M. 1998, MNRAS, 297, 355
Schwarz, D. J., Starkman, G. D., Huterer, D., & Copi, C. J. 2004, Phys. Rev. Lett., 93, 221301
Sealfon, C., Verde, L., & Jimenez, R. 2005, Phys. Rev. D, 72, 103520
Seckel, D., & Turner, M. S. 1985, Phys. Rev. D, 32, 3178
Seery, D., & Lidsey, J. E. 2005, J. Cosmol. Astropart. Phys., JCAP06(2005)003
Seery, D., & Lidsey, J. E. 2007, J. Cosmol. Astropart. Phys., JCAP01(2007)008
Seery, D., Lidsey, J. E., & Sloth, M. S. 2007, J. Cosmol. Astropart. Phys., JCAP01(2007)027
Seljak, U., Slosar, A., & McDonald, P. 2006, J. Cosmol. Astropart. Phys., JCAP10(2006)014
Seljak, U., & Zaldarriaga, M. 1996, ApJ, 469, 437
Seljak, U., & Zaldarriaga, M. 1997, Phys. Rev. Lett., 78, 2054
Seljak, U., et al. 2005a, Phys. Rev. D, 71, 043511
Seljak, U., et al. 2005b, Phys. Rev. D, 71, 103515
Serra, P., & Cooray, A. 2008, Phys. Rev. D, 77, 107305
Shafi, Q., & Senoguz, V. N. 2006, Phys. Rev. D, 73, 127301
Shafieloo, A., & Souradeep, T. 2004, Phys. Rev. D, 70, 043523
Shafieloo, A., & Souradeep, T. 2008, Phys. Rev. D, 78, 023511
Sievers, J. L., et al. 2003, ApJ, 591, 599
Sievers, J. L., et al. 2007, ApJ, 660, 976
Sikivie, P. 2008, Lect. Notes Phys., 741, 19
Silk, J., & Turner, M. S. 1987, Phys. Rev. D, 35, 419
Silverstein, E., & Tong, D. 2004, Phys. Rev. D, 70, 103505
Slosar, A. 2006, Phys. Rev. D, 73, 123501
Smith, K. M., & Zaldarriaga, M. 2006, arXiv:astro-ph/0612571
Smith, S., et al. 2004, MNRAS, 352, 887
Smoot, G. F., et al. 1992, ApJ, 396, L1
Song, Y.-S., Hu, W., & Sawicki, I. 2007, Phys. Rev. D, 75, 044004
Spergel, D. N., & Zaldarriaga, M. 1997, Phys. Rev. Lett., 79, 2180
Spergel, D. N., et al. 2003, ApJS, 148, 175
Spergel, D. N., et al. 2007, ApJS, 170, 377
Starobinsky, A. A. 1979, Pis'ma Zh. Eksp. Teor. Fiz., 30, 719
Starobinsky, A. A. 1982, Phys. Lett. B, 117, 175
Starobinsky, A. A. 1985, Sov. Astron. Lett., 11, 133
Steigman, G. 2007, Annu. Rev. Nucl. Part. Sci., 57, 463
Steigman, G., Schramm, D. N., & Gunn, J. E. 1977, Phys. Lett. B, 66, 202
Steinhardt, P. J., & Accetta, F. S. 1990, Phys. Rev. Lett., 64, 2740
Stompor, R., & Efstathiou, G. 1999, MNRAS, 302, 735
Takada, M., Komatsu, E., & Futamase, T. 2006, Phys. Rev. D, 73, 083520

Tegmark, M. 2005, Phys. Scr., T121, 153
Tegmark, M., de Oliveira-Costa, A., & Hamilton, A. J. 2003, Phys. Rev. D, 68, 123523
Tegmark, M., et al. 2004a, ApJ, 606, 702
Tegmark, M., et al. 2004b, Phys. Rev. D, 69, 103501
Tegmark, M., et al. 2006, Phys. Rev. D, 74, 123507
Tocchini-Valentini, D., Douspis, M., & Silk, J. 2005, MNRAS, 359, 31
Tocchini-Valentini, D., Hoffman, Y., & Silk, J. 2006, MNRAS, 367, 1095
Tonry, J. L., et al. 2003, ApJ, 594, 1
Trotta, R. 2007, MNRAS Lett., 375, L26
Trotta, R., & Melchiorri, A. 2005, Phys. Rev. Lett., 95, 011305
Tsujikawa, S., & Gumjudpai, B. 2004, Phys. Rev. D, 69, 123523
Turner, M. S., & Wilczek, F. 1991, Phys. Rev. Lett., 66, 5
Upadhye, A. 2007, Nucl. Phys. Proc. Suppl., 173, 11
Verde, L., & Peiris, H. V. 2008, J. Cosmol. Astropart. Phys., JCAP07(2008)009
Verde, L., Wang, L., Heavens, A. F., & Kamionkowski, M. 2000, MNRAS, 313, 141
Viel, M., Haehnelt, M. G., & Lewis, A. 2006, MNRAS, 370, L51
Vielva, P., Martínez-González, E., Barreiro, R. B., Sanz, J. L., & Cayón, L. 2004, ApJ, 609, 22
Wandelt, B. D. 2003, ECONF, C030908, WELT001
Wandelt, B. D., Larson, D. L., & Lakshminarayanan, A. 2004, Phys. Rev. D, 70, 083511
Wang, L., & Kamionkowski, M. 2000, Phys. Rev. D, 61, 63504
Wang, L., & Steinhardt, P. J. 1998, ApJ, 508, 483
Wang, Y. 2008, Phys. Rev. D, 77, 123525
Wang, Y., & Mukherjee, P. 2007, Phys. Rev. D, 76, 103533
Wang, Y., & Tegmark, M. 2004, Phys. Rev. Lett., 92, 241302
Watanabe, Y., & Komatsu, E. 2006, Phys. Rev. D, 73, 123515
Weinberg, S. 1972, Gravitation and Cosmology (New York: Wiley)
Weinberg, S. 1978, Phys. Rev. Lett., 40, 223
Weinberg, S. 1989, Rev. Mod. Phys., 61, 1
Weinberg, S. 2003, Phys. Rev. D, 67, 123504
Weinberg, S. 2004, Phys. Rev. D, 70, 083522
Weinberg, S. 2008, Cosmology (Oxford: Oxford Univ. Press)
Wetterich, C. 1988, Nucl. Phys. B, 302, 668
Wiaux, Y., Vielva, P., Barreiro, R. B., Martínez-González, E., & Vandergheynst, P. 2008, MNRAS, 385, 939
Wilczek, F. 1978, Phys. Rev. Lett., 40, 279
Winitzki, S., & Kosowsky, A. 1998, New Astron., 3, 75
Wood-Vasey, W. M., et al. 2007, ApJ, 666, 694
Wright, E. L. 2007, ApJ, 664, 633
Wright, E. L., et al. 2009, ApJS, 180, 283
Wu, C. S., Ambler, E., Hayward, R. W., Hoppes, D. D., & Hudson, R. P. 1957, Phys. Rev., 105, 1413
Xia, J.-Q., Li, H., Wang, X., & Zhang, X. 2008, A&A, 483, 715
Yadav, A. P. S., Komatsu, E., Wandelt, B. D., Liguori, M., Hansen, F. K., & Matarrese, S. 2008, ApJ, 678, 578
Yadav, A. P. S., & Wandelt, B. D. 2008, Phys. Rev. Lett., 100, 181301
Yamamoto, K., Parkinson, D., Hamana, T., Nichol, R. C., & Suto, Y. 2007, Phys. Rev. D, 76, 023504
Yao, W. M., et al. 2006, J. Phys. G: Nucl. Part. Phys., 33, 1
Zaldarriaga, M. 1997, Phys. Rev. D, 55, 1822
Zaldarriaga, M., & Seljak, U. 1997, Phys. Rev. D, 55, 1830
Zaldarriaga, M., & Seljak, U. 1998, Phys. Rev. D, 58, 023003
Zhang, P., Liguori, M., Bean, R., & Dodelson, S. 2007, Phys. Rev. Lett., 99, 141302
Zhao, G.-B., Xia, J.-Q., Feng, B., & Zhang, X. 2007, Int. J. Mod. Phys.D, 16, 1229
Zlatev, I., Wang, L., & Steinhardt, P. J. 1999, Phys. Rev. Lett., 82, 896